공학박사학위논문

항복점 현상으로 인한 금속 박판 재료의 꺾임 결함과 소부 경화에 대한 실험 및 수치해석 연구

Experimental and numerical investigation for the fluting defect and bake hardening of metallic sheet materials originated from the yield-point phenomenon

2020 년 2 월

서울대학교 대학원

기계항공공학부

김 재 현

항복점 현상으로 인한 금속 박판 재료의 꺾임 결함과 소부 경화에 대한 실험 및 수치해석 연구

Experimental and numerical investigation for the fluting defect and bake hardening of metallic sheet materials originated from the yield-point phenomenon

지도교수 김 도 년

이 논문을 공학박사 학위논문으로 제출함

2019 년 10 월

서울대학교 대학원

기계항공공학부

김 재 현

김재현의 공학박사 학위논문을 인준함

2019 년 12 월

위 원 장 : 윤 병 동 (서명)

부위원장 : 김 도 년 (서명)

위 원 : 윤 군 진 (서명)

위 원 : 이 명 규 (서명)

위 원 : 김 태 효 (서명)

Abstract

Experimental and numerical investigation for the fluting defect and bake hardening of metallic sheet materials originated from the yield-point phenomenon

Jaehyun Kim
School of Mechanical and Aerospace Engineering
The Graduate School
Seoul National University

The yield-point phenomenon of annealed or aged metals has duality in terms of avoiding it or utilizing it. Defects such as fluting in v-bending originated from the phenomenon can be avoided through roller-leveling process composed of multiple up-and-down bending operations. However, excessive leveling conditions can lead to superficies defects, and an adequate process condition remains still elusive. Utilizing the phenomenon, bake hardening characterized by the significant increase of yield stress after baking of pre-strained low carbon steel can be used for improving dent resistance in automotive sheet metal forming applications. However, many previous investigations about bake hardenability concentrate only on the bake hardening response of uniaxial tension with related influence factors, and numerous numerical studies for the dent resistance rarely consider bake hardening effect. To accurately predict the behavior of materials with this phenomenon, the constitutive model for computational elastoviscoplastic analysis should be able to depict the yield-point phenomenon, the Bauschinger effect, and bake hardenability, rendering it difficult to obtain a converged solution in implicit numerical analysis when the conventional one-point Newton method is used. In the present study, firstly, comprehensive experimental investigations are performed for the fluting defect in the v-bending process, its reduction by the roller-leveling process, and the dent resistance of an automotive bake hardenable steel. Systematic evaluation for the effect of roller-leveling condition on the fluting in v-bending is then carried out

using pre-coated low carbon steel after examining the rate dependency and the cyclic characteristics of the phenomenon in uniaxial loads. The bake hardening behavior of a dual phase steel is observed in uniaxial load cases and static dent experiments conducted in pre-strained and bake hardened conditions. For numerical analysis to describe these experimental observation results, an implicit stress-integration procedure is formulated and implemented for a constitutive material model that can describe both the yield-point phenomenon and the Bauschinger effect. And we propose robust stress integration algorithms that can be used effectively in implicit finite element analysis employing the bisection method and the two-point Newton method. This material model is also integrated with a bake hardening model to illustrate bake hardening potentials. The validation results of the model with simple problems demonstrate that the model can be reliably used to calculate the solutions of the yield-point phenomenon problems that cannot be obtained using conventional iterative methods although these algorithms may require longer computational times. Numerical simulations corresponding to the experiments are carried out with material parameters determined to reproduce the uniaxial experiments. V-bending simulations at various roller-leveling conditions fairly demonstrate the fluting defect and its reduction experimentally observed. The bake hardening behaviors identified in the experiments are investigated in static dent simulations including a bake hardening step, and the bake hardening effect is overall described in numerical simulations. To conclude, the proposed analysis procedure is expected to be useful in estimating a proper leveling condition to prevent potential defects and dent resistance of automotive bake hardenable steels as well as investigating the effect of the yield-point phenomenon in various metal forming processes.

keywords: Yield-point phenomenon, Elastoviscoplasticity, Stress integration algorithm, Fluting, Bake hardening, Dent

student number: 2016-36339

Contents

List of Tables

List of Figures

Chapter 1

Introduction

1.1 Yield-point phenomenon

The yield-point phenomenon (YPP) is a unique yielding behavior observed often in aged or annealed low carbon steel. In a uniaxial tension test, the YPP can be characterized by three aspects: sharply increased yielding stress, consecutive stress drop and lower yielding fluctuation as observed in Fig.1.1. As described in the schematic tensile specimens in Fig.1.1, the sharply increased yielding stress is the elastic limit which can be called upper yield point, and the lower yielding fluctuation after the subsequent stress drop results from the local plastic deformation consisting of Lüders bands nucleation and propagation. The YPP was firstly reported in the experiment of Piobert et al. (1842) where the surficial marks on a metal plate deformed by a projectile were observed. The definite description of these marks was made by Lüders (1860) with the polished surface of bent metal, leading to the birth of terminology, Lüders band. Since these experimental works, many studies investigating the YPP have been reported including the well-known dislocation locking theory proposed by Cottrell and Bilby (1949) and the dislocation proliferation and velocity characteristics acquired by Johnston and Gilman (1959). The dislocation locking theory brought the terminology, *Cottrell atmosphere* which can help to explain the unique characteristics of the YPP such as an upper yield point and

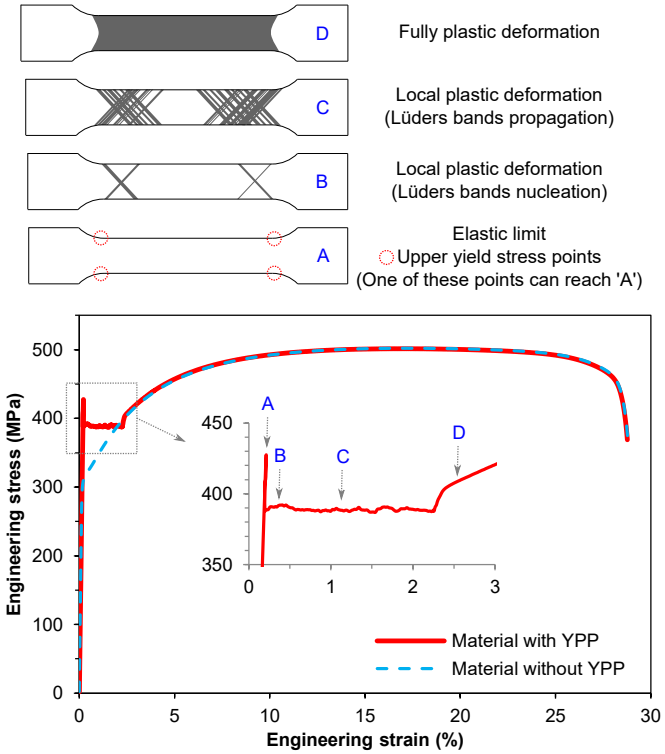

Figure 1.1. Stress-strain responses of metallic material with YPP and without YPP in their uniaxial tensile test and corresponding schematic tensile specimens

a subsequent yield drop by relating them with the diffusion of interstitial carbon or nitrogen atoms into a dislocation core. Although this theory was well established in terms of the dislocation locking, it was not fully satisfied with the unlocking concept because Johnston and Gilman (1959) found a case where the YPP was not affected by the unpinning of dislocations in LiF crystals. Including these locking and unlocking debates, deeper and broader insights into the YPP in the 1950s and 1960s are well summarized in Hall (1970). In the last couple of decades, the research focus of the YPP has been transfigured from explicating the YPP itself to explaining and describing it with the finite element (FE) method.

1.2 Avoiding or utilizing the YPP

The YPP can cause forming defects such as *stretcher strains* and *fluting* in sheet metal forming applications where the fluting is also referred to as *kinking* as stated in Ding and Duncan (2004) and Duncan et al. (1999). Being distinct from typical defects such as crack, necking, wrinkle, and springback in sheet metal forming process, these defects result from inhomogeneous plastic deformation due to the YPP and can be regarded as critical defects when they appear in outer panels of automotive vehicles or home appliances.

In general, the YPP can be alleviated by temper rolling, also known as skin pass rolling, that provides diminutive strains, usually less than 0.5%, to the material as stated in Hosford and Caddell (2011). However, pre-coated low carbon steel (PLCS) often exhibits the YPP even after the temper rolling process at the last stage of steel production because the material can be aged during the post-production color coating process of hot temperature. Similar to other aged low carbon steels, the YPP of PLCS is characterized, in its stress-strain curve of uniaxial tension, by the sharp upper yield point, the subsequent yield drop to the lower yield point and the lower yield region (Fig.1.2a). Localized plastic deformation due to the YPP engenders Lüders bands

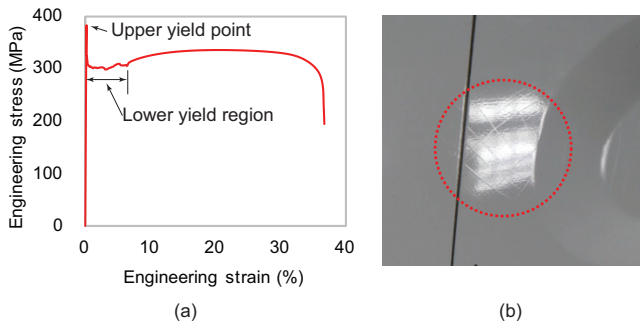

Figure 1.2. The YPP of PLCS: (a) stress-strain response in uniaxial tension test and (b) stretcher strains in circular embossing.

or stretcher strains, for example, in circular embossing (Fig.1.2b). The YPP-induced

plastic deformations can also lead to the fluting defect in the v-bending (Fig.1.3a) of PLCS in its as-received (without any process for YPP reduction) condition. Here, an

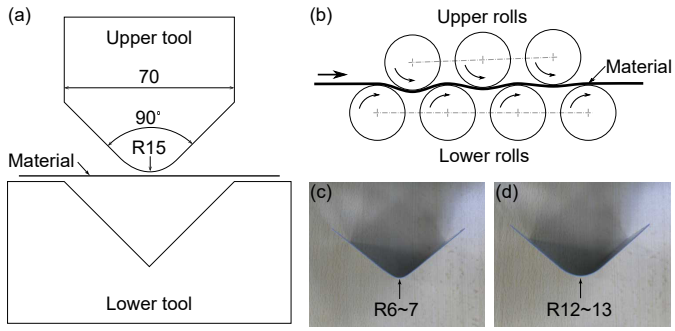

Figure 1.3. Fluting defect in the v-bending process: (a) schematic diagram of the v-bending process with an R15 punch; (b) schematic diagram of the roller-leveling process; (c) a sharp corner shape observed in the raw PLCS after the v-bending due to fluting defects; and (d) a normal corner shape observed in the roller-leveled PLCS after the v-bending.

undesirably sharp corner is observed as plastic deformations localized at the corner form a plastic hinge in the bending process (Fig.1.3c). Nevertheless, it has been shown that the YPP can be reduced, if not fully removed, with the application of the roller-leveling process consisting of cyclic bending operations (Fig.1.3b). Pearce (1991) explained that these operations induce mobile dislocations sufficient to diminish the yield-point elongation. Plastic deformations generated from repeated bending-unbending actions during this process abate the YPP. While Theis (1999) showed that this process has been frequently used to correct other shape defects including crossbow, edge wave, center buckle, camber, and twist, it is essential to avert defects associated with the YPP such as fluting particularly for materials like PLCS (Fig.1.3d).

Although it is important to eschew the YPP by a roller-leveling process in the aforementioned cases, the YPP is not always something that should be avoided because there is a suitable method to utilize it in sheet metal forming applications. That is bake hardening (BH) behavior characterized by a drastic yield stress increase after the

paint baking of pre-strained low carbon steel. In general, this BH behavior is known to be contributed by two effects, the Cottrell atmosphere and precipitation hardening. Among these two sources of hardening, the dislocation locking develops first until all of dislocation sites are occupied with solute atoms. When this locking atmosphere is fully condensed and if free solute atoms are still available, the precipitation hardening successively begins by forming the precipitates of ε-carbide. This two-stage concept was reported in the past literature such as Wilson and Russell (1960) and well explained in Elsen and Hougardy (1993). More detailed metallurgical knowledge for the BH mechanisms can be referred to Rana and Singh (2017).

Various automotive body parts such as outer skin panels and structural members take advantage of the BH behavior in order to improve dent and crash resistance. This improvement also can contribute to the vehicle body lightweighting by reducing the thickness of the steel sheet used. As stated in Kantereit (2011), representative automotive steels that reveal the BH behavior are conventional BH steels developed in the 1980s. Some of advanced steel grades such as dual phase (DP) and transformation-induced plasticity (TRIP) steels also have the BH potential which is investigated by many studies like Waterschoot et al. (2003), Timokhina et al. (2007), J. Zhang et al. (2008), and Ramazani et al. (2014).

As a key mechanical property of bake hardenable automotive steels, BH stress can be determined in uniaxial tension test before and after baking operation as illustrated in Fig.1.4. The BH stress value is the difference between the highest stress in the pre-tension and the lower yield stress of the tension after baking. The pre-tension and baking step epitomizes the forming and the paint baking process, respectively, in the actual automotive sheet metal applications. The dent resistance test such as SAE J2575 is often used in evaluating the BH potential of automotive steels. In Holmberg and Thilderkvist (2002), it was observed that higher yield stress can directly improve the dent performance. If this higher stress is obtained by BH in paint baking, bake-hardened steels can induce superior dent characteristics to non-bake-hardenable steels even with

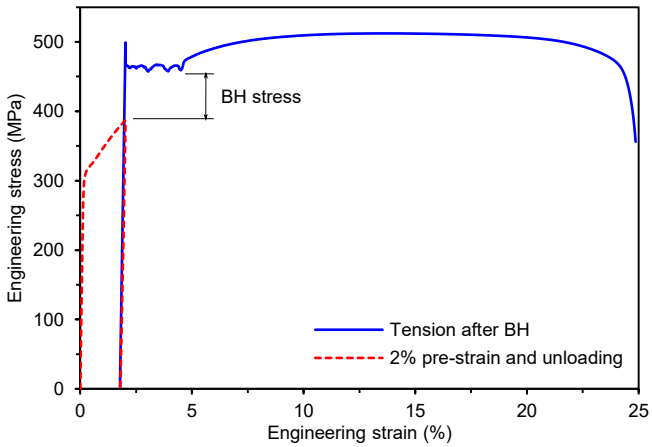

Figure 1.4. Stress-strain response of DP steel in uniaxial tension test before and after baking operation.

similar yield stress after forming and similar thickness.

1.3 Literature review

1.3.1 YPP defect and its reduction method

There have been few studies on the YPP-related defect and its reduction method. Aratani et al. (1997) found that fluting occurred at the yield-point elongation over 4.5% in the production process of roll-formed three-piece can body with the steel of 0.18 mm thickness and 0.041% carbon content. They also demonstrated the reduction of fluting by the flexor treatment that gave bending and unbending deformation prior to the roll forming process. This treatment is similar to the roller-leveling process except it uses only one set of rolls. Park and Yoon (2007) did theoretical, experimental and numerical investigation on the onset condition of fluting in the tangential bending process with low carbon steel of 0.5-0.6 mm thickness. Park (2015) conducted an experimental study on adequate roller-leveling conditions to reduce the YPP-related defects, mostly the stretcher strains in the circular embossing of PLCS. It was found that unwanted surficial

defects could be generated if an excessive leveling condition was applied. Nevertheless, the effect of YPP in other manufacturing processes such as the v-bending process has been rarely reported and the proper condition of a roller-leveling process to eliminate the YPP-related defects remains elusive.

1.3.2 Dent resistance considering BH behavior

Studies on dent resistance of automotive panels have been reported many times, but those considering BH behavior are rarely found in the past literature. Asnafi (1995) derived analytic equations to evaluate the dent resistance and experimentally validated the equations. Holmberg and Thilderkvist (2002) investigated the material dependency of the static dent resistance varying the conditions of forming operation. Jung (2002) conducted FE analysis as well as analytic calculations to identify the relationship between the dent-related performance of automotive body panels and their design factors such as material properties, thickness, panel size, curvature, and test condition. However, these works did not include BH materials or contemplate BH behavior even when BH materials were involved in their studies. Holmberg and Nejabat (2004) showed the limitation of isotropic hardening model in the numerical simulation of dent resistance, and Shen et al. (2010) demonstrated the accuracy improvement in the numerical analysis of dent resistance by using a linear kinematic hardening model and a nonlinear combined hardening model. Recently, an advanced constitutive model was adopted in Lee et al. (2016) for dent resistance FE analysis providing more accurate predictions than a conventional approach that uses von Mises yield function, isotropic hardening, and a constant elastic modulus. Nonetheless, BH behaviors or BH materials were not handled by these studies.

1.3.3 Constitutive model and numerical analysis for YPP

There have been various studies on the constitutive model and numerical analysis for YPP. The theory proposed by Cottrell and Bilby (1949) was a starting point of

YPP constitutive models. They suggested a dislocation locking theory to elucidate the mechanism of the YPP beyond the ostensible observations of Piobert et al. (1842) and Lüders (1860). However, this well-established theory was not fully aligned with the unlocking concept because Johnston and Gilman (1959) found no evidence of dislocation unpinning in LiF crystals exhibiting the YPP. Based on their investigation, Hahn (1962) built a constitutive model describing the YPP on the premise of the expeditious dislocation proliferation and the stress effect on the dislocation velocity. Yoshida (2000) pioneered an elastoviscoplastic constitutive model depicting both the YPP and cyclic behaviors that had never been suggested before this model. Its YPP part was developed based on the dislocation multiplication and velocity behavior where a phenomenological approximation for the fraction of mobile dislocation density was newly proposed to express the rapid dislocation multiplication. Later, Yoshida et al. (2008) improved this model in order to capture a sharper upper yield point and carried out explicit FE simulations to find out the appropriate rolling condition to remove the YPP in the temper rolling process (hereafter, this improved model is referred to as Yoshida-2008 model). They adopted a two-surface kinematic hardening rule proposed by R. D. Krieg (1975) in order to illustrate the Bauschinger effect by using multiple equations solved for the relative motion of the yield surface to the bounding surface.

A lot of research effort to advance the YPP model and its application to the prediction YPP-related defects has been followed after Yoshida's pioneering work. Park and Hwang (2002) performed FE analysis to investigate the optimum roller-leveling condition to remove blanking bow defects using a rather simple, linear hardening model without considering the YPP. Park and Yoon (2007) identified the fluting condition in terms of material properties in tangential bending by using the FE analysis procedure of Park and Hwang (2002) with an improved material model consisting of lower yield and linear hardening regions neglecting the upper yield point followed by a sudden yield drop. Pepelnjak and Barisic (2007) optimized the part geometry to remove the stretcher strains on tinplate rings based on FE simulation results. Wenman and Chard-

Tuckey (2010) predicted the residual stress characterizing the Lüders strain in a compact tension specimen under a complex loading condition by employing the plasticity model proposed by S. Zhang et al. (2001) without considering the kinematic hardening behavior. Žerovnik et al. (2010) developed a rate-independent phenomenological material model that captures both cyclic plasticity and YPP. Schwab and Ruff (2013) explained the actual material behavior associated with the YPP by using a simple macromechanical model without taking the rate dependency of YPP and the Bauschinger effect into account. Mazière and Forest (2015) obtained the Lüders strain propagation analytically using a strain gradient plasticity model, which did not suffer from the mesh dependence problem observed in conventional FE analysis. Nevertheless, this model was also based on the rate-independent plasticity and did not consider the cyclic behavior. Giarola et al. (2015) performed FE analysis for the skin pass rolling process using the material model displaying the actual upper yield point suggested by Yoshida et al. (2008) and Schwab and Ruff (2013) with the rigid-plastic, rate-independent, and isotropic hardening behavior.

1.3.4 Stress integration algorithms

These YPP models were often implemented explicitly for FE analysis partly because of their high nonlinearities making it hard to obtain a converged solution iteratively using an implicit stress integration algorithm. As described in Prior (1994), since an implicit algorithm may fail to find a converged solution or it may require a significantly large number of iterations to get a solution, the explicit algorithm can be more effective even though a much smaller time step size need to be used in general. Pepelnjak and Barisic (2007) used an explicit code to avoid contact instabilities in an implicit method for simulating and analyzing stretcher strains in the stamping process at the increased forming speed of 4.6 m/sec. However, if the convergence can be guaranteed, using an implicit method can be more efficient in general as one can use a larger incremental step during analysis.

Since Wilkins (1964) firstly presented the famous stress integration algorithm, radial return mapping, many related topics such as iso-error map in R. D. Krieg and D. B. Krieg (1977), consistent tangent operator in Simo and Taylor (1985) and integration stability in Ortiz and Popov (1985) have been studied. Lately, exponential map based methods were introduced to enhance the accuracy of stress integration. Rezaiee-Pajand et al. (2010) applied an exponential-based method on the von Mises plasticity model with nonlinear kinematic hardening rules to show highly accurate stress integration. They also conducted similar studies on the nonlinear mixed hardening models in Rezaiee-Pajand et al. (2011a). Some semi-implicit schemes based on the exponential map methods in Rezaiee-Pajand et al. (2014) were converted from fully explicit schemes in Rezaiee-Pajand et al. (2011b). Despite their robustness and improved accuracy in stress integration, they might not be useful in handling non-convergent cases.

1.3.5 Recent YPP studies

Recently, Žerovnik et al. (2016) investigated the influence of the YPP on the cyclic plasticity by utilizing strain field images. Their experimental observation was, however, not connected to any numerical prediction. Markiewicz et al. (2016) identified the characteristics of viscoplastic behavior for spot-weld heat affected materials showing the YPP. They used the modified Krupkowsky viscoplastic model to compare numerical results with experimental data. Nevertheless, in their numerical work, the YPP and the cyclic behavior were not considered. Abspoel et al. (2017) proposed a new correlation method for yield criteria to obtain the stress factors directly from tensile test data. They neglected the YPP exhibited in the tensile test of low carbon steels when calculating the plastic work. C. Zhang et al. (2017) carried out microstructure-based FE analysis to study the effect of microstructure heterogeneity on the microscopic stress triaxiality in C-Mn weld metals. Their numerical simulation using the representative volume element (RVE) did not properly describe the yield point elongation of tensile experiments. Mao and Liao (2019) also used RVE to predict the YPP and work hardening behaviors of

DP steels. Although their model was able to reveal the upper and lower yield points as well as the yield-point elongation, they did not investigate the cyclic behaviors.

1.3.6 BH models

In order to scope out BH models that can be used to describe the BH behavior, the dislocation locking mechanism proposed by Cottrell and Bilby (1949) should be revisited. Their proposed theory involves the diffusivity and concentration of solute atoms with BH time and temperature and could predict the extent of dislocation locking. However, their theory was meaningful only for the early stage of pinning process and modified by Harper (1951) and Cochardt et al. (1955) to consider the saturation of the pinning process. Hartley (1966) presented a simplified equation to calculate the BH stress by employing the concepts of thermally activated dislocation mechanisms discussed in Conrad (1964). The two BH models, one from Harper (1951) and the other from Hartley (1966) were used to compare the aging kinetics between bake hardenable ultra low carbon steel and bake hardenable low carbon steel in De et al. (2001). While some of these early studies might not take the precipitation hardening into account in their BH models, Das et al. (2014) developed a new BH model that includes both the Cottrell effect and the precipitation hardening. The Cottrell effect part of this model was based on the equation of Hartley (1966) and the precipitation hardening part was originated from the Gladman (1999) and Zener (1949). Many previously published experimental BH data were in good agreement with the calculated result from the model of Das et al. (2014).

Although many kinds of literature researching BH models were published in the past, most of them focused on some factors affecting BH response or the response magnitude itself and investigations associated with sheet metal forming applications were rarely reported except for only a few studies such as Ballarin et al. (2009b) and Ballarin et al. (2009a). Ballarin et al. (2009b) developed a BH model which is based on the equation proposed by Zhao et al. (2001) for the formation of the Cottrell atmosphere

and an evolution equation describes the growth of precipitates for the precipitation hardening. They coupled the developed model with their simple bilinear YPP model originated from Tsukahara and Iung (1998) and carried out uniaxial tension tests and simulations to validate their coupled model. Ballarin et al. (2009a) expanded their original work into complex loading paths by adapting a polycrystalline self-consistent approach. However, these works did neither consider the kinematic hardening and the rate-dependency in their YPP model nor assess BH potentials in actual applications such as static dent cases.

1.4 Objectives and outline

Although many aforementioned investigations on the YPP and related applications including BH behavior have been reported, no comprehensive studies on the emergence of YPP-related defects, the process condition for their prevention, and the evaluation of the BH potential with the static dent performance have been conducted to the best of authors' knowledge. In this thesis, the first objective is to experimentally investigate the YPP with PLCS and BH behavior with DP steel in various cases such as uniaxial load, v-bending together with roller-leveling for YPP defects, and static dent load for BH. Secondly, in order to describe these experimental behaviors, it is aimed to enable implicit elastoviscoplastic FE analysis for materials with the YPP by employing a robust stress integration algorithm. To illustrate, we consider the Yoshida-2008 model, arguably the most comprehensive model depicting both the YPP and the Bauschinger effect, whose kinematic hardening part is replaced with the one proposed by Yoshida and Uemori (2003) for simplicity. To integrate the BH model into the YPP model is also included in this objective. The last objective is to numerically simulate the YPP and BH behavior such as fluting defect in v-bending, its reduction by the roller-leveling process, and the BH effect in the static dent case using the YPP and BH integrated model.

In the beginning, in Chapter 2, the YPP-related behaviors of PLCS are characterized

by performing uniaxial tension tests at various crosshead speeds, uniaxial cyclic tests, and v-bending tests under systematically varied roller-leveling conditions as described. The investigation on the BH behavior of DP steel is carried out with uniaxial tension and compression experiments before and after BH operation at several BH conditions. At the same conditions, static dent experiments before and after BH operation are also conducted. New findings from these experiments are addressed in detail.

In Chapter 3, a robust implicit stress-integration procedure is formulated for a constitutive material model that can capture the rate-dependent YPP and the Bauschinger effect. This procedure is implemented as a user-material subroutine UMAT of Abaqus/-Standard for FE analysis. Here, the Yoshida-2008 model is employed as a base model with some modifications to use a more efficient kinematic hardening rule in the implicit approach proposed by Yoshida and Uemori (2003) and to consider the true yield-point behavior explained in Schwab and Ruff (2013). And the two-point Newton method is also employed, which is shown to be robust and efficient in solving non-convergent nonlinear equations with a single variable in Tiruneh et al. (2013) or multiple variables in Saheya et al. (2016), unlike the typical one-point Newton method. The material model is used to test several stress integration algorithms including the conventional one-point Newton method, the two-point Newton method, the bisection method, and their combinations. The BH model proposed in Das et al. (2014) is taken and coupled with the material model to take BH behavior into account.

In Chapter 4, numerical simulations for validating the robustness of the material model are carried out for uniaxial tension, simple shear, uniaxial cyclic, v-bending and cantilever bending problems. The performance of each stress integration algorithm is evaluated by the computing time, the number of increments and the simulation response. BH calculations are also verified using single element simulations.

In Chapter 5, FE simulations corresponding to v-bending and roller-leveling experiments of PLCS are carried out for mimicking the fluting defect and its reduction. These simulations use the constitutive model whose material parameters are determined to

match the experimental data in uniaxial tension and cyclic tests of PLCS. The prediction capability of the model for the pertinent condition of the roller-leveling is demonstrated by the results of roller-leveling FE analysis followed by v-bending simulations. Numerical simulations corresponding to the static dent experiments of DP steel are conducted using the YPP and BH coupled model with the material parameters chosen to fit the experimental result of uniaxial tension and compression tests of the same material. The BH steps are also included in these simulations. The simulation results overall illustrate the BH behavior of the DP steel providing the assessment of BH performance of the material.

It is expected that the established FE analysis procedure with the proposed material model would be useful in investigating the effect of YPP in other metal forming processes and estimating a proper condition for the roller-leveling process to effectively remove YPP-related defects. Also, the proposed model can be utilized in evaluating the BH potential with the static dent analysis. Note that the contents from Chapter 2 to Chapter 5 are addressed based on our previous research of J. Kim and D. N. Kim (2019) and J. Kim et al. (2019) except for the consideration of BH behavior.

Chapter 2

Experimental Investigations

In this chapter, comprehensive sets of experiments are devised and performed to systematically analyze the YPP-related behaviors of PLCS and the static dent resistance of bake hardenable DP steel. For the behaviors of PLCS, specifically, we explore the rate dependency of the YPP in uniaxial tension tests, the cyclic characteristics in uniaxial cyclic tests, and the effect of roller-leveling conditions on the fluting as well as the rate dependency of the fluting in v-bending tests. The PLCS of these experiments is the thickness of 0.6 mm and the carbon content of 0.02%.

For the dent resistance of bake hardenable DP steel, uniaxial tension, uniaxial tension-compression, and static dent tests are carried out with BH operation. The bake hardenable galva-annealed DP steel with the carbon content of 0.078%, the thickness of 0.7 mm, and the tensile stress of 490 MPa is used for these experiments. Hereinafter, this material is referred to as 490DP. For the BH operation of all related experiments, a climatic chamber Climats Excal 2211-TA PS is used to have a high precision temperature profile.

2.1 Experimental observations for fluting defect and its reduction method with PLCS

2.1.1 Uniaxial tension test

The dimensions of PLCS uniaxial tension specimen with the gauge length of 50 mm are specified in Fig.2.1. The specimens are prepared so that their rolling direction (RD)

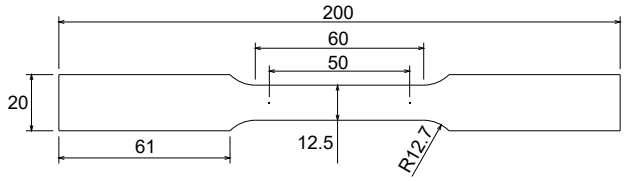

Figure 2.1. Specimen for the uniaxial tension test. The thickness of the specimen is 0.6 mm.

is aligned to the tensile direction. Uniaxial tension tests are performed at the crosshead speeds of 0.6, 6, and 30 mm/min using a Zwick-Roell 100 kN universal testing machine equipped with a contact-type extensometer. The tests are repeated three times for each crosshead speed condition.

The stress-strain curves and their YPP-related properties are shown in Fig.2.2a and Fig.2.2b, respectively. These properties are quantified referring to ISO 6892-1:2016. The upper yield point is determined from the first peak value of the stress-strain curve while the lowest value in the lower yield region is measured as the lower yield point. The yield-point elongation is calculated by subtracting the strain value at the upper yield point from that at the beginning of uniform strain hardening. The latter value is selected at the point of highest slope around the beginning of uniform strain hardening as indicated using hollow symbols in Fig.2.2a. The highest slope point is determined by selecting the maximum value among instantaneous slope values calculated by $(\sigma_{(k)} - \sigma_{(k-1)})/(\varepsilon_{(k)} - \varepsilon_{(k-1)})$ around the beginning of uniform strain hardening. It can be observed that the upper and lower yield points increase with the crosshead speed,

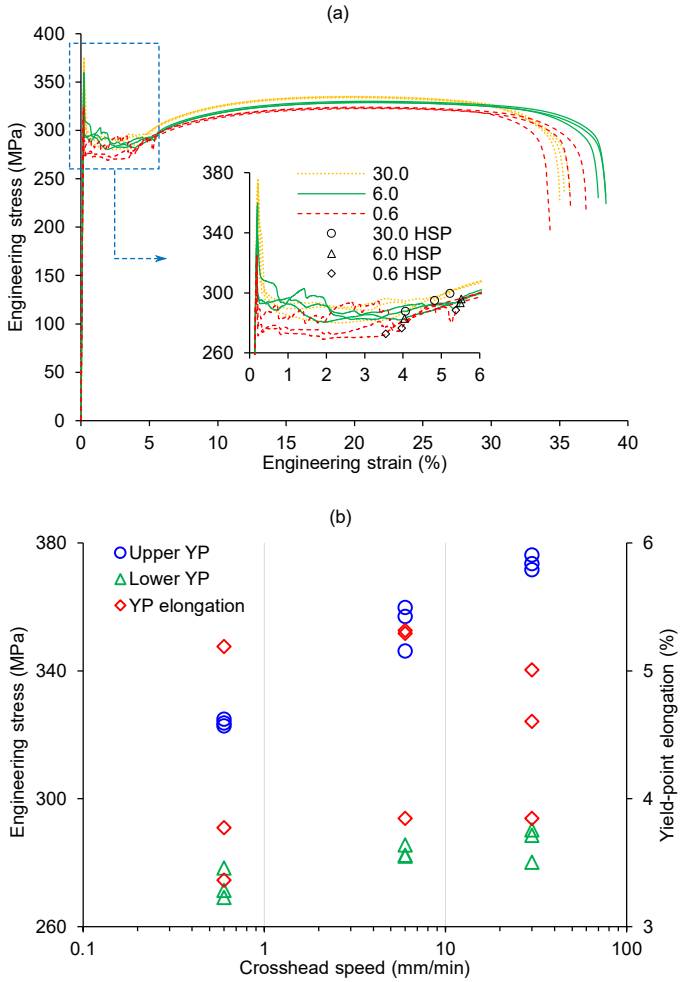

Figure 2.2. Results of the uniaxial tension tests: (a) stress-strain responses at the crosshead speed of 0.6, 6 and 30 mm/min and (b) corresponding YPP-related properties. HSP indicates the highest slope points and YP denotes the yield-point.

which agrees qualitatively with the experiments by Yoshida (2000) for the hot-rolled low carbon steel with 0.07% carbon content and the experiments by Watanabe (1982) for the cold-rolled low carbon steel with 0.07% carbon content. Sun et al. (2003) also experimentally showed the rate dependency of the yield-point elongation and the lower yield point for low carbon steel. On the other hand, the yield-point elongation data in the present experiments are rather scattered with a relatively large variation. The scattered

yield-point elongations might be because the yield-point elongation is dominated by the nucleation and propagation of the Lüders band. This behavior of the Lüders band is hardly homogeneous as well as it is difficult, in practice, to pinpoint the beginning of uniform strain hardening from the noisy stress-strain curves. As a result, unlike the previous experiments by Yoshida (2000), Watanabe (1982) and Sun et al. (2003), no clear tendency with respect to the crosshead speed was observed. Meanwhile, as reported in Yoshida (2000), the stress level in the strain hardening region is elevated with respect to the crosshead speed.

2.1.2 Uniaxial cyclic test

Uniaxial cyclic tests consisting of tension, compression, and re-tension processes with PLCS are carried out for the strain ranges of 4% and 8% at the crosshead speed of 10 mm/min using a servo-controlled testing machine equipped with a laser extensometer. Specimens whose gauge length is 20 mm are used with other dimensions as specified in Fig.2.3. Again, the uniaxial force is applied along their RD. The gauge width of the

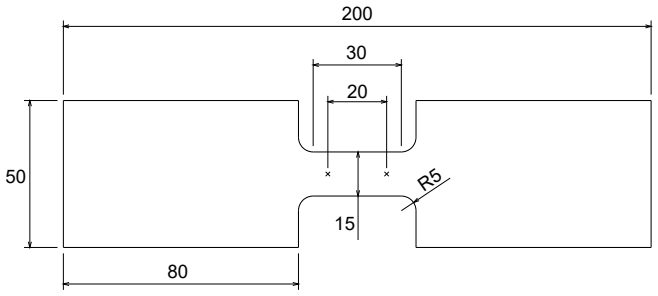

Figure 2.3. Specimen for the uniaxial cyclic test. The thickness of the specimen is 0.6 mm.

specimen and the clamping force applied are 15 mm and 200 kgf, respectively. These values are chosen to avoid any instability during the test based on two equations in Bae and Huh (2011) originally derived in Boger et al. (2005) and Cao and Wang (2000). According to those equations, the maximum attainable compressive strain is about

0.146 and the corresponding clamping force is about 300 kgf. In the present experiment, however, the clamping force is selected as 200 kgf to reduce the frictional and biaxial effects on the specimen. In this condition, the compressive strain is 0.094 larger than the current strain ranges. In addition, Teflon sheets whose thickness is 0.1 mm are attached to both sides of the gauge section in order to minimize the frictional force caused by the clamping force. In general, raw stress-strain data need to be corrected for frictional and biaxial influences due to the clamping force. The frictional corrections for the acquired stress-strain data are made using the method in Boger et al. (2005). We adjust the friction coefficient used for correction in the range of 0.06-0.11 to match the uniaxial tension curve at the same crosshead speed. The biaxial effect is ignored because the normal stress induced by the clamping force is much smaller than the longitudinal stress. Normal stress σ_n in the gauge length area (30 mm x 15 mm) is about 4.4 MPa. Then, the effective stress considering the biaxial effect can be calculated as

$$\sqrt{\frac{1}{2}\left[(\sigma_m - \sigma_n)^2 + {\sigma_m}^2 + {\sigma_n}^2\right]} \tag{2.1}$$

with the measured longitudinal stress σ_m. The difference between this effective stress and the absolute value of σ_m is about 2 MPa which can be neglected.

The corrected stress-strain responses are plotted in Fig.2.4. Note that the curves in Fig.2.4b are symmetric about the stress reversal points. The Bauschinger effect is clearly captured after the stress reversals for both 4% and 8% strain ranges. The change in the strain hardening rate is hardly observed in the second tension of the 4% strain range test. It might be because the disintegration of the dislocation cell walls generated during the compression is not completed in the second tension as observed in Hasegawa et al. (1975) with transmission electron microscopy. No permanent softening in the compression of the 4% test is identified from the curve. This might be linked to the fact that the compression region is within the region of yield-point elongation and the dislocation cell walls are not fully developed during the first tension. On the other hand, the workhardening stagnation and the subsequent strain hardening appear clearly in the 8% strain range test. This means that the preformed dislocation cell walls are

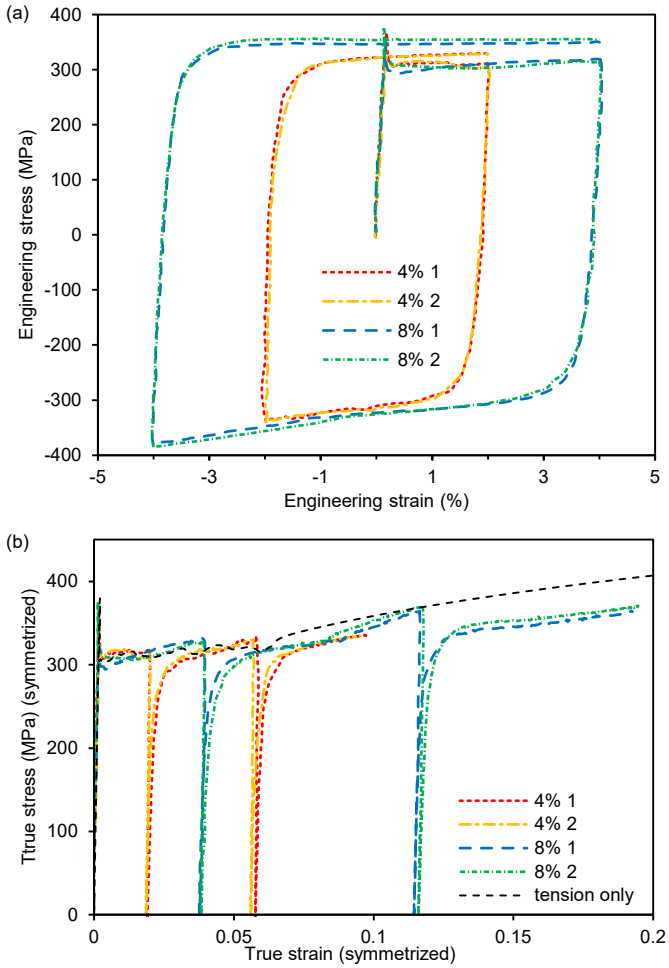

Figure 2.4. Stress-strain responses of the uniaxial cyclic tests in the strain range of 4% and 8% at the crosshead speed 10 mm/min: (a) engineering stress vs. engineering strain and (b) true stress vs. true strain symmetrized about the stress reversal points.

completely dissolved at the deflection points in the reversed deformations. The strain hardening slope after the deflection point in the compression is steeper than that in the second tension. These workhardening stagnation behaviors are in accord with the experimental studies by Hu et al. (1992).

2.1.3 Roller-leveling test

The primary control parameter in the roller-leveling process is an intermesh (IM) that determines the vertical position of rolls. The roller-leveling tests are conducted with five intermesh conditions using an experimental roller-leveler illustrated in Fig.2.5 with the material feeding direction set to the RD. Test specimens are 750-800 mm long and

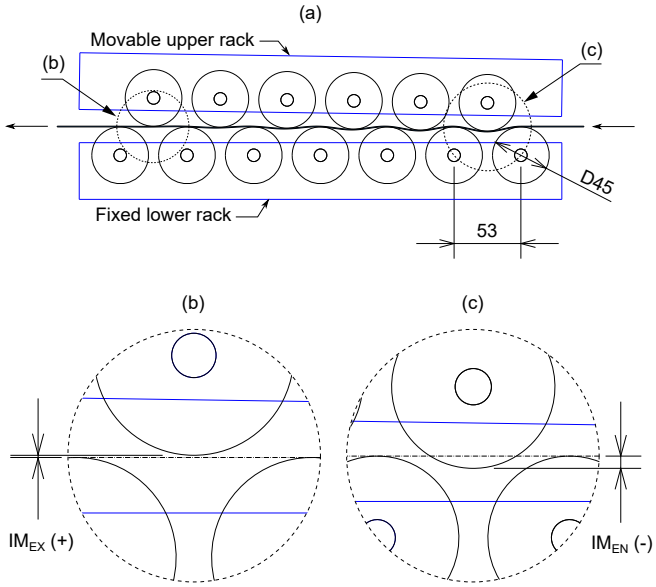

Figure 2.5. Configuration of the roller-leveling process: (a) a layout of upper and lower rolls; (b) a detail view of the exit intermesh; and (c) a detail view of the entrance intermesh.

100 mm wide. Generally, for materials with thin gauge, the entrance intermesh IM_{EN} is set to a negative value and the exit intermesh IM_{EX} is set to a positive value as indicated in Fig.2.5b and c. The amount of plastic strain induced to the material is determined by the entrance intermesh. Park et al. (2006) derived an equation to account for this relationship based on a simplified stress profile through the thickness assuming a pure bending situation. And Park (2015) rearranged the equation as

$$\mathrm{PF} = \frac{t - t_e}{t} = 1 - \frac{Y_0 L^2}{12Et(t - \mathrm{IM_{EN}})} \tag{2.2}$$

where PF is the plastic fraction representing the amount of induced plastic strain through the thickness, t and t_e denote the thickness and its elastic portion, respectively, Y_0 is the yield stress, L is the distance between two rolls and E is Young's modulus. The five intermesh conditions and corresponding PF calculated with $t = 0.6$ mm, $Y_0 = 305$ MPa, $L = 53$ mm and $E = 199.514$ GPa are listed in Table 2.1. The IM_{EX} and the

Table 2.1. Intermesh conditions and corresponding PF values in the roller-leveling process.

IM_{EN} (mm)	-0.8910	-1.3880	-1.7856	-2.3821	-3.3761
PF (%)	60	70	75	80	85

rotational speed of rolls are fixed to 0.5 mm and 20 rpm, respectively.

Simple visual inspection of PLCS plates after the roller-leveling process reveals the appearance of surface defects in the specimen processed with 85% PF condition as shown in Fig.2.6. These defects are presumably induced by the occurrence of repeated flutings during the roller-leveling process. They are hardly found in the specimens processed with other PF conditions. This observation agrees with the experimental result by Park (2015). To investigate more quantitatively, the 10 mm x 10 mm surfaces of each specimen are measured using the Wyko NT9300 Optical Profiler. The 3-D surface profiles and corresponding roughness values are shown in Fig.2.7. The average roughness Ra and the root mean square roughness Rq defined in Turner and Miller (2006) are expressed as

$$\text{Ra} = \frac{1}{n_p}\sum_{i=1}^{n_p}|\mathbb{Z}_i - \bar{\mathbb{Z}}| \quad \text{and} \quad \text{Rq} = \sqrt{\frac{1}{n_p}\sum_{i=1}^{n_p}(\mathbb{Z}_i - \bar{\mathbb{Z}})^2}, \tag{2.3}$$

respectively. Here, n_p, $\mathbb{Z}_i$, and $\bar{\mathbb{Z}}$ denote the number of measurement points, the surface height at measurement point i, and the mean value of $\mathbb{Z}_i$, respectively. Similar to the visual inspection in Fig.2.6, the surficial defects shown as the repeated fluting lines perpendicular to the RD can be observed in the surface profile of specimens processed with 80% and 85% PF conditions (Fig.2.7a). The measured roughness values

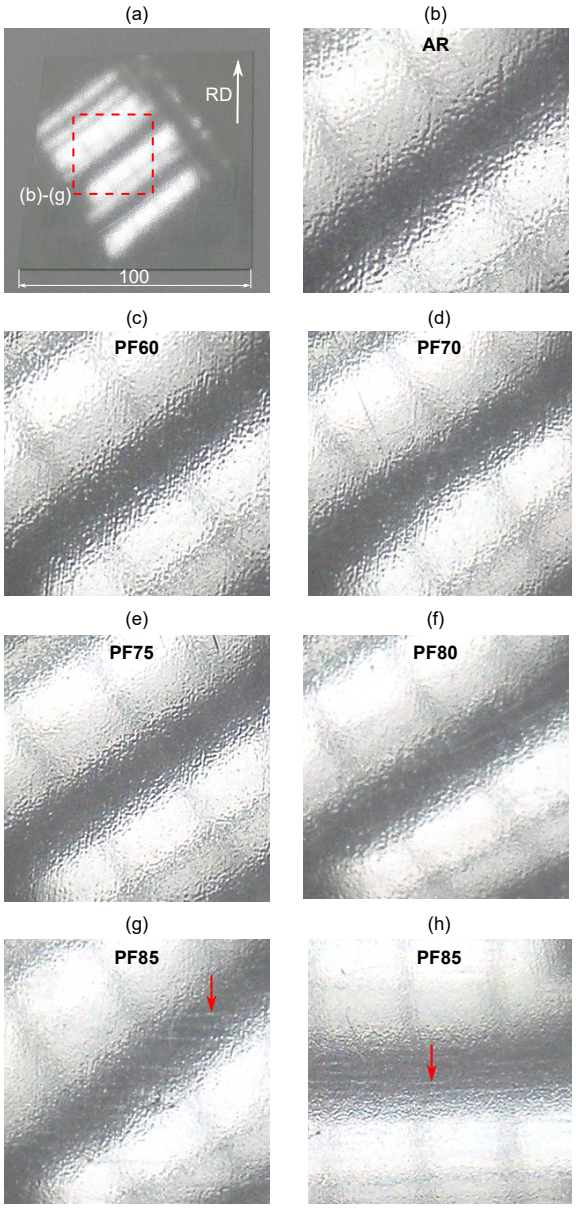

Figure 2.6. Surfaces of the roller-leveled specimens: (a) a part of specimen samples for the visual inspection under light; (b) as-received specimen; and (c)-(h) roller-leveled specimens processed with various PF conditions. (g) and (h) show the surface of the same specimen at different light angles. Red arrows indicate surface defects due to excessive roller-leveling.

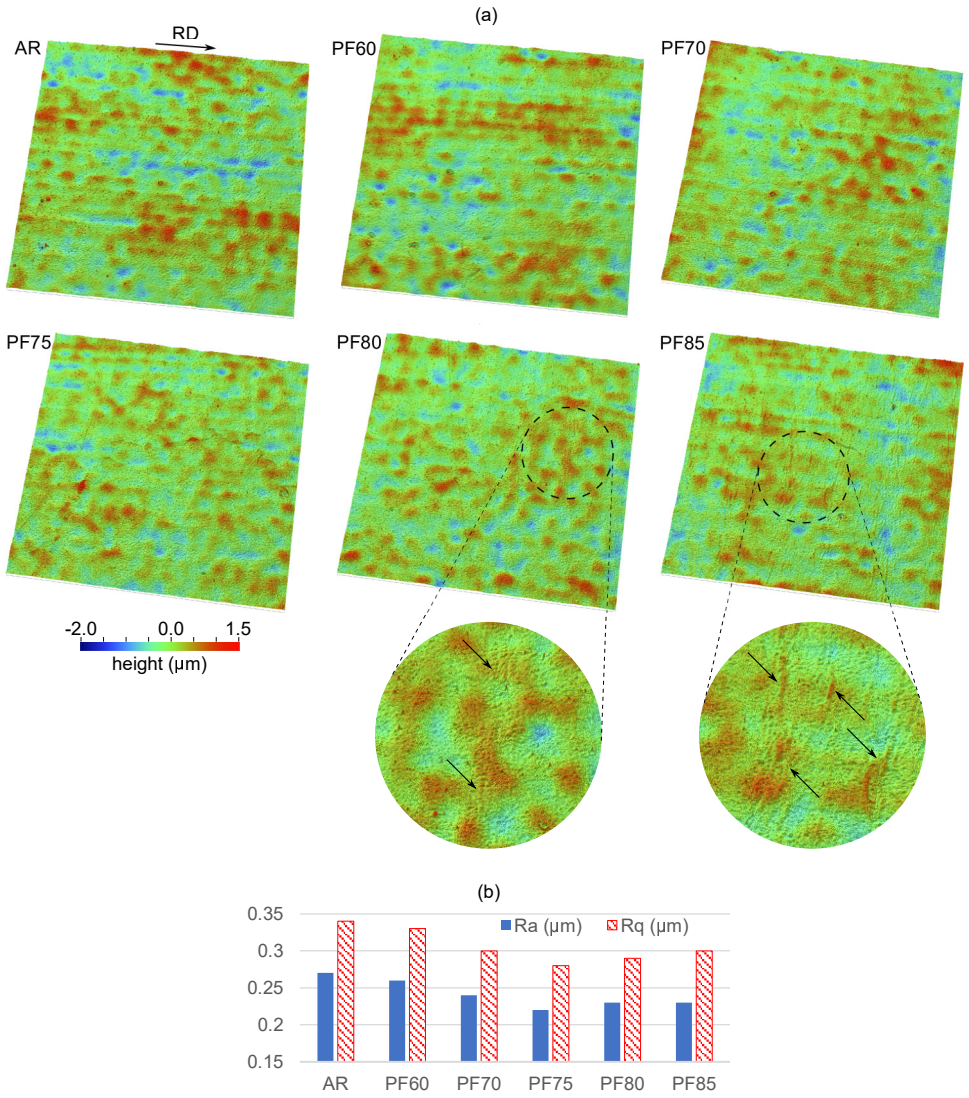

Figure 2.7. 3-D surface measurements on the area of 10 mm x 10 mm of specimens: (a) surface profiles and (b) surface roughness values of specimens with as-received and five PF conditions. Arrows in (a) indicate fluting defects. Ra and Rq in (b) represent the average roughness and the root mean square roughness.

also indicate the emergence of surficial defects at these PF conditions (Fig.2.7b). Generally, the roughness values decrease as PF increases because the rolls flatten the surface of specimens more with a higher pressure. In Fig.2.7b, however, it can be observed that both Ra and Rq roughness metrics increase from 75% PF condition, suggesting the surficial defects begin to appear around this roller-leveling condition. These results, which have hardly been found in previous studies, demonstrate that it is more appropriate to determine the maximum PF condition without surficial defects from the surface roughness data rather than from simple visual inspection.

The uniaxial tension tests at the crosshead speed of 6 mm/min are then conducted for these roller-leveled PLCS materials where three uniaxial tension specimens are extracted for each PF condition. The stress-strain responses and their YPP-related properties are depicted in Fig.2.8. As expected, all YPP-related properties decrease with PF (except for 60% PF condition) compared to the as-received condition because the higher PF condition induces the larger plastic strains by enlarging the plastic region from outer surface to neutral surface. However, the YPP cannot be entirely disappeared even with the maximum PF condition due to the remaining elastic region around the neutral layer. In the strain hardening region, the higher hardening stresses are observed for materials processed with larger PF conditions as the strain hardening is dependent on the amount of induced plastic strains.

It is surprising that YPP-related properties of specimens roller-leveled with 60% PF condition are larger than those of unprocessed materials, which has never been reported previously to the best of authors' knowledge. The increased YPP-related properties might be because of the reduction of residual stresses induced by high temperature during the coating process of PLCS. The reduction of residual stresses by the roller-leveling process was proven experimentally in Park et al. (2006) where the residual stresses in a hot rolled flat plate were shown to be reduced by half when roller-leveled with 70% PF condition. From the experiment of Hutchison (1957), it can be inferred that stress concentration that may occur near a region of residual stresses in uniaxial tension

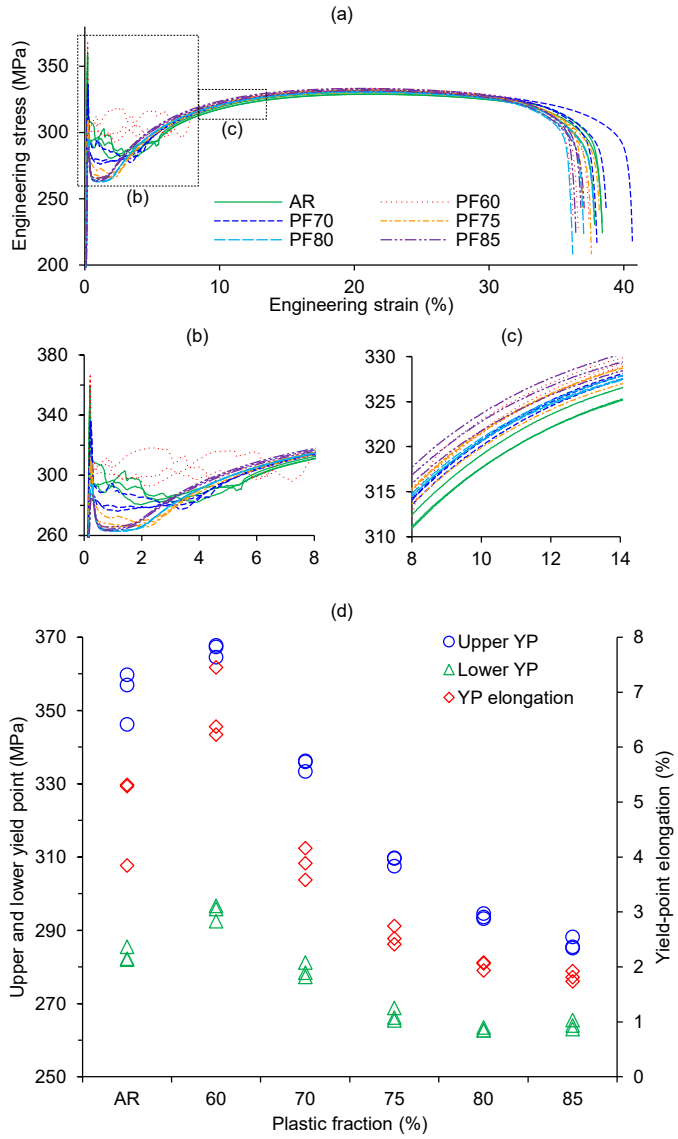

Figure 2.8. Uniaxial tension tests of roller-leveled materials at the crosshead speed 6 mm/min: (a) stress-strain responses; (b)-(c) detail parts of (a); and (d) corresponding YPP-related properties.

lowers the upper yield point. Van Rooyen (1971) also showed that the upper yield point can be drastically increased without any stress concentration in a tensile specimen. So, the reduction in residual stresses can effectively raise the upper yield point leading to

the increase of lower yield point and yield-point elongation as a consequence. Hence, it is presumed that the roller-leveling process has two effects: inducing plastic strains (or mobile dislocations) and reducing residual stresses each of which exerts an opposite influence on the YPP-related properties. Results suggest that the effect of residual stress reduction might be dominant in relatively light roller-leveling conditions while that of induced mobile dislocations governs the YPP-related properties in more severe processing conditions. Nevertheless, more systematic and comprehensive experiments are required to confirm this conjecture, which is out of the scope of this study.

2.1.4 V-bending test

To investigate the effect of roller-leveling conditions on the fluting, the v-bending experiments as depicted in Fig.1.3a are carried out using a mechanical servo press. The lower tool is fixed as a die and the upper tool moves downward as a punch. Rectangular specimens that are 100 mm long, aligned to the RD, and 50 mm wide are used. First, as-received PLCS without roller-leveling process is tested at four punch speeds of 5, 10, 15 and 20 strokes per minute (SPM) in order to study the rate dependency of the fluting. Experiments are performed three times at each punch speed. Then, three specimens are extracted from roller-leveled PLCS materials for each PF condition and tested at the punch speed of 10 SPM to examine the effect of roller-leveling conditions. The total stroke of the punch is 250 mm and the punch touches the specimen at the last stroke of 28.54 mm. The profiles of the punch speed during the last stroke of 29.70 mm are plotted in Fig.2.9.

The deformed specimens after the v-bending experiments are shown in Fig.2.10a and b. Deformed shapes of as-received specimens (Fig.2.10a) indicate that the fluting occurs at all punch speeds, but the rate effect on the amount of fluting is hardly identified by simple visual inspection. The effect of roller-leveling condition on the fluting defect is, on the contrary, clearly seen in the deformed specimens (Fig.2.10b) as the radius of curvature increases as PF increases. Interestingly, deflection lines where the slope of

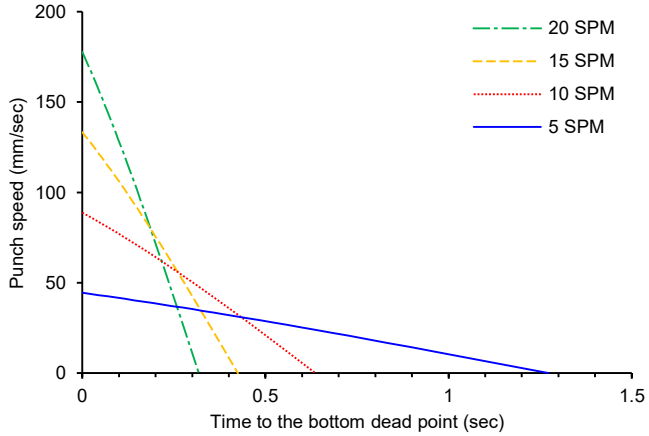

Figure 2.9. Profiles of the punch speeds during the last stroke of 29.70 mm in the v-bending test.

the straight part suddenly changes are observed for both sides at all punch speeds. They are induced by contact between the punch and the specimen after the fluting occurs as illustrated in Fig.2.10c. Meanwhile, the deflection lines in roller-leveled specimens are not observed in higher PF conditions where the fluting does not occur. In order to analyze the deformed shape of specimens more quantitatively, the bottom surface of each specimen is scanned using the Metris LC-100 line laser probe. The mid-sectional curves along the longitudinal direction are then obtained from the scanned data. The deformed shape of mid-sectional curves is characterized by the radius of curvature R, the bending angle A and the deflection point denoted in Fig.2.10d. The datum point in Fig.2.10d is the intersection of two lines each of which is obtained by connecting two points on the curve at 5 mm and 15 mm from the closest end of the curve. The radius of curvature R is calculated by nonlinear least-square fitting to a circle using the data points in the range of $-2.5 \leq x \leq 2.5$. The bending angle A is the angle between two lines, one from two points at $x = 20$ and $x = 30$ and the other from two points at $x = -20$ and $x = -30$.

The mid-sectional curves for as-received specimens tested with four punch speeds are drawn in Fig.2.11a and the corresponding R and A quantities are plotted in Fig.2.11d.

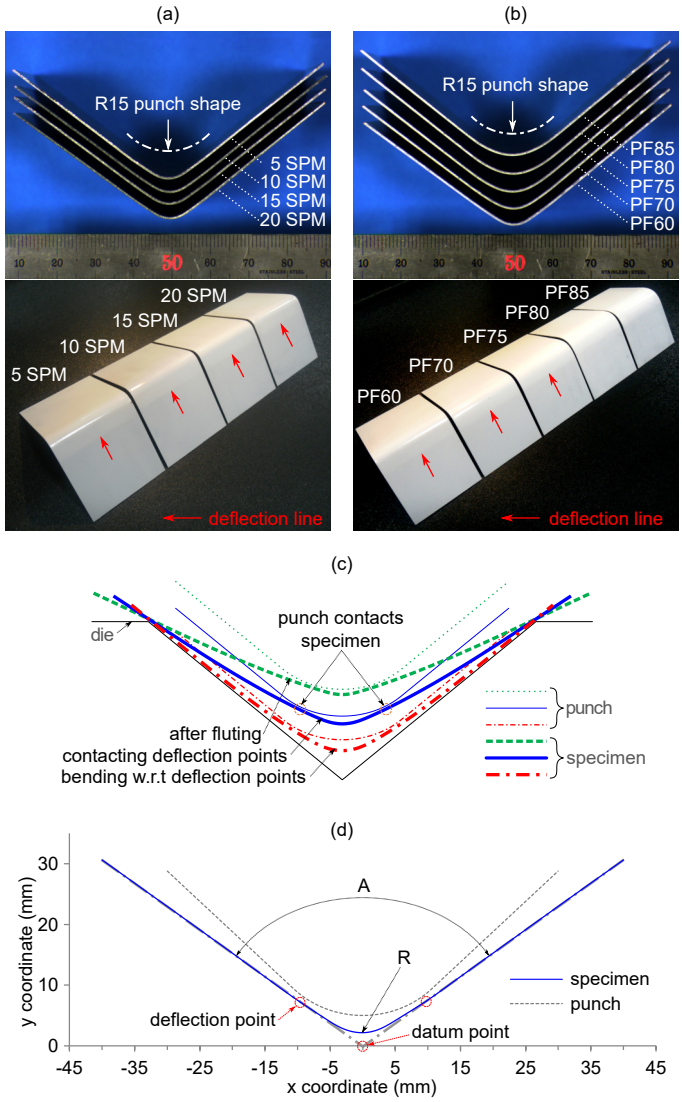

Figure 2.10. Deformed specimen samples after the v-bending test: (a) as-received PLCS with four different punch speeds; (b) roller-leveled PLCS with five PF conditions; (c) contact states between the punch and the specimen in the test; and (d) definition of the radius of curvature (R) and the bending angle (A) of a mid-sectional curve. Red arrows in (a) and (b) indicate the deflection lines. While they are marked at one side surface, the deflection lines exist at the other side surface as well.

In Fig.2.11a, the occurrence of flutings can be perceptibly seen in all cases by comparing

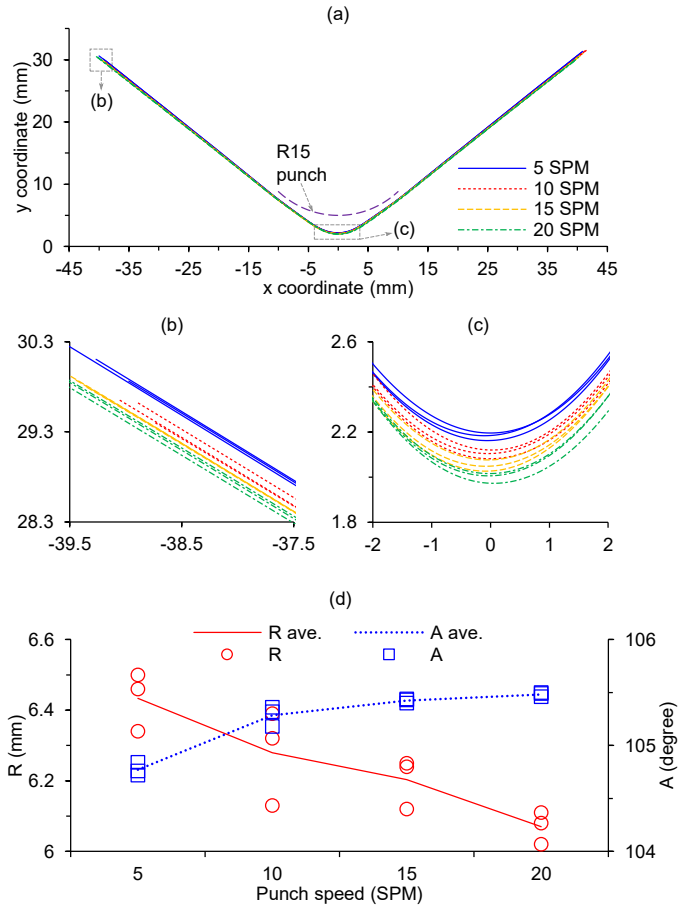

Figure 2.11. V-bending test results for as-received specimens tested with four punch speeds: (a) mid-sectional curves; (b)-(c) close-up views of mid-sectional curves; and (d) the measured radius of curvature R and bending angle A.

the curvature of the specimen with the R15 punch profile. All mid-sectional curves in Fig.2.11a are positioned such that their datum points are located at the origin. Measured radii of curvature are much smaller than the punch radius due to fluting and they are decreasing slightly with the punch speed as YPP properties increase with it. Dependence of the bending angle on the punch speed seems to be negligible as its difference is less than 1 degree. While deflection points are hardly recognized in Fig.2.11a, they can be

easily identified near $x = \pm 10$ in the plot of tangent slopes for the mid-sectional curves as shown in Fig.2.12. Here, we can clearly see the formation of two straight regions

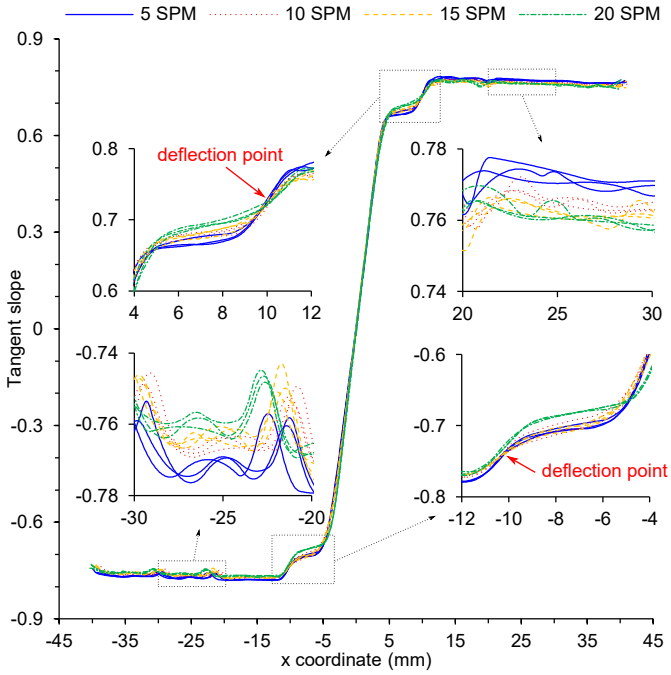

Figure 2.12. Tangent slope of the mid-sectional curves for as-received specimens tested with four punch speeds.

(corresponding to constant slope) about the deflection point on each side.

The mid-sectional curves for roller-leveled specimens process with five PF conditions and the corresponding R and A quantities are shown in Fig.2.13. The reduction of the fluting by the roller-leveling process can be visually recognized as in Fig.2.13a and c. With high PF conditions, the radius of curvature of roller-leveled specimens becomes closer to the punch radius. Except for 60% PF condition which turns out to increase the YPP-related properties in the uniaxial tension test, the radius of curvature increases with PF from approximately 6.3 mm for as-received specimens on average to 11.2 mm for specimens processed with 85% PF condition. The increase of the radius of curvature from 70% to 80% PF condition is about three times higher than that

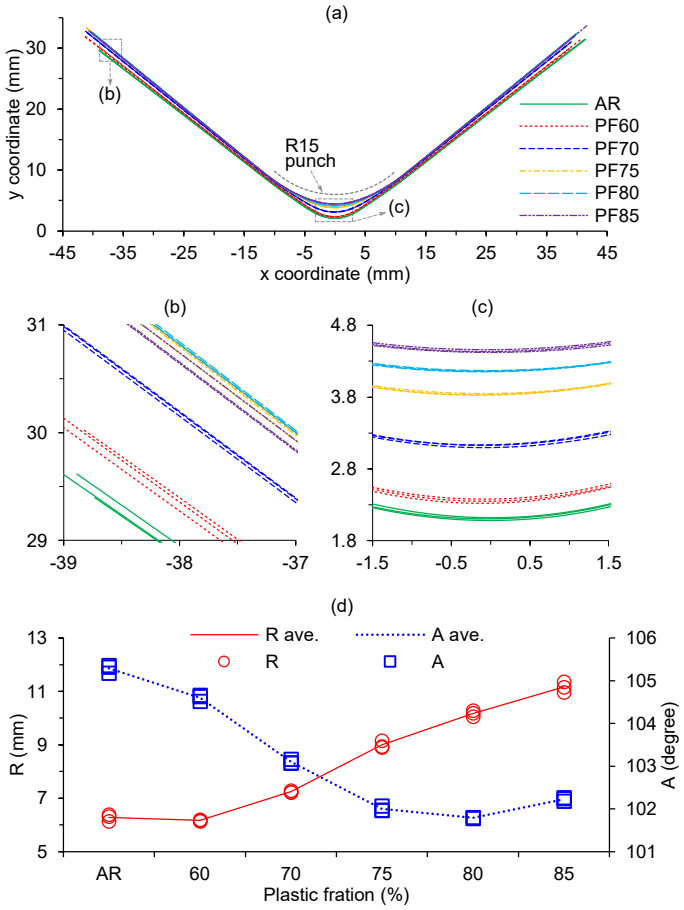

Figure 2.13. V-bending test results for roller-leveled specimens tested with five PF conditions: (a) mid-sectional curves; (b)-(c) close-up views of mid-sectional curves; and (d) the measured radius of curvature R and bending angle A. The punch speed is 10 SPM.

from 60% to 70% PF condition. A slightly decreased radius of curvature in the 60% PF condition compared to the as-received condition agrees with the increased YPP properties in uniaxial tension test for the same PF condition. The bending angle A is, on the other hand, decreasing slightly with PF even though R is increasing. It might be because the bending angle A can be affected by not only the radius of curvature R but also the amount of plastic strain induced during the roller-leveling process de-

termining the amount of springback. With lower PF conditions, plastic deformation is more concentrated on the fluting region resulting in higher strain hardening there. As a result, the bending angle A becomes bigger due to larger springback. As the PF condition in the roller-leveling process gets higher, the curved region becomes wider with a relatively lower strain hardening state leading to a reduction in the amount of springback. Moreover, the disappearance of deflection lines can be observed as the PF condition gets higher as shown in Fig.2.10b from the plot of tangent slopes calculated for these specimens. In Fig.2.14, the plateau begins to disappear with the 70% PF condition and becomes unnoticeable from the 80% PF condition.

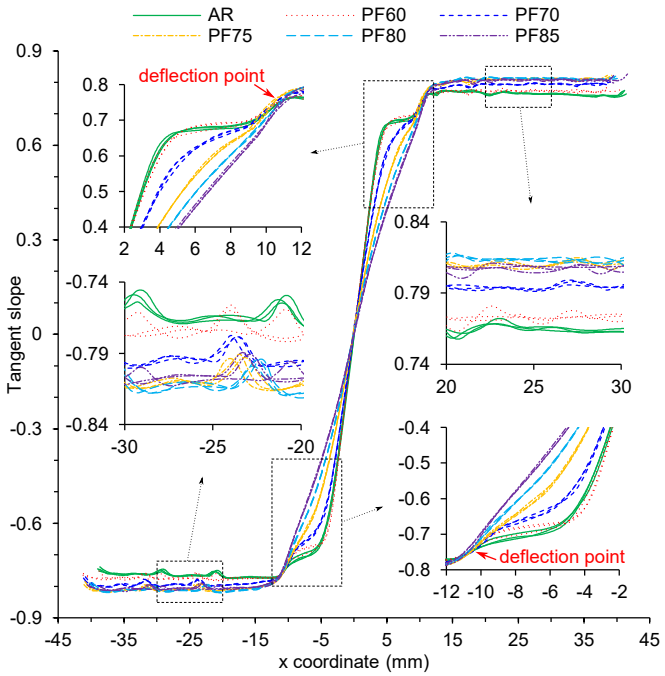

Figure 2.14. Tangent slope of the mid-sectional curves for roller-leveled specimens tested with five conditions.

2.2 Experimental observations for static dent resistance considering BH behavior with 490DP

Experimental procedures for uniaxial tension and uniaxial tension-compression cases are listed in Table 2.2. Note that for the 'T only' and 'T-C' cases just skip the unloading

Table 2.2. Procedure for uniaxial tension and uniaxial tension-compression.

Case	pre-strain (%)	BH temperature (°C)	BH time (min)
T only			
T-U-BH-T	2.0	100, 150, 200	20
T-U-BH-T	2.0	200	5, 20, 35
T-U-BH-T	2.0, 3.0, 4.0	200	35
T-U-BH-C	2.0, 3.0, 4.0	200	35
T-C	2.0, 3.0, 4.0		

T: tension, U: unloading, BH: bake hardening, C: compression

and BH steps. The temperature history for all BH operations are shown in Fig.2.15.

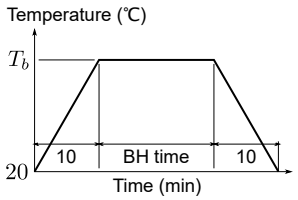

Figure 2.15. Temperature history for the BH operations. T_b denotes BH temperature.

2.2.1 Uniaxial tension test with BH

The dimensions of 490DP uniaxial tension specimen are the same as those in Fig.2.1 except for the shoulder radius which is 20 mm, not 12.7 mm. Uniaxial tension experiments are carried out using the same machine with the PLCS experiments. The tests are repeated three times for the same condition, and a representative response of the

repeated results is selected and used in the present chapter.

The stress-strain responses at the crosshead speed of 6 mm/min in the experiment for the rolling, transverse, and diagonal directions of the specimen are plotted in Fig.2.16. The responses show that yielding is anisotropic, and the response of the transverse

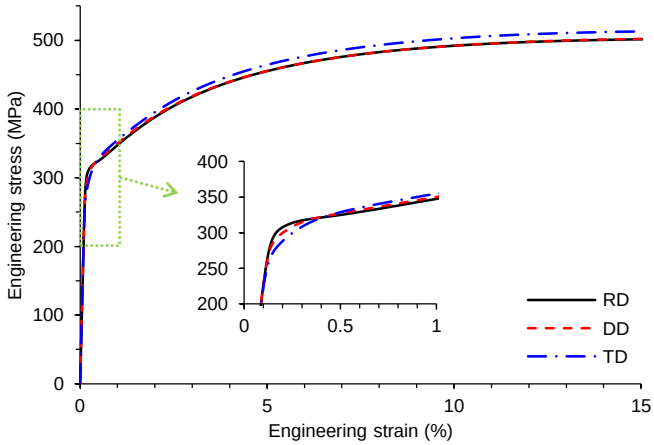

Figure 2.16. Directional stress-strain responses in uniaxial tension test at the crosshead speed of 6 mm/min.

direction has slightly higher stress levels than those of the other directions which are almost identical beyond the strain of 5%. The Lankford coefficients for each direction are recorded as $r_{RD} = 0.937$, $r_{DD} = 0.973$, and $r_{TD} = 1.085$, all measured at the engineering strain of 15%. Despite the anisotropic characteristics of this material in these directional tests, remaining uniaxial tension and uniaxial tension-compression tests are all conducted in the rolling direction, and the numerical analysis part of the present BH study assumes material isotropy for numerical simplicity. The response of the rolling direction is defined as an as-received case in the subsequent uniaxial tension experiments.

The rate-dependency of the material is also examined in the uniaxial tension tests with the crosshead speed of 0.6, 6, and 30 mm/min as shown in Fig.2.17. Here, the curve of the crosshead speed of 6 mm/min is the same as the as-received case (RD

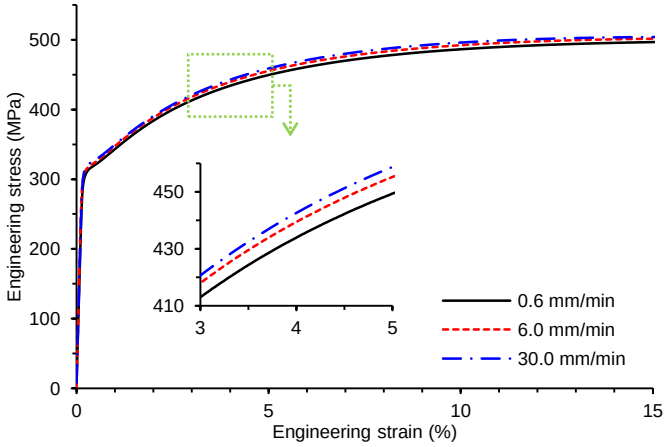

Figure 2.17. Stress-strain responses in uniaxial tension test at the crosshead speed of 0.6, 6 and 30 mm/min.

in Fig.2.16). Although the rate-dependency is clearly observed in the tests, the stress difference between 0.6 and 30 mm/min in the strain hardening region is not so high as about 10 MPa. Note that subsequent uniaxial tension and uniaxial tension-compression experiments are all conducted at the crosshead speed of 6 mm/min unless specified.

Uniaxial tension experiments including BH operation are carried out to investigate the BH behavior of the material in the uniaxial tensile case. The BH conditions used in these experiments are the same as the conditions 'T-U-BH-T' shown in Table 2.2. Thus, the test procedure consists of tension as pre-strain, unloading, BH, and tension. The BH temperature according to the BH time for these conditions follows the temperature history in Fig.2.15. Firstly, stress-strain responses according to BH temperature are plotted with the as-received case in Fig.2.18. Pre-strain applied to these tests is 2%. The highest temperature case apparently shows the yield-point elongation of around 2% with the highest upper yield point and the highest stress level in the strain hardening region, while the other temperature cases show relatively weaker YPP. In all cases, the stress level of the strain hardening region is higher than the as-received condition.

Next stress-strain responses drawn in Fig.2.19 and Fig.2.20 are for the BH time of

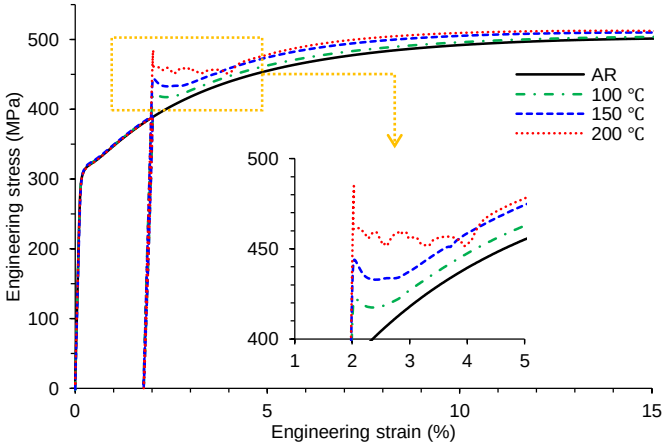

Figure 2.18. Stress-strain responses in uniaxial tension test with BH temperature of 100, 150, and 200 °C for BH time of 20 min and pre-strain of 2%. 'AR' denotes the as-received condition.

5, 10, and 20 min at the BH temperature of 100 °C and for the BH time of 5, 20 and 35 min at the BH temperature of 200 °C, respectively. In Fig.2.19, it is observed that the

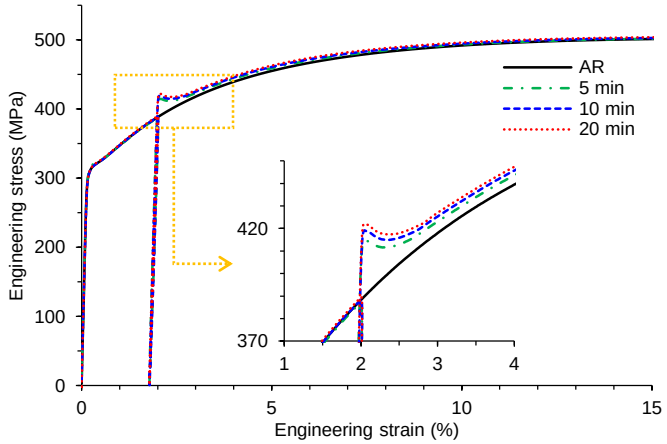

Figure 2.19. Stress-strain responses in uniaxial tension test for BH time of 5, 10, and 20 min at BH temperature of 100 °C and pre-strain of 2%. 'AR' denotes the as-received condition.

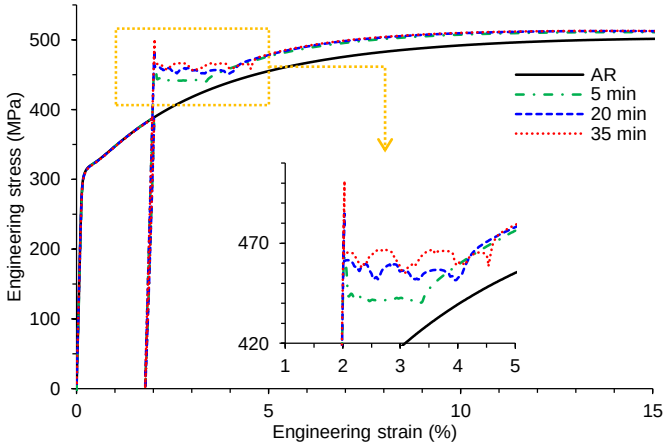

Figure 2.20. Stress-strain responses in uniaxial tension test for BH time of 5, 20, and 35 min at BH temperature of 200 °C and pre-strain of 2%. 'AR' denotes the as-received condition.

YPP is not strong but the upper and lower yield points are slightly elevated according to the BH time. The stresses in the strain hardening region are similar despite that their difference with respect to the BH time is exhibited in the detail graph. In Fig.2.20, all three BH time cases obviously reveal the yield-point elongation which escalates as the BH time increases. The upper yield point is also elevated as the BH time increases. However, the stress level in the strain hardening region is very similar to each other. When the minimum cases in Fig.2.18 and Fig.2.20 are compared, it can be found that the BH condition of 200 °C and 5 min provide stronger YPP than that of 100 °C and 20 min.

The last stress-strain responses are plotted in Fig.2.21 showing the BH behavior according to the pre-strain. As the pre-strain increases, the upper and lower yield stress are increased because the starting point of BH is located in the strain hardening region, whereas the BH stress is decreased. The effect of BH temperature, BH time, and pre-strain on the BH behavior identified in the present uniaxial tension experiments might be well agreed with the result of many previous works of literature such as Elsen and

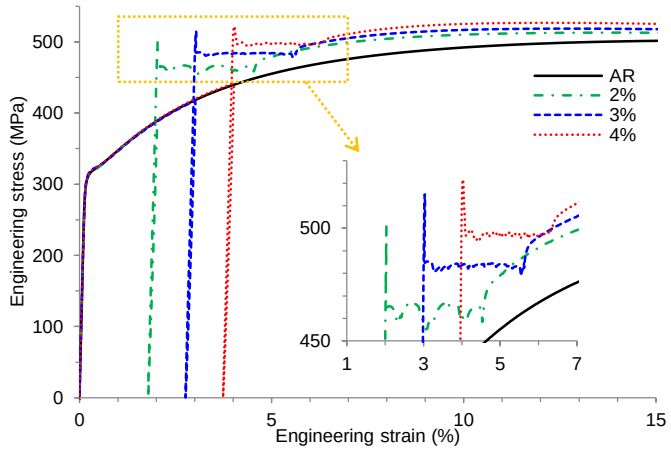

Figure 2.21. Stress-strain responses in uniaxial tension test with pre-strain of 2, 3, and 4%. The BH temperature and time are 200 °C and 35 min, respectively. 'AR' denotes the as-received condition.

Hougardy (1993) and De et al. (2001).

With the present uniaxial tension tests of various BH conditions, the evolution of elastic modulus is investigated. The elastic moduli with respect to the pre-strain are obtained before and after BH operation as shown in Fig.2.22. The averaged values of the moduli are similar to the exponential curve which fitted the experimental degradation of the uniaxial chord modulus for 490DP in Lee et al. (2016) even though they did not include BH operation for their measurement of the chord modulus. So, the effect of BH operation on the elastic modulus recovery might be negligible. And this effect is also hardly observed in Fig.2.23. As the BH condition changes, the elastic modulus does not show a certain tendency. The exponential curve equation in Fig.2.22 is expressed as

$$E = E_0 - (E_0 - E_{sat})[1 - \exp(-\xi_E \bar{\varepsilon})], \tag{2.4}$$

where E_0, E_{sat}, and ξ_E denote the initial elastic modulus, the saturated modulus, and the rate of the degradation, respectively. The corresponding parameters are listed in Table 2.3.

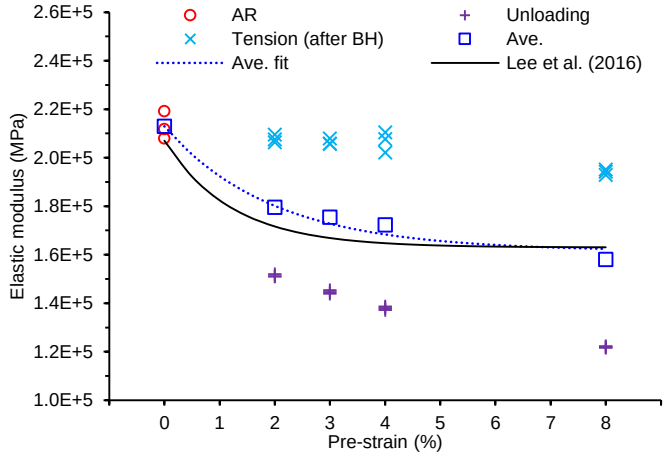

Figure 2.22. Degradation of elastic modulus as a function of pre-strain in uniaxial tension before and after BH operation. The BH temperature and time are 200 °C and 35 min, respectively.

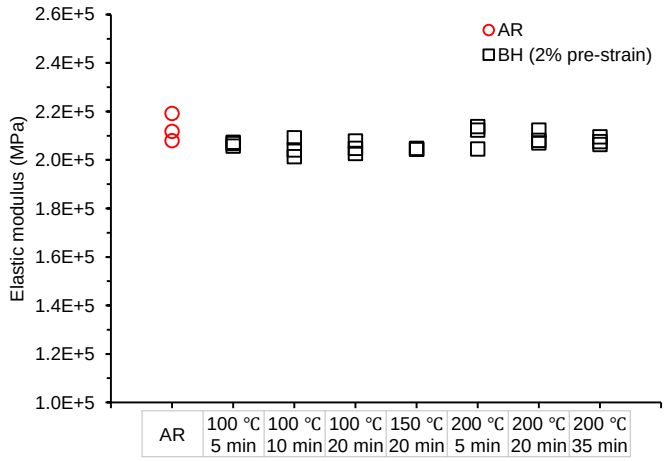

Figure 2.23. Elastic modulus of various BH conditions at the pre-strain of 2%.

Table 2.3. Elastic modulus parameters.

	E_0 [GPa]	E_{sat} [GPa]	ξ_E
Present (Ave. fit)	212.9	161.5	51
Lee et al. (2016)	207.0	163.0	82

2.2.2 Uniaxial tension-compression test with BH

Uniaxial tension-compression tests combined with BH operation are performed for the pre-strain of 2, 3, and 4% using the same machine for the uniaxial cyclic tests of PLCS. The tests are repeated at least three times for the same condition, and the result responses are averaged. The dimensions of the test specimen are the same as Fig.2.3 except for the thickness and the gauge length, which are 0.7 mm and 25 mm, respectively. The clamping force of 300 kgf is applied to obviate any instability during compression. The test conditions are the same as the conditions 'T-U-BH-C' and 'T-C' listed in Table 2.2. Hence, the test procedure with BH consists of tension as pre-strain, unloading, BH, and compression. The procedure without BH is just tension and compression. The compressive engineering strains that terminate the tests are 2, 3, and 4% for the pre-strain of 2, 3, and 4%, respectively. The BH temperature according to the BH time follows the temperature history in Fig.2.15 with the BH temperature of 200 °C and the BH time of 35 min.

Similarly as the experiments of PLCS, according to two equations introduced from Boger et al. (2005) and Cao and Wang (2000), the maximum attainable compressive true strain is calculated as about 0.151 for the gauge width 15 mm, and the corresponding clamping force estimated as about 541 kgf. Nonetheless, the clamping force of 300 kgf is used to minimize frictional and biaxial effects on the specimen. With this clamping force, the maximum compressive true strain can be about 0.080. Although this value is smaller than the current maximum compressive true strain of 0.083, buckling did not occur in all compression tests. Teflon sheets of 0.1 mm thickness are affixed on both sides of the specimen gauge section for minimizing the frictional effect. Referring to Boger et al. (2005), the obtained stress-strain raw data is corrected to remove the frictional effects from them with the friction coefficient of 0.080-0.095 so that the corrected curves in the tensile region can match to a uniaxial tension curve. The biaxial effects are also corrected by using Eq.(2.1). This biaxial effects can be ignored if they are considered to be negligibly small. In these tests, the normal stress induced by the

clamping force in the gauge section (30 mm x 15 mm) is about 6.5 MPa, and the difference between before and after the corrections is around 3.2 MPa.

The corrected engineering stress-strain curves are shown in Fig.2.24. The ‘T only’

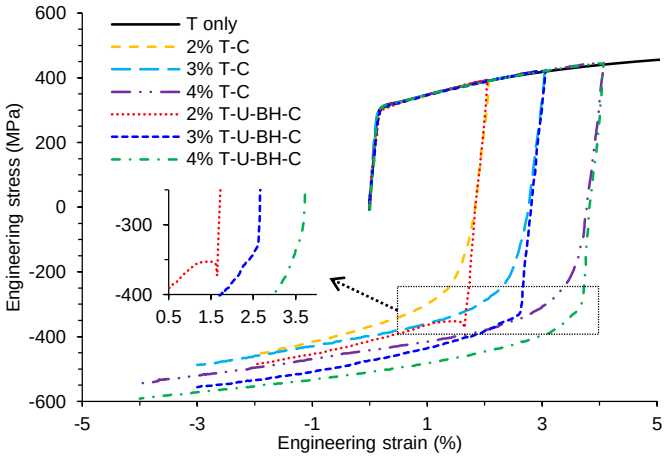

Figure 2.24. Engineering stress-strain responses in uniaxial tension-compression test with pre-strain of 2, 3, and 4%. For the ‘T-U-BH-C’ cases, BH temperature and BH time are 200 °C and 35 min, respectively. ‘T only’ denotes tension only.

curve is the same as the ‘AR’ of Fig.2.18-2.21 generated from the uniaxial tension tests which have twice a higher strain rate than the uniaxial tension-compression tests at the same crosshead speed due to the difference of the specimen gauge length. Although the strain rates are different, the rate dependency in this strain rate range might be negligibly small. Therefore, the ‘T only’ curve can be used in the correction of the other curves, and as a result, the curves in the tension are well matched with each other after correcting the frictional and biaxial effects. In the ‘T-C’ cases, the Bauschinger effect is observed while the workhardening stagnation may not occur. This experimental evidence of no workhardening stagnation in 490DP, as well as the clearly captured workhardening stagnation in the experiments of PLCS, conforms to the experimental result of Yoshida et al. (2002). Compression after BH brings the YPP only clearly in the 2% pre-strain case. However, the intensity of the YPP is quite smaller than the tension

cases. Furthermore, in the other pre-strain case with BH, the YPP is almost disappeared despite that the transient regions from elastic to plastic are relatively sharper than the 'T-C' cases. These weaker responses of the YPP might be the frictional effects induced by the clamping force. The sharp upper yield point and abrupt yield drop seem to be concealed by the friction force. Compressive behaviors after BH were rarely reported in the past literature, and the present experimental investigation could be the first one to the best of authors' knowledge. In order to check the permanent softening behavior of the material, the curves of Fig.2.24 are converted to true values and symmetrized about the stress reversal points as plotted in Fig.2.25. The permanent softening is captured

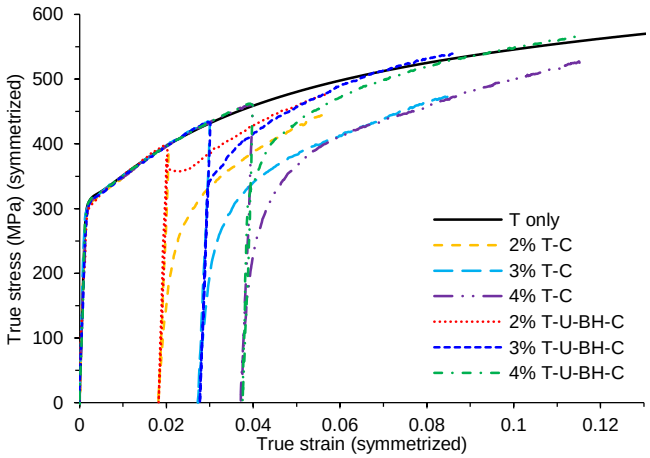

Figure 2.25. True stress-strain responses converted from Fig.2.24. The curves are symmetrized about the stress reversal points.

in all 'T-C' cases whereas BH cases with the pre-strain of 3 and 4% almost reach the stress level of uniaxial tension.

2.2.3 Static dent test with BH

Static dent experiments with 490DP are conducted by referring to SAE J2575 (Standardized Dent Resistance Test Procedure). Generic panels for the experiments are formed using a 300-tonne hydraulic press with tools illustrated in Fig.2.26a. The tool

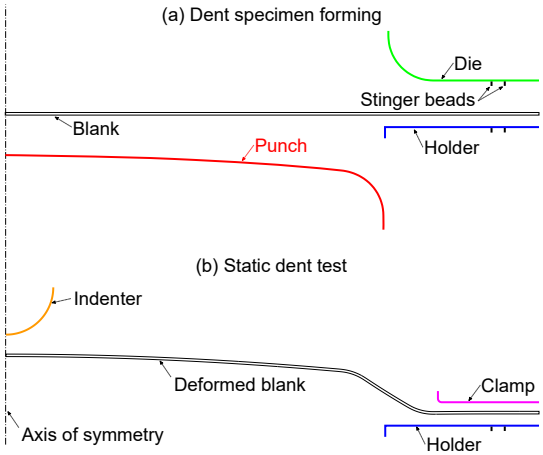

Figure 2.26. Schematics for (a) dent specimen forming and (b) static dent test. Dimensions are given in Fig.5.25.

dimensions given in Fig.5.25 are not exactly the same as those in SAE J2575. The generic panel whose initial size is 300 mm x 300 mm is bound by the die and the holder with the holder force of 100 tonnes during the die stroke of 16 mm. This stroke value is from a touch point between the fixed punch and the blank to the bottom dead point of the die. The die speed is 3 mm/sec. The die and holder have two sets of stinger beads, male in the die side and female in the holder side. These stinger beads can generate two small grooves around the deformed shape of the panel, and the grooves can be fitted to the holder of the static dent test as shown in Fig.2.26b. In the static dent test, the deformed panel fixed between the clamp and the holder is pushed by the spherical indenter of 25.4 mm diameter, and then unloaded. The speed and total displacement of the indenter are 2 mm/min and 6 mm, respectively.

Before the dent tests, the strains of the deformed panel are measured using a Grid Analyzer Model 100U of the FMTI systems Inc. for three specimens at the locations as marked in Fig.2.27a, and the measurement results are shown in Fig.2.27b. The circle diameter for the strain measurement is 2.5 mm, and the circle grid interval is 10 mm. The thickness strain e_3 values are calculated from plastic incompressibility. The RD

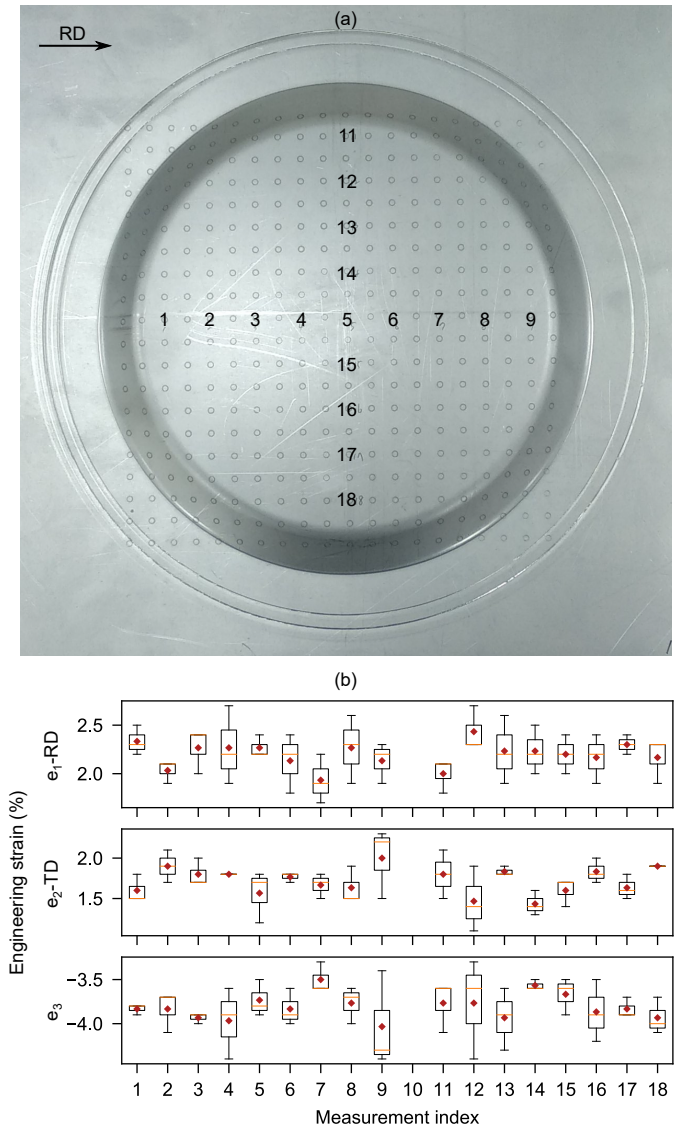

Figure 2.27. (a) Deformed panels and strain measurement points and (b) measurement results.

strain of 2.20% on average is higher than the TD strain of 1.72% on average due to material anisotropy whereas a certain trend of the strain distribution according to the

measurement location may not be observed. The relation

$$\frac{r_{TD}}{r_{RD}}\left(=\frac{1.085}{0.937}=1.158\right)=\frac{(d\varepsilon_{RD}/d\varepsilon_3)}{(d\varepsilon_{TD}/d\varepsilon_3)}=\frac{d\varepsilon_{RD}}{d\varepsilon_{TD}} \tag{2.5}$$

also supports the strain difference between the RD and TD strain as

$$\frac{d\varepsilon_{RD}}{d\varepsilon_{TD}}\approx\frac{\ln(1+e_{1,ave}/100)}{\ln(1+e_{2,ave}/100)}=1.276. \tag{2.6}$$

The thicknesses of the deformed panel are also measured with an ultrasonic thickness gauge of Krautkramer at the same locations as the strain measurement for three specimens. These thicknesses and calculated values from the thickness strain e_3 are plotted in Fig.2.28. The thickness of the as-received condition is measured as 0.699-

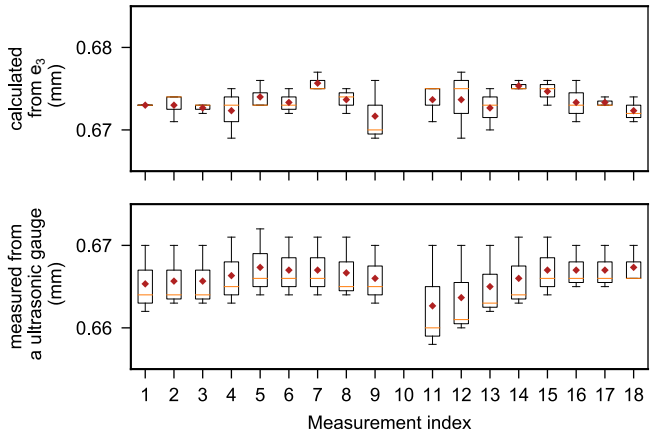

Figure 2.28. Measured thicknesses of the deformed panels with calculated values from e_3 of Fig.2.27.

0.701. The average measured thickness of the deformed panel is 0.666, and this value is different from the calculated value of 0.673 on average. This might be because of low accuracy in strain and thickness measurement.

The convex surfaces of the deformed panels are obtained by 3-D laser-scanning with the Steinbichler T-Scan pro laser scanner for three specimens. Sectional center curves in the RD and TD as drawn in Fig.2.29 are extracted from the 3-D scanned surface data. Note that the y values of the curves are shifted in order that the minimum

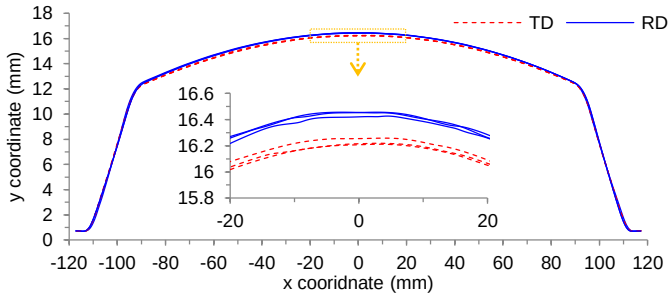

Figure 2.29. Sectional center curves extracted from the 3-D scanned surfaces of the deformed panels.

point of the curves becomes 0.7 mm. Accordingly, the top points of curves are different, and the RD curves are higher than the TD curves. The average amount of springback at the top points obtained from the curves in Fig.2.29 is 0.254 mm in the RD and 0.470 mm in the TD.

The static dent tests are conducted for the deformed panels after BH operation and those without BH operation. The BH conditions which take the BH temperature history in Fig.2.15 are 100 °C for 5, 10, and 20 min, 150 °C for 20 min, and 200 °C for 5, 20, and 35 min. So, two BH temperature cases with respect to the BH time and one BH time case with respect to the BH temperature are investigated for the dent resistance of the material 490DP. The tests are repeated three times for the same condition, and all test responses are plotted in Fig.2.30. In the same conditions, some curves show different force levels. As the BH condition becomes strong, the widths of the curves, which means the force difference between the forward and backward movement of the indenter, get narrower. Meanwhile, the overall shapes of the curves are barely changed between the BH conditions. Dent depth and maximum force defined in Fig.2.30a are drawn in Fig.2.31 according to the BH condition. Note that the dent depth is determined at the indenter force of 0.5 N. The dent depths are apparently decreased as the BH condition gets stronger. However, the maximum forces are quite scattered presumably due to experimental artifacts. Therefore, it can be shown that the

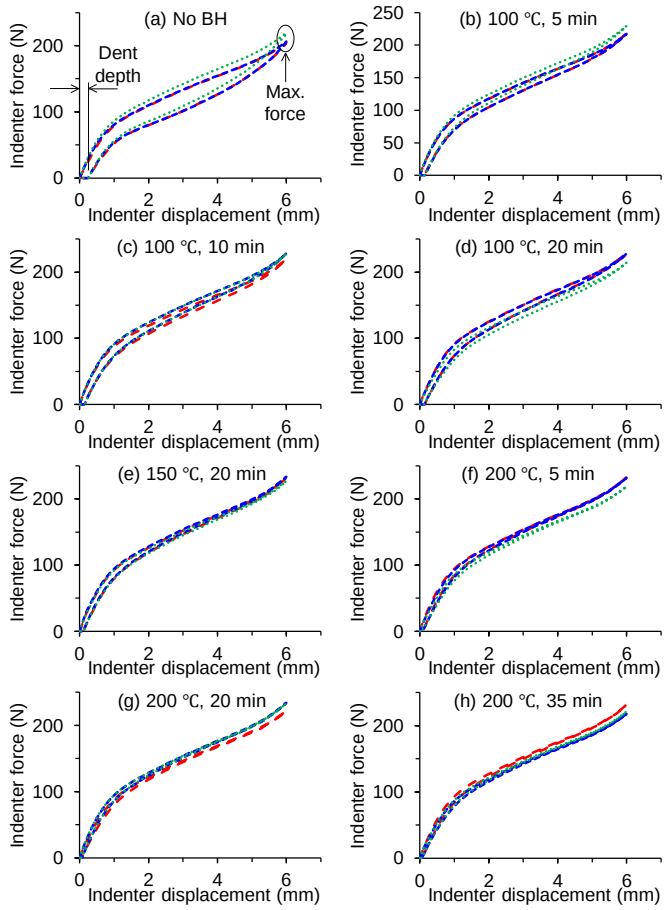

Figure 2.30. Experimental responses of dent test according to BH condition: (a) no BH condition and (b)-(h) BH conditions.

dent forces are more sensitive to experimental conditions than the dent depths. The following force-displacement responses are averaged for the same condition.

The averaged responses for the three BH temperatures are plotted as Fig.2.32. When the indenter pushes the deformed panels, the forces of the BH temperature of 150 and 200 °C follow almost a similar route and even reach nearly equivalent maximum points. While, when the indenter moves backward, higher BH temperature case reveals higher indenter force, and this difference might lead to the discrepancy of permanent dent depth. As expected, the case without BH records the minimum in the indenter force

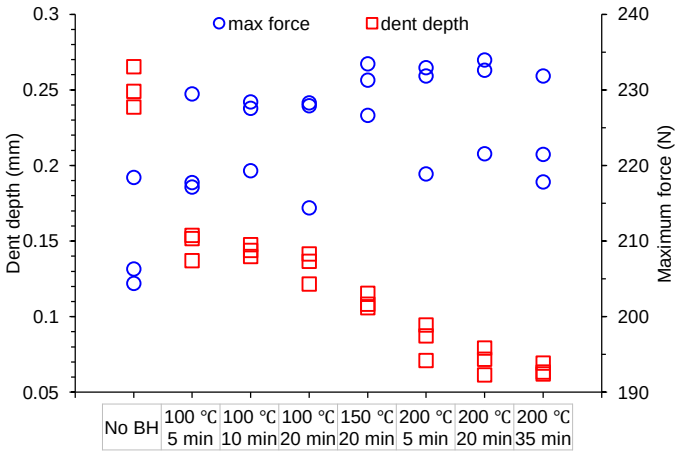

Figure 2.31. Dent depth and maximum force according to BH condition.

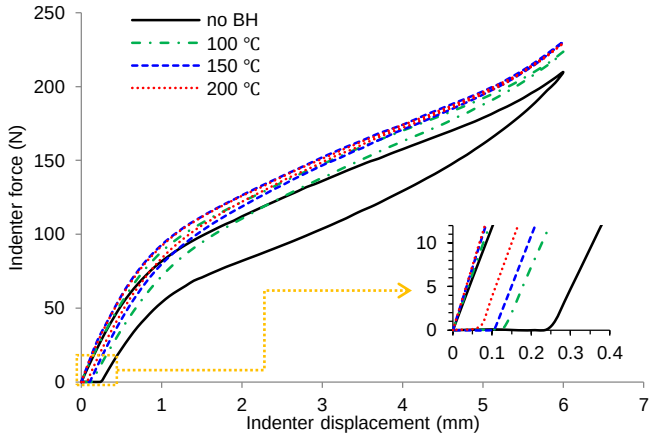

Figure 2.32. Averaged force-displacement responses with respect to the BH temperature. The BH time is 20 min.

and the maximum in the permanent dent depth.

The force-displacement responses for the three BH time are drawn in Fig.2.33-2.34. In Fig.2.33 with the BH temperature of 100 °C, two longer BH time cases have very similar force histories while the shortest BH time case exhibits a weaker response than the other two cases as expected. The permanent dent depth is decreased as the BH time increases, and this trend is clearly identified in Fig.2.31. In Fig.2.34 with the BH

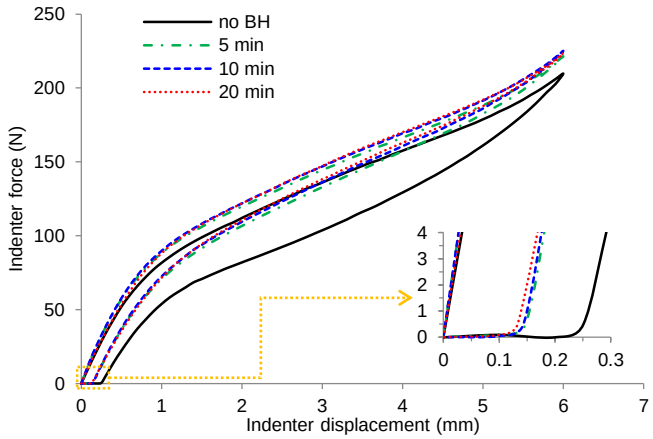

Figure 2.33. Force-displacement responses with respect to the BH time. The BH temperature is 100 °C.

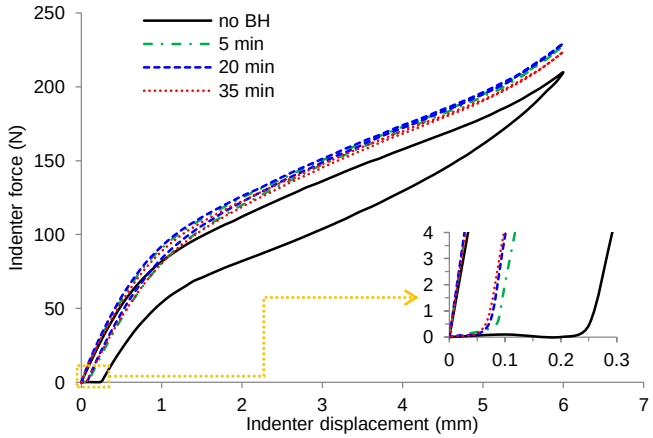

Figure 2.34. Force-displacement responses with respect to the BH time. The BH temperature is 200 °C.

temperature of 200 °C, the curve widths become narrower than those in Fig.2.33 as expected. However, the force responses in this BH temperature of 200 °C hardly show a certain tendency with respect to the BH time as already mentioned with Fig.2.31. Whereas the dent depth is decreased as the BH time increases. When comparing the dent depth difference between Fig.2.32 and Fig.2.33-2.34, the depth is more sensitive

to the BH temperature than the BH time. This characteristic is apparently agreed with the stress-strain responses in the uniaxial tension tests as exhibited in Fig.2.18-2.20.

2.3 Summary

In this chapter, comprehensive and in-depth investigations for the fluting defect and its reduction by the roller-leveling process were conducted experimentally, the experiments for the BH behavior of 490DP was also synthetically handled with uniaxial tension, uniaxial tension-compression, and static dent cases. Uniaxial tension and cyclic experiments were carried out first to check the rate dependency of the YPP and its cyclic behaviors as well as to determine the material constants of the YPP constitutive model for PLCS. In the roller-leveling test performed with five PF conditions, surficial defects in the material processed with higher PF conditions were identified by both visual inspection and 3-D surface profile measurement. Calculating the surface roughness values from the 3-D surface measurement as a function of induced plastic strains seems useful to determine the proper PF condition without leading to surficial defects. YPP properties of roller-leveled specimens decreased in general as induced plastic strains increased. Exceptionally, they were slightly increased with 60% PF condition compared to those of the as-received specimen probably due to the dominant effect of residual stress reduction over the plastic strain addition in a low PF condition. In the v-bending tests, specimens with the YPP exhibited the fluting characterized by much smaller radii of curvature compared with the punch radius. This fluting resulted in the presence of the deflection point near the contact point between the punch and the specimen. As YPP-related properties were reduced by the roller-leveling process, these fluting-related features disappeared.

In the uniaxial tension tests for the BH behavior of DP steel, the stress-strain responses according to various BH conditions were analyzed, and it was found that the responses with respect to the BH temperature exhibited more obvious difference than

those with respect to the BH time. The BH responses and the degradation of the elastic modulus according to the pre-strain were also studied in the uniaxial tension tests. With the fixed condition of BH temperature and time, the uniaxial tension-compression tests were carried out to investigate the Bauschinger effect before and after the BH operation. Only the pre-strain of a 2% case gave clear YPP in the compression after BH. In the static dent experiments, the BH effects were examined using the deformed panels. As the BH conditions got stronger, there was no clear tendency in the maximum dent force while there was an apparent reduction in the dent depth. As identified in the uniaxial tension, the BH effect on the dent resistance was even explicitly observed in the BH temperature variations.

Chapter 3

Material Modeling

In this chapter, a constitutive material model for YPP, its implicit incremental formulation, and the coupling of a BH model with the YPP material model are presented. These are for investigating the capabilities of the model to predict the fluting defect in the v-bending experiments, studying the effect of roller-leveling conditions on it, and assessing the BH behavior in the static dent experiments. We adopt the Yoshida-2008 model as it can describe both the rate-dependency of the YPP and the cyclic behavior and develop its implicit form for efficient FE simulations. In this development, the original kinematic hardening rule in the Yoshida-2008 model is replaced with a simpler kinematic hardening rule suggested by Yoshida and Uemori (2003) for computational efficiency. An alternative kinematic hardening model to consider the true YPP behavior of Schwab and Ruff (2013) is also tested. We newly propose a robust stress integration method in the implicit formulation to overcome the difficulty in obtaining converged solutions. For the BH part of the model, a phenomenological BH model introduced in Das et al. (2014) is utilized for considering the two BH stages, the formation of the Cottrell atmosphere and the precipitation hardening.

3.1 Constitutive Model

3.1.1 YPP model

Basic assumptions of infinitesimal elastic deformation and finite plastic deformation for the present constitutive model approximate the rate of deformation $\dot{\boldsymbol{\varepsilon}}$ to

$$\dot{\boldsymbol{\varepsilon}} = \dot{\boldsymbol{\varepsilon}}^e + \dot{\boldsymbol{\varepsilon}}^p, \tag{3.1}$$

where $\dot{\boldsymbol{\varepsilon}}^e$ and $\dot{\boldsymbol{\varepsilon}}^p$ denote the elastic and plastic part of the rate of deformation, respectively. Based on the material embedded (or co-rotational) coordinate system, the objective rate $\mathring{\boldsymbol{\sigma}}$ of the Cauchy stress $\boldsymbol{\sigma}$ and $\dot{\boldsymbol{\varepsilon}}^e$ have the elastic relation expressed as

$$\mathring{\boldsymbol{\sigma}} = \mathbf{D} : \dot{\boldsymbol{\varepsilon}}^e, \tag{3.2}$$

where $\mathbf{D}$ stands for the elasticity tensor. Hereafter, $(\circ)$ is used for the objective rate.

The Yoshida-2008 model has the separate constitutive equations for two regions: the Lüders band (LB) region and the work hardening (WH) region, represented by the subscript l and w, respectively. They are expressed as the following equations:

$$\dot{\bar{\varepsilon}}_l = \frac{b\rho_m}{M}\left(\frac{\langle \bar{\sigma}_l - Y_l \rangle}{D_l}\right)^{n_e}, \tag{3.3}$$

$$\dot{\bar{\varepsilon}}_w = \frac{b\rho_m}{M}\left(\frac{\langle \bar{\sigma}_w - (Y_l + R_y) \rangle}{D_w}\right)^{n_e}, \tag{3.4}$$

where b, ρ_m, M and R_y are the magnitude of the Burgers vector, the mobile dislocation density, the Taylor factor, and the isotropic hardening stress, respectively. Here, Y_l, D_l, D_w and n_e are material constants. The angle bracket $\langle\cdot\rangle$ stands for the Macaulay bracket which can be defined as $\langle x \rangle = max\,(0, x)$ and allows to determine whether a current state is elastic or viscoplastic. The mobile dislocation density ρ_m is given as

$$\rho_m = \rho_t f_m, \tag{3.5}$$

with

$$\rho_t = \rho_0 + Z\bar{\varepsilon}^{\chi}, \tag{3.6}$$

$$f_m = f_{m0} + (f_{ma} - f_{m0}) \left[1 - \exp\left(-\lambda \bar{\varepsilon}\right)\right], \tag{3.7}$$

where ρ_t, f_m and ρ_0 are the total dislocation density, its mobile fraction and its initial value, respectively, and Z and χ are material constants. The initial and saturated values of f_m are f_{m0} and f_{ma}, respectively, and λ is a material constant. The effective stresses $\bar{\sigma}_l$ and $\bar{\sigma}_w$ are defined as

$$\bar{\sigma}_l = \sqrt{\frac{3}{2}\mathbf{s} : \mathbf{s}} \quad \text{and} \quad \bar{\sigma}_w = \sqrt{\frac{3}{2}\left(\mathbf{s} - \boldsymbol{\alpha}\right) : \left(\mathbf{s} - \boldsymbol{\alpha}\right)}, \tag{3.8}$$

where $\mathbf{s}$ and $\boldsymbol{\alpha}$ stand for the deviatoric stress of $\boldsymbol{\sigma}$ and the back stress, respectively. The effective plastic strains $\dot{\bar{\varepsilon}}_l$ and $\dot{\bar{\varepsilon}}_w$ are calculated using

$$\dot{\bar{\varepsilon}} = \sqrt{\frac{2}{3}\dot{\boldsymbol{\varepsilon}}^p : \dot{\boldsymbol{\varepsilon}}^p}. \tag{3.9}$$

The associated flow rule provides

$$\dot{\boldsymbol{\varepsilon}}^p = \dot{\bar{\varepsilon}}_l \mathbf{n}_l \quad \text{and} \quad \dot{\boldsymbol{\varepsilon}}^p = \dot{\bar{\varepsilon}}_w \mathbf{n}_w, \tag{3.10}$$

where $\mathbf{n}_l$ and $\mathbf{n}_w$ stand for the flow vectors defined as

$$\mathbf{n}_l = \frac{3}{2}\frac{\mathbf{s}}{\bar{\sigma}_l} \quad \text{and} \quad \mathbf{n}_w = \frac{3}{2}\frac{\mathbf{s} - \boldsymbol{\alpha}}{\bar{\sigma}_w}. \tag{3.11}$$

The WH mode has the same initial yield condition Y_l as the LB mode. In this thesis, Eq.(3.4) is modified to adopt the kinematic hardening model of Yoshida and Uemori (2003) and the modified equation for WH mode is given by

$$\dot{\bar{\varepsilon}}_w = \frac{b f_m \rho_t}{M}\left(\frac{\langle \bar{\sigma}_w - Y_w \rangle}{D_w}\right)^{n_e} \tag{3.12}$$

with

$$Y_w = Y_{w0} + (Y_{wa} - Y_{w0}) \left[1 - \exp\left(-\zeta \bar{\varepsilon}\right)\right], \tag{3.13}$$

where Y_{w0} and Y_{wa} denote the initial and asymptotic value of Y_w, respectively and ζ is a material constant. This modification enables the present model to capture a smaller lower yield point than the original kinematic hardening model. Alternatively, to

closely describe the true material behavior related to the YPP as stated in Schwab and Ruff (2013), Y_w can be also expressed as

$$Y_w = \frac{Y_{wa}}{2}\left[1 + \tanh\zeta\left(\bar{\varepsilon} - Y_{w0}\right)\right]. \tag{3.14}$$

Both models for kinematic hardening are tested in the present numerical studies.

The back stress $\boldsymbol{\alpha}$ for the kinematic hardening rule in Yoshida and Uemori (2003) is composed of $\boldsymbol{\beta}$, the center of the bounding surface, and $\boldsymbol{\theta}$, the relative position of the yield surface to the bounding surface, as

$$\boldsymbol{\alpha} = \boldsymbol{\beta} + \boldsymbol{\theta}, \tag{3.15}$$

where $\boldsymbol{\beta}$ and $\boldsymbol{\theta}$ evolve with

$$\mathring{\boldsymbol{\theta}} = C\left(\frac{2}{3}a\dot{\boldsymbol{\varepsilon}}^p - \sqrt{\frac{a}{\bar{\theta}}}\boldsymbol{\theta}\dot{\bar{\varepsilon}}\right), \tag{3.16}$$

$$\mathring{\boldsymbol{\beta}} = m\left(\frac{2}{3}b_1\dot{\boldsymbol{\varepsilon}}^p - \boldsymbol{\beta}\dot{\bar{\varepsilon}}\right), \tag{3.17}$$

Here,

$$a = B_0 + R_b - Y_{wa}, \tag{3.18}$$

$$\bar{\theta} = \sqrt{\frac{3}{2}\boldsymbol{\theta} : \boldsymbol{\theta}}, \tag{3.19}$$

where C, m and b_1 are material constants and B_0 denotes the initial size of the bounding surface. The isotropic hardening stress R_b changes as

$$\dot{R}_b = m\left(R_{sat} - R_b\right)\dot{\bar{\varepsilon}}, \tag{3.20}$$

where R_{sat} stands for the saturated value of R_b. Note that, Eq.(3.20) is only relevant when $\boldsymbol{\beta}$ meets the conditions presented in Yoshida and Uemori (2003) as

$$\begin{aligned} &g_\sigma\left(\boldsymbol{\beta}, \mathbf{q}, r\right) = \frac{3}{2}\left(\boldsymbol{\beta} - \mathbf{q}\right) : \left(\boldsymbol{\beta} - \mathbf{q}\right) - r^2 = 0 \quad \text{and} \\ &\frac{\partial g_\sigma}{\partial \boldsymbol{\beta}} : \mathring{\boldsymbol{\beta}} = \left(\boldsymbol{\beta} - \mathbf{q}\right) : \mathring{\boldsymbol{\beta}} > 0, \end{aligned} \tag{3.21}$$

where g_σ is the non-isotropic hardening surface whose center and radius are $\mathbf{q}$ and r, respectively. Otherwise, $\dot{R}_b = 0$. These conditions suggested in Yoshida and Uemori (2003) are required to represent the workhardening stagnation as observed in Yoshida et al. (2002). The evolution of $\mathbf{q}$ is assumed as

$$\mathring{\mathbf{q}} = \mu\,(\boldsymbol{\beta} - \mathbf{q}) \quad \text{where} \quad \mu = \frac{3}{2r^2}\,(\boldsymbol{\beta} - \mathbf{q}) : \mathring{\boldsymbol{\beta}} - \frac{\dot{r}}{r}. \tag{3.22}$$

Here, μ can be obtained by substituting $\dot{\mathbf{q}}$ into the consistency condition $\dot{g}_\sigma = 0$. And the evolution of r is assumed as

$$\begin{aligned} \dot{r} &= h\frac{3}{2r}\,(\boldsymbol{\beta} - \mathbf{q}) : \mathring{\boldsymbol{\beta}} \quad \text{when} \quad \dot{R}_b > 0, \\ \dot{r} &= 0 \quad \text{when} \quad \dot{R}_b = 0, \end{aligned} \tag{3.23}$$

where h $(0 \le h \le 1)$ is a material parameter related to the expansion rate of g_σ.

3.1.2 BH model

As previously explained in Chapter 1, the BH stress can be the summation of the two effects expressed as

$$\sigma_{BH} = \sigma_{Cott} + \sigma_{prec}, \tag{3.24}$$

where

$$\sigma_{Cott} = \frac{k_B T_b}{V_{act}} \ln\left[(1 - g_b)^{(1+\omega)}\,(1 + \omega g_b)\right], \tag{3.25}$$

$$\sigma_{prec} = 0.538\frac{G_{Fe} b {V_f}^{1/2}}{X_p} \ln\left(\frac{X_p}{2b}\right), \tag{3.26}$$

derived in Das et al. (2014). Here, σ_{Cott} and σ_{prec} are the stress increase in MPa by the Cottrell effect and the precipitation hardening, respectively. And these expressions are from the original references, Hartley (1966) and Gladman (1999).

In Eq.(3.25), k_B, T_b, and V_{act} denote the Boltzmann constant, BH temperature in °K, and the activation volume of the dislocation mechanism, respectively. A BH parameter ω varying with plastic work was expressed as $\omega = s_b/(0.05\sigma_{pre}\varepsilon_{pre})$ in Das et al. (2014) with an empirical constant s_b, the flow stress σ_{pre} at the end of the pre-strain, and the corresponding plastic strain ε_{pre}. But, in the present model, $\sigma_{pre}\varepsilon_{pre}$ is

substituted by plastic dissipation energy E_p which can be directly obtained in numerical FE simulations. Referring to Hartley (1966), g_b the concentration of interstitial atoms on dislocations can be given as

$$g_b = 1 - \exp\left[-3n_c b\left(\frac{\pi}{2}\right)^{1/3}\left(\frac{\mathbb{A}D_b t_b}{k_B T_b}\right)^{2/3}\right], \tag{3.27}$$

with

$$D_b = D_0 \exp\left(-\frac{Q_d}{R_{gas}T_b}\right), \tag{3.28}$$

where n_c, $\mathbb{A}$, and t_b are the volumetric concentration of interstitial atoms in the matrix of material, an interaction parameter, and BH time, respectively. In D_b, the diffusivity of the interstitial atoms, D_0, Q_d, and R_{gas} stand for the diffusion coefficient, the activation energy of diffusion, and the universal gas constant, respectively.

In Eq.(3.26), G_{Fe} is the shear modulus of the matrix of material, X_p is a spatial diameter of the precipitate particles, b is the Burgers vector, and V_f is the volume fraction of precipitation particles expressed as

$$V_f = \left(\frac{4\pi}{3}\right)\alpha_p^3 (D_b t_b)^{3/2}, \tag{3.29}$$

with a growth coefficient α_p, originally proposed by Zener (1949), given as

$$\alpha_p = \sqrt{2\frac{n_c - n_1}{n_0 - n_1}}, \tag{3.30}$$

where n_c, n_0, and n_1 denote the available free carbon concentration in the matrix, the carbon concentration in the precipitate, and the equilibrium carbon concentration between the interface and the precipitate, respectively. In the present model, for avoiding too small value of V_f, Eq.(3.29) can be slightly modified as

$$V_f = C_{prec}\left(\frac{4\pi}{3}\right)\alpha_p^3 (D_b t_b)^{3/2}, \tag{3.31}$$

where C_{prec} is a material constant with the order of 10^7. In Eq.(3.30), n_c can be calculated at the corresponding annealing temperature using Thermo-Calc with the

TCFE-9 database. n_0 can be obtained from the stoichiometry of ε-carbide ($Fe_{2.4}C$). In Leslie (1991), n_1 can be approximately estimated by the following equation

$$\log\left(n_1\right)_{ppm} = 4.06 - \frac{1335}{T_b}. \tag{3.32}$$

This equation was originally suggested by Chipman (1972).

3.1.3 Integration of BH model into YPP model

There can be various methods to couple this BH model with the YPP model. The present study does not directly use σ_{Cott} calculated from Eq.(3.25), rather adopts the relationship derived in Hartley (1966), which is expressed as

$$\left(1-g_b\right)^{(1+\omega)}\left(1+\omega g_b\right) = \exp\left(\frac{V_{act}\sigma_{Cott}}{k_B T_b}\right) = \frac{L_{dis,BH}}{L_{dis}}, \tag{3.33}$$

where $L_{dis,BH}$ is the length of the mobile dislocation line after BH and L_{dis} is that before BH. Then, by assuming

$$\frac{L_{dis,BH}}{L_{dis}} = \frac{\rho_{m,BH}}{\rho_m}, \tag{3.34}$$

where $\rho_{m,BH}$ is the mobile dislocation density after BH and ρ_m is that before BH, Eq.(3.33) can be rewritten as

$$\rho_r = \frac{\rho_{m,BH}}{\rho_m} = \left(1-g_b\right)^{(1+\omega)}\left(1+\omega g_b\right), \tag{3.35}$$

where ρ_r denotes the mobile dislocation density ratio. However, the mobile dislocation density ρ_m defined in Eq.(3.5) is only a function of $\bar{\varepsilon}$. So, a simple and effective method to associate Eq.(3.35) with Eq.(3.5) is to adopt an offset value x_b in Eq.(3.6) and Eq.(3.7) as

$$\rho_{m,BH} = \left[\rho_0 + Z(\bar{\varepsilon}-x_b)^{\chi}\right]\left\{f_{m0} + \left(f_{ma}-f_{m0}\right)\left[1-\exp\left(-\lambda(\bar{\varepsilon}-x_b)\right)\right]\right\}. \tag{3.36}$$

Therefore, after the dislocation density ratio is calculated from Eq.(3.35), x_b can be easily obtained by applying the Newton method to Eq.(3.36). A detailed procedure for obtaining x_b will be described in the next section.

The back stress $\boldsymbol{\alpha}$ also should be taken into account for the BH behavior in the LB mode. This is because the BH behavior after the pre-strain also is associated with the Bauschinger effect. Thus, the effective stress of the LB mode $\bar{\sigma}_l$ in Eq.(3.8) can be redefined as

$$\bar{\sigma}_l = \sqrt{\frac{3}{2}\left(\mathbf{s} - C_b\boldsymbol{\alpha}_b\right) : \left(\mathbf{s} - C_b\boldsymbol{\alpha}_b\right),}, \tag{3.37}$$

where $\boldsymbol{\alpha}_b$ and C_b denote the last back stress before BH and its coefficient. This stress does not change during the BH step. The flow vector of the LB mode in Eq.(3.11) is also changed as

$$\mathbf{n}_l = \frac{3}{2}\frac{\mathbf{s} - C_b\boldsymbol{\alpha}_b}{\bar{\sigma}_l}. \tag{3.38}$$

Meanwhile, σ_{prec} in Eq.(3.26) can be directly coupled with Eq.(3.3) and Eq.(3.12) as

$$\dot{\bar{\varepsilon}}_l = \frac{b\rho_m}{M}\left(\frac{\langle\bar{\sigma}_l - Y_l - \sigma_{prec}\rangle}{D_l}\right)^{n_e}, \tag{3.39}$$

$$\dot{\bar{\varepsilon}}_w = \frac{b\rho_m}{M}\left(\frac{\langle\bar{\sigma}_w - Y_w - \sigma_{prec}\rangle}{D_w}\right)^{n_e}. \tag{3.40}$$

3.2 Computational Implementation

All quantities in the discretized constitutive equations are regarded as those at the current increment $n+1$, unless specified. For instance, $\bar{\varepsilon}$ is the effective plastic strain of the current increment $n+1$ and $\bar{\varepsilon}_n$ is that of the previous increment n. The discretized constitutive equations are implemented into the Abaqus UMAT subroutine which includes BH calculations, trial state assessment, stress integration, state variable update, and consistent tangent stiffness calculation.

3.2.1 BH calculation

The calculation of the BH equations is firstly conducted before the trial stresses are assessed. The first assumption for this step is that the calculation is only performed when T_b exceeds a certain temperature, 30 °C in this study. The second assumption

is a separate calculation of BH equations from the stress integration. This means that the stress integration cannot proceed once the BH equations are calculated in the same increment. These assumptions might be quite reasonable in terms of actual automotive forming applications. For example, in the actual applications, bake hardenable steels normally take several months to be aged at room temperature as stated in Baker et al. (2002), and paint baking operations are generally separated from forming operations.

The objective of this calculation step is to obtain the offset value x_b for the Cottrell effect and the precipitation hardening σ_{prec}. Prior to determine x_b, it is necessary to calculate g_b in Eq.(3.35) by using Eq.(3.27) with BH temperature T_b and BH time t_b. When the BH temperature is constant, g_b can be directly calculated. However, it may take several minutes to increase and decrease the temperature of target objects in typical paint baking operations. Hence, a certain calculation procedure for the duration of temperature increase and decrease should be specified. In the present implementation, g_b is calculated as

$$g_b = g_{bn} + \Delta g_b. \tag{3.41}$$

When the BH temperature increase or decrease during the current increment, by differentiating Eq.(3.27), Δg_b can be given as

$$\begin{aligned} \Delta g_b = 2n_c b \left(\frac{\pi}{2t_b}\right)^{1/3} \left(\frac{\mathbb{A}D_b}{k_B T_b}\right)^{2/3} \\ \cdot \left\{ \exp\left[-3n_c b \left(\frac{\pi}{2}\right)^{1/3} \left(\frac{\mathbb{A}D_b t_b}{k_B T_b}\right)^{2/3} \right] \right\} \Delta t_b, \end{aligned} \tag{3.42}$$

evaluated at t_b which is the value of time (step time in Abaqus) at the beginning of the current increment, and Δt_b is time increment. When the BH temperature is constant during the current increment, Δg_b can be directly calculated from Eq.(3.27) replacing t_b with the total time of constant temperature. Note that if Eq.(3.42) is used when the BH temperature is constant, a much smaller value of g_b can be obtained than using Eq.(3.27). Thus, this customized procedure might be appropriate.

Meanwhile, in Eq.(3.35), ω represents $s_b/(0.05E_p)$ as previously explained. In single element FE simulations, E_p is always larger than zero when the BH calculation

proceeds after the pre-strain. However, E_p can be zero in the simulations with multiple elements, for instance, near the grip area of the tensile specimen. Therefore, ω should be alternatively expressed as $s_b/[0.05(E_p+1)]$ in order to avoid the infinity value of ω when there is no plastic deformation in some elements.

Now, the determination of the offset value x_b is addressed. Substituting Eq.(3.36) into Eq.(3.35) and rearranging it gives

$$\psi_\rho(x_b) = \rho_{m,BH}(x_b) - \rho_{mn}\rho_r = 0, \tag{3.43}$$

where ρ_{mn} stands for ρ_m of the previous increment. Then, x_b can be obtained by solving this equation with the Newton method. Linearization of Eq.(3.43) can give the (k)th iterative correction as

$$x_b{}^{(k)} := x_b{}^{(k-1)} - \frac{\psi_\rho\left(x_b{}^{(k-1)}\right)}{\left.\dfrac{\partial\psi_\rho}{\partial x_b}\right|_{x_b=x_b{}^{(k-1)}}}, \tag{3.44}$$

where

$$\frac{\partial\psi_\rho}{\partial x_b} = \frac{\partial f_m}{\partial x_b}\rho_t + f_m\frac{\partial\rho_t}{\partial x_b}, \tag{3.45}$$

with

$$\frac{\partial f_m}{\partial x_b} = \lambda\left(f_m - f_{ma}\right), \tag{3.46}$$

$$\frac{\partial\rho_t}{\partial x_b} = -\chi Z\left(\bar{\varepsilon} - x_b\right)^{\chi-1}. \tag{3.47}$$

Similarly as g_b, the precipitation hardening value σ_{prec} can be integrated as

$$\sigma_{prec} = \sigma_{prec_n} + \Delta\sigma_{prec}, \tag{3.48}$$

where σ_{prec_n} stands for σ_{prec} of the previous increment, and

$$\begin{aligned}\Delta\sigma_{prec} &= 0.538\frac{G_{Fe}b}{2X_p{V_f}^{1/2}}\ln\left(\frac{X_p}{2b}\right)\frac{3}{2}C_{prec}\left(\frac{4\pi}{3}\right)\alpha_p^3{D_b}^{3/2}{t_b}^{1/2}\Delta t_b \\ &= 0.538\frac{3G_{Fe}b{V_f}^{1/2}}{4X_p t_b}\ln\left(\frac{X_p}{2b}\right)\Delta t_b.\end{aligned} \tag{3.49}$$

Note that Eq.(3.49) is only applicable when the BH temperature is changed, and if it is constant, Eq.(3.26) is used after replacing t_b with the total time of constant temperature. With the obtained values of x_b and σ_{prec}, the next stress integration procedure begins.

3.2.2 Trial state assessment

When the total strain increment $\Delta\boldsymbol{\varepsilon}$ is given in the subroutine, it is decomposed as

$$\Delta\boldsymbol{\varepsilon} = \Delta\boldsymbol{\varepsilon}^e + \Delta\boldsymbol{\varepsilon}^p, \tag{3.50}$$

where $\Delta\boldsymbol{\varepsilon}^e$ and $\Delta\boldsymbol{\varepsilon}^p$ are the elastic and plastic part of $\Delta\boldsymbol{\varepsilon}$, respectively. This equation is obtained from Eq.(3.1) based on the incremental deformation theory of Chung and Richmond (1993). At the beginning of the subroutine, we assume the current state is purely elastic, i.e. $\Delta\boldsymbol{\varepsilon} = \Delta\boldsymbol{\varepsilon}^e$, and the trial stress and its effective values are obtained as

$$\boldsymbol{\sigma}^T = \boldsymbol{\sigma}_n + \mathbf{D} : \Delta\boldsymbol{\varepsilon}^e, \tag{3.51}$$

$$\bar{\sigma}_l^T = \sqrt{\frac{3}{2}(\mathbf{s}^T - C_b\boldsymbol{\alpha}_b) : (\mathbf{s}^T - C_b\boldsymbol{\alpha}_b)}, \tag{3.52}$$

$$\bar{\sigma}_w^T = \sqrt{\frac{3}{2}(\mathbf{s}^T - \boldsymbol{\alpha}_n) : (\mathbf{s}^T - \boldsymbol{\alpha}_n)}, \tag{3.53}$$

where $'T'$ denotes the trial state. Then, we can assess whether the current state is purely elastic or viscoplastic using the following conditions:

$$\bar{\sigma}_l^T < (Y_l + \sigma_{prec}) \quad \text{and} \quad \bar{\sigma}_w^T < (Y_{wn} + \sigma_{prec}), \tag{3.54}$$

$$\bar{\sigma}_l^T < (Y_l + \sigma_{prec}) \quad \text{and} \quad \bar{\sigma}_w^T \geq (Y_{wn} + \sigma_{prec}), \tag{3.55}$$

$$\bar{\sigma}_l^T \geq (Y_l + \sigma_{prec}) \quad \text{and} \quad \bar{\sigma}_w^T < (Y_{wn} + \sigma_{prec}), \tag{3.56}$$

$$\bar{\sigma}_l^T > (Y_l + \sigma_{prec}) \quad \text{and} \quad \bar{\sigma}_w^T > (Y_{wn} + \sigma_{prec}), \tag{3.57}$$

with Eq.(3.39) and Eq.(3.40). The discrete form of Eq.(3.39) and Eq.(3.40) becomes

$$\frac{\Delta\bar{\varepsilon}_l}{\Delta t} = \frac{b f_m \rho_t}{M}\left(\frac{\langle\bar{\sigma}_l - Y_l - \sigma_{prec}\rangle}{D_l}\right)^{n_e}, \tag{3.58}$$

$$\frac{\Delta\bar{\varepsilon}_w}{\Delta t} = \frac{b f_m \rho_t}{M}\left(\frac{\langle \bar{\sigma}_w - Y_w - \sigma_{prec}\rangle}{D_w}\right)^{n_e}, \tag{3.59}$$

where

$$f_m = f_{m0} + (f_{ma} - f_{m0})\left\{1 - \exp\left[-\lambda\left(\bar{\varepsilon}_n + \Delta\bar{\varepsilon} - x_b\right)\right]\right\}, \tag{3.60}$$

$$\rho_t = \rho_0 + Z\left(\bar{\varepsilon}_n + \Delta\bar{\varepsilon} - x_b\right)^{\chi}, \tag{3.61}$$

and

$$\begin{aligned} Y_w &= Y_{w0} + (Y_{wa} - Y_{w0})\left\{1 - \exp\left[-\zeta\left(\bar{\varepsilon}_n + \Delta\bar{\varepsilon}\right)\right]\right\} \quad \text{or} \\ Y_w &= \frac{Y_{wa}}{2}\left\{1 + \tanh\left[\zeta\left(\bar{\varepsilon}_n + \Delta\bar{\varepsilon} - Y_{w0}\right)\right]\right\}, \end{aligned} \tag{3.62}$$

with $\Delta\bar{\varepsilon} = \Delta\bar{\varepsilon}_l$ and $\Delta\bar{\varepsilon} = \Delta\bar{\varepsilon}_w$ for the LB region and the WH region, respectively. It is obvious that the condition Eq.(3.54) is elastic and the condition Eq.(3.57) is viscoplastic by the angle bracket. For other conditions, we need the selection criterion of the Yoshida-2008 model for the region as

$$\begin{aligned} &\text{LB region if} \quad \Delta\bar{\varepsilon}_l < \Delta\bar{\varepsilon}_w \quad \text{or} \\ &\text{WH region if} \quad \Delta\bar{\varepsilon}_l \geq \Delta\bar{\varepsilon}_w \end{aligned} \tag{3.63}$$

for a given stress, assuming $D_l > D_w$. Applying the condition Eq.(3.55) to Eqs.(3.58)-(3.59) yields $\Delta\bar{\varepsilon}_l = 0$ and $\Delta\bar{\varepsilon}_w \geq 0$. Then, by the criterion Eq.(3.63), the current state is still elastic. Analogously, the condition Eq.(3.56) is also an elastic state. If the current state turns out to be elastic, the subroutine goes on to the next increment after updating the stress as $\boldsymbol{\sigma} = \boldsymbol{\sigma}^T$ and returning the elasticity tensor $\mathbf{D}$ as the consistent tangent stiffness. When the current state becomes viscoplastic, the subroutine starts the stress integration procedure.

3.2.3 Stress integration

The primary computation of the stress integration is to find $\Delta\bar{\varepsilon}_l$ for the LB region and $\Delta\bar{\varepsilon}_w$, θ, and $\boldsymbol{\beta}$ for the WH region.

LB region

With the well-known relation

$$\bar{\sigma}_l = \bar{\sigma}_l^T - 3G\Delta\bar{\varepsilon}_l \tag{3.64}$$

in the radial return mapping scheme for von Mises plasticity, rewriting Eq.(3.58) for the LB region gives

$$\psi_l\left(\Delta\bar{\varepsilon}_l\right) = \frac{\Delta\bar{\varepsilon}_l}{\Delta t} - \frac{bf_m\rho_t}{M}\left(\frac{\bar{\sigma}_l^T - 3G\Delta\bar{\varepsilon}_l - Y_l - \sigma_{prec}}{D_l}\right)^{n_e} = 0, \tag{3.65}$$

where G denotes the shear modulus. The traditional one-point Newton method to solve $\psi_l\left(\Delta\bar{\varepsilon}_l\right) = 0$ brings the (k)th iterative correction as

$$\Delta\bar{\varepsilon}_l^{(k)} := \Delta\bar{\varepsilon}_l^{(k-1)} - \frac{\psi_l\left(\Delta\bar{\varepsilon}_l^{(k-1)}\right)}{\left.\dfrac{\partial\psi_l}{\partial\Delta\bar{\varepsilon}_l}\right|_{\Delta\bar{\varepsilon}_l=\Delta\bar{\varepsilon}_l^{(k-1)}}}, \tag{3.66}$$

where

$$\begin{aligned}\frac{\partial\psi_l}{\partial\Delta\bar{\varepsilon}_l} = \frac{1}{\Delta t} - \frac{b}{M}\left(\frac{\partial f_m}{\partial\Delta\bar{\varepsilon}_l}\rho_t + f_m\frac{\partial\rho_t}{\partial\Delta\bar{\varepsilon}_l}\right)\left(\frac{\bar{\sigma}_l^T - 3G\Delta\bar{\varepsilon}_l - Y_l - \sigma_{prec}}{D_l}\right)^{n_e} \\ -\frac{bf_m\rho_t}{M}\left(\frac{-3Gn_e}{D_l}\right)\left(\frac{\bar{\sigma}_l^T - 3G\Delta\bar{\varepsilon}_l - Y_l - \sigma_{prec}}{D_l}\right)^{n_e-1},\end{aligned} \tag{3.67}$$

with

$$\frac{\partial f_m}{\partial\Delta\bar{\varepsilon}_l} = \lambda\left(f_{ma} - f_m\right) \quad \text{and} \quad \frac{\partial\rho_t}{\partial\Delta\bar{\varepsilon}_l} = \chi Z\left(\bar{\varepsilon}_n + \Delta\bar{\varepsilon}_l - x_b\right)^{\chi-1}. \tag{3.68}$$

With this method, however, the solution of Eq.(3.65) may not be obtained when $\Delta\bar{\varepsilon}_l^{(0)} = 0$ and $\bar{\varepsilon}_n$ is close to zero because Eq.(3.65) has a minimum in the vicinity of $\Delta\bar{\varepsilon}_l = 0$ as shown Fig.3.1. For this reason, a robust iterative method such as the bisection method or the two-point Newton method is required in the stress integration. If we use the bisection method, the convergence is guaranteed as the initial lower bound $\mathbb{L}_l^{(0)}$ and the initial upper bound $\mathbb{U}_l^{(0)}$ determined from Eq.(3.65) as

$$\mathbb{L}_l^{(0)} = 0 \quad \text{and} \quad \mathbb{U}_l^{(0)} = \frac{\bar{\sigma}_l^T - Y_l - \sigma_{prec}}{3G}, \tag{3.69}$$

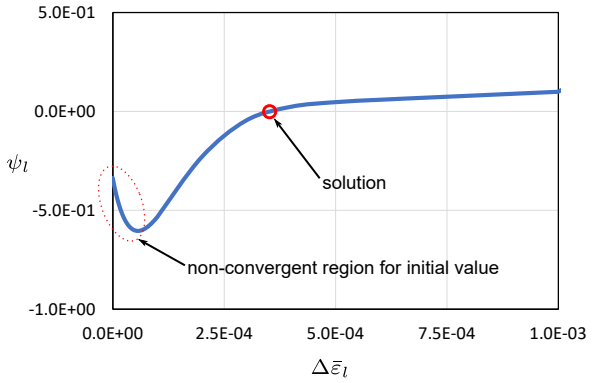

Figure 3.1. Graph of Eq.(3.65) when $\Delta t = 0.001$, $\bar{\sigma}_l^T = 460$, $\bar{\varepsilon}_n = 0.00001$ and the material parameters in Table 3.1.

Table 3.1. Material parameters for Fig.3.1.

Common parameters											LB mode	
E [GPa]	ν	b [mm]	M	f_{m0}	f_{ma}	λ	ρ_0	Z	χ	n_e	D_l	Y_l
199.5	0.3	2.5e-7	2.76	1.0e-5	0.1	10	1.0e4	3.0e9	1.5	20	130.0	150.0

satisfy always $\psi_l(\mathbb{L}_l^{(0)}) < 0$ and $\psi_l(\mathbb{U}_l^{(0)}) > 0$. The iterative update for this method can be made as

$$\begin{aligned} \mathbb{L}_l^{(k)} &= \frac{\mathbb{L}_l^{(k-1)} + \mathbb{U}_l^{(k-1)}}{2} \quad \text{if} \quad \psi_l(\mathbb{L}_l^{(k)}) \cdot \psi_l(\mathbb{L}_l^{(k-1)}) > 0 \\ \mathbb{U}_l^{(k)} &= \frac{\mathbb{L}_l^{(k-1)} + \mathbb{U}_l^{(k-1)}}{2} \quad \text{otherwise,} \end{aligned} \tag{3.70}$$

until $\psi_l(\mathbb{L}_l^{(k)})$, $\psi_l(\mathbb{U}_l^{(k)})$ or $(\mathbb{U}_l^{(k)} - \mathbb{L}_l^{(k)})$ are less than the specified tolerance of the integration procedure.

The two-point Newton method Tiruneh et al. (2013) defines a new variable as

$$\mathbb{M} = \frac{\psi_l - \psi_l^{(k-1)}}{\Delta\bar{\varepsilon}_l - \Delta\bar{\varepsilon}_l^{(k-1)}}, \tag{3.71}$$

where $\Delta\bar{\varepsilon}_l^{(k-1)}$ and $\psi_l^{(k-1)}$ denote the $(k-1)$th guess and the corresponding $\psi_l^{(k-1)}$ at $\Delta\bar{\varepsilon}_l^{(k-1)}$, respectively. Then, this variable can be used as an independent variable of the

function ψ_l. By applying the Newton method, a better approximation $\mathbb{M}^{(k+1)}$ for the $(k+1)$th iteration becomes

$$\mathbb{M}^{(k+1)} = \mathbb{M}^{(k)} - \frac{\psi_l^{(k)}}{\left.\dfrac{d\psi_l}{d\mathbb{M}}\right|_{\Delta\bar{\varepsilon}_l = \Delta\bar{\varepsilon}_l^{(k)}}}, \tag{3.72}$$

where

$$\mathbb{M}^{(k+1)} = \frac{\psi_l^{(k+1)} - \psi_l^{(k-1)}}{\Delta\bar{\varepsilon}_l^{(k+1)} - \Delta\bar{\varepsilon}_l^{(k-1)}} \quad \text{and} \quad \mathbb{M}^{(k)} = \frac{\psi_l^{(k)} - \psi_l^{(k-1)}}{\Delta\bar{\varepsilon}_l^{(k)} - \Delta\bar{\varepsilon}_l^{(k-1)}}. \tag{3.73}$$

If $\mathbb{M}^{(k+1)}$ satisfies $\psi_l = 0$, $\psi_l^{(k+1)} = 0$. Then, substituting Eq.(3.73) into Eq.(3.72) gives

$$\frac{-\psi_l^{(k-1)}}{\Delta\bar{\varepsilon}_l^{(k+1)} - \Delta\bar{\varepsilon}_l^{(k-1)}} = \frac{\psi_l^{(k)} - \psi_l^{(k-1)}}{\Delta\bar{\varepsilon}_l^{(k)} - \Delta\bar{\varepsilon}_l^{(k-1)}} - \frac{\psi_l^{(k)}}{\left.\dfrac{d\psi_l}{d\mathbb{M}}\right|_{\Delta\bar{\varepsilon}_l = \Delta\bar{\varepsilon}_l^{(k)}}}. \tag{3.74}$$

The derivative ψ_l with respect to $\mathbb{M}$ can be expressed as

$$\frac{d\psi_l}{d\mathbb{M}} = \frac{\dfrac{d\psi_l}{d\Delta\bar{\varepsilon}_l}}{\dfrac{d\mathbb{M}}{d\Delta\bar{\varepsilon}_l}} = \frac{\dfrac{d\psi_l}{d\Delta\bar{\varepsilon}_l}\left(\Delta\bar{\varepsilon}_l - \Delta\bar{\varepsilon}_l^{(0)}\right)^2}{\left(\Delta\bar{\varepsilon}_l - \Delta\bar{\varepsilon}_l^{(0)}\right)\dfrac{d\psi_l}{d\Delta\bar{\varepsilon}_l} - \left(\psi_l - \psi_l^{(0)}\right)}. \tag{3.75}$$

Inserting Eq.(3.75) into Eq.(3.74) and deriving for $\Delta\bar{\varepsilon}_l^{(k+1)}$ yield

$$\Delta\bar{\varepsilon}_l^{(k+1)} = \Delta\bar{\varepsilon}_l^{(k-1)} + \frac{\Delta\bar{\varepsilon}_l^{(k)} - \Delta\bar{\varepsilon}_l^{(k-1)}}{1 - \dfrac{\psi_l^{(k)}}{\psi_l^{(k-1)}}\dfrac{\psi_l^{(k)} - \psi_l^{(k-1)}}{\Delta\bar{\varepsilon}_l^{(k)} - \Delta\bar{\varepsilon}_l^{(k-1)}}\dfrac{1}{\left.\dfrac{d\psi_l}{d\Delta\bar{\varepsilon}_l}\right|_{\Delta\bar{\varepsilon}_l = \Delta\bar{\varepsilon}_l^{(k)}}}}. \tag{3.76}$$

The initial two points $\Delta\bar{\varepsilon}_l^{(0)}$ and $\Delta\bar{\varepsilon}_l^{(1)}$ can be chosen as $\mathbb{L}^{(0)}$ and $\mathbb{U}^{(0)}/2$, respectively, for this two-point Newton method.

WH region

For the WH mode, Eq.(3.59), Eqs.(3.60)-(3.62) and the following incremental forms

$$\boldsymbol{\theta} - \boldsymbol{\theta}_n = C\Delta\bar{\varepsilon}_w \left(\frac{2}{3} a \mathbf{n}_w - \sqrt{\frac{a}{\bar{\theta}}} \boldsymbol{\theta} \right), \tag{3.77}$$

$$\boldsymbol{\beta} - \boldsymbol{\beta}_n = m\Delta\bar{\varepsilon}_w \left(\frac{2}{3} b_1 \mathbf{n}_w - \boldsymbol{\beta} \right), \tag{3.78}$$

are solved to find $\Delta\bar{\varepsilon}_w$, $\boldsymbol{\theta}$ and $\boldsymbol{\beta}$. After $\boldsymbol{\theta}$ and $\boldsymbol{\beta}$ are obtained, the back stress $\boldsymbol{\alpha}$ can be obtained by Eq.(3.15). Rearranged from Eq.(3.59) and Eqs.(3.16)-(3.17), the discrete constitutive equations for the WH region can be defined as

$$\psi_w \left(\Delta\bar{\varepsilon}_w, \boldsymbol{\theta}, \boldsymbol{\beta} \right) = \frac{\Delta\bar{\varepsilon}_w}{\Delta t} - \frac{b f_m \rho_t}{M} \left(\frac{\bar{\sigma}_w^{\mathbb{T}} - 3G\Delta\bar{\varepsilon}_w - Y_w - \sigma_{prec}}{D_w} \right)^{n_e} = 0, \tag{3.79}$$

$$\boldsymbol{\psi}_\theta \left(\Delta\bar{\varepsilon}_w, \boldsymbol{\theta}, \boldsymbol{\beta} \right) = \boldsymbol{\theta} - \boldsymbol{\theta}_n - C\Delta\bar{\varepsilon}_w \left(\frac{2}{3} a \mathbf{n}_w - \sqrt{\frac{a}{\bar{\theta}}} \boldsymbol{\theta} \right) = \mathbf{0}, \tag{3.80}$$

$$\boldsymbol{\psi}_\beta \left(\Delta\bar{\varepsilon}_w, \boldsymbol{\theta}, \boldsymbol{\beta} \right) = \boldsymbol{\beta} - \boldsymbol{\beta}_n - m\Delta\bar{\varepsilon}_w \left(\frac{2}{3} b_1 \mathbf{n}_w - \boldsymbol{\beta} \right) = \mathbf{0}, \tag{3.81}$$

where

$$\bar{\sigma}_w^{\mathbb{T}} = \sqrt{\frac{3}{2} \left(\mathbf{s}^T - \boldsymbol{\alpha} \right) : \left(\mathbf{s}^T - \boldsymbol{\alpha} \right)}, \tag{3.82}$$

$$\mathbf{n}_w = \frac{3}{2} \frac{\mathbf{s} - \boldsymbol{\alpha}}{\bar{\sigma}_w} = \frac{3}{2} \frac{\mathbf{s}^T - \boldsymbol{\alpha}}{\bar{\sigma}_w^{\mathbb{T}}}. \tag{3.83}$$

Note that, as in the LB region, the well-known relation

$$\bar{\sigma}_w = \bar{\sigma}_w^{\mathbb{T}} - 3G\Delta\bar{\varepsilon}_w \tag{3.84}$$

is used in defining Eq.(3.79). $\boldsymbol{\alpha}$ in Eq.(3.82) is the back stress calculated from Eq.(3.15) at the current increment. Then, the conventional one-point Newton method for multi-variate case uses the linear equations

$$\frac{\partial \psi_w}{\partial \Delta\bar{\varepsilon}_w} \mathrm{d}\Delta\bar{\varepsilon}_w + \frac{\partial \psi_w}{\partial \boldsymbol{\theta}} : \mathrm{d}\boldsymbol{\theta} + \frac{\partial \psi_w}{\partial \boldsymbol{\beta}} : \mathrm{d}\boldsymbol{\beta} = -\psi_w, \tag{3.85}$$

$$\frac{\partial \boldsymbol{\psi}_\theta}{\partial \Delta\bar{\varepsilon}_w} \mathrm{d}\Delta\bar{\varepsilon}_w + \frac{\partial \boldsymbol{\psi}_\theta}{\partial \boldsymbol{\theta}} : \mathrm{d}\boldsymbol{\theta} + \frac{\partial \boldsymbol{\psi}_\theta}{\partial \boldsymbol{\beta}} : \mathrm{d}\boldsymbol{\beta} = -\boldsymbol{\psi}_\theta, \tag{3.86}$$

$$\frac{\partial \boldsymbol{\psi}_\beta}{\partial \Delta\bar{\varepsilon}_w}\mathrm{d}\Delta\bar{\varepsilon}_w + \frac{\partial \boldsymbol{\psi}_\beta}{\partial \boldsymbol{\theta}} : \mathrm{d}\boldsymbol{\theta} + \frac{\partial \boldsymbol{\psi}_\beta}{\partial \boldsymbol{\beta}} : \mathrm{d}\boldsymbol{\beta} = -\boldsymbol{\psi}_\beta, \tag{3.87}$$

where

$$\frac{\partial \psi_w}{\partial \Delta\bar{\varepsilon}_w} = \frac{1}{\Delta t} - \frac{b}{M}\left(\frac{\partial f_m}{\partial \Delta\bar{\varepsilon}_w}\rho_t + f_m\frac{\partial \rho_t}{\partial \Delta\bar{\varepsilon}_w}\right)\left(\frac{\bar{\sigma}_w^{\mathbb{T}} - 3G\Delta\bar{\varepsilon}_w - Y_w - \sigma_{prec}}{D_w}\right)^{n_e} + \frac{bf_m\rho_t}{M}\frac{n_e}{D_w}\left(3G + \frac{\partial Y_w}{\partial \Delta\bar{\varepsilon}}\right)\left(\frac{\bar{\sigma}_w^{\mathbb{T}} - 3G\Delta\bar{\varepsilon}_w - Y_w - \sigma_{prec}}{D_w}\right)^{n_e-1}, \tag{3.88}$$

$$\frac{\partial \psi_w}{\partial \boldsymbol{\theta}} = \frac{\partial \psi_w}{\partial \boldsymbol{\beta}} = \frac{bf_m\rho_t}{M}\frac{n_e}{D_w}\left(\frac{\bar{\sigma}_w^{\mathbb{T}} - 3G\Delta\bar{\varepsilon}_w - Y_w - \sigma_{prec}}{D_w}\right)^{n_e-1}\mathbf{n}_w, \tag{3.89}$$

$$\frac{\partial \boldsymbol{\psi}_\theta}{\partial \Delta\bar{\varepsilon}_w} = C\left[\left(\sqrt{\frac{a}{\bar{\theta}}} + \frac{\partial a}{\partial \Delta\bar{\varepsilon}_w}\frac{\Delta\bar{\varepsilon}_w}{2\sqrt{a\bar{\theta}}}\right)\boldsymbol{\theta} - \frac{2}{3}\left(a + \Delta\bar{\varepsilon}_w\frac{\partial a}{\partial \Delta\bar{\varepsilon}_w}\right)\mathbf{n}_w\right], \tag{3.90}$$

$$\frac{\partial \boldsymbol{\psi}_\theta}{\partial \boldsymbol{\theta}} = \mathbf{I}_s + C\Delta\bar{\varepsilon}_w\left[\frac{2}{3}a\frac{\partial \mathbf{n}_w}{\partial \mathbf{s}} + \sqrt{\frac{a}{\bar{\theta}}}\left(\mathbf{I}_s - \frac{3}{4}\frac{\boldsymbol{\theta}\otimes\boldsymbol{\theta}}{\bar{\theta}^2}\right)\right], \tag{3.91}$$

$$\frac{\partial \boldsymbol{\psi}_\theta}{\partial \boldsymbol{\beta}} = C\Delta\bar{\varepsilon}_w\frac{2}{3}a\frac{\partial \mathbf{n}_w}{\partial \mathbf{s}}, \tag{3.92}$$

$$\frac{\partial \boldsymbol{\psi}_\beta}{\partial \Delta\bar{\varepsilon}_w} = m\left(\boldsymbol{\beta} - \frac{2}{3}b_1\mathbf{n}_w\right), \tag{3.93}$$

$$\frac{\partial \boldsymbol{\psi}_\beta}{\partial \boldsymbol{\theta}} = m\Delta\bar{\varepsilon}_w\frac{2}{3}b_1\frac{\partial \mathbf{n}_w}{\partial \mathbf{s}}, \tag{3.94}$$

$$\frac{\partial \boldsymbol{\psi}_\beta}{\partial \boldsymbol{\beta}} = \mathbf{I}_s + m\Delta\bar{\varepsilon}_w\left(\frac{2}{3}b_1\frac{\partial \mathbf{n}_w}{\partial \mathbf{s}} + \mathbf{I}_s\right), \tag{3.95}$$

with

$$\frac{\partial f_m}{\partial \Delta\bar{\varepsilon}_w} = \lambda\left(f_{ma} - f_m\right), \tag{3.96}$$

$$\frac{\partial \rho_t}{\partial \Delta\bar{\varepsilon}_w} = \chi Z\left(\bar{\varepsilon}_n + \Delta\bar{\varepsilon}_w - x_b\right)^{\chi-1}, \tag{3.97}$$

$$\frac{\partial a}{\partial \Delta\bar{\varepsilon}_w} = m\left(R_{sat} - R_b\right), \tag{3.98}$$

and

$$\frac{\partial Y_w}{\partial \Delta\bar{\varepsilon}_w} = \zeta\left(Y_{wa} - Y_w\right) \quad \text{or} \quad \frac{\partial Y_w}{\partial \Delta\bar{\varepsilon}_w} = \frac{\zeta Y_{wa}}{2\cosh^2\zeta\left(\bar{\varepsilon}_n + \Delta\bar{\varepsilon}_w - Y_{w0}\right)}, \tag{3.99}$$

for the correction to the current $\boldsymbol{\theta}$, $\boldsymbol{\beta}$ and $\Delta\bar{\varepsilon}_w$ as

$$\Delta\bar{\varepsilon}_w^{(k)} := \Delta\bar{\varepsilon}_w^{(k-1)} + \mathrm{d}\Delta\bar{\varepsilon}_w, \tag{3.100}$$

$$\boldsymbol{\theta}^{(k)} := \boldsymbol{\theta}^{(k-1)} + \mathrm{d}\boldsymbol{\theta}, \tag{3.101}$$

$$\boldsymbol{\beta}^{(k)} := \boldsymbol{\beta}^{(k-1)} + \mathrm{d}\boldsymbol{\beta}. \tag{3.102}$$

Here, $\mathbf{I}_s$ is the fourth-order symmetric projection tensor. The right-hand side terms of Eqs.(3.85)-(3.99) are evaluated at $(\Delta\bar{\varepsilon}_w, \boldsymbol{\theta}, \boldsymbol{\beta}) = (\Delta\bar{\varepsilon}_w^{(k-1)}, \boldsymbol{\theta}^{(k-1)}, \boldsymbol{\beta}^{(k-1)})$. The initial points for this case are chosen as $(\Delta\bar{\varepsilon}_w^{(0)}, \boldsymbol{\theta}^{(0)}, \boldsymbol{\beta}^{(0)}) = (0, \boldsymbol{\theta}_n, \boldsymbol{\beta}_n)$.

Inferred from the similarity between Eq.(3.65) and Eq.(3.79), it may be necessary to use the two-point Newton method. For the multivariate two-point Newton method, Eqs.(3.79)-(3.81) may be expressed as

$$\boldsymbol{\Psi}(\boldsymbol{\gamma}) = \mathbf{0}, \tag{3.103}$$

where the vector $\boldsymbol{\Psi}$ consists of ψ_w, $\boldsymbol{\psi}_\theta$ and $\boldsymbol{\psi}_\beta$ and the vector $\boldsymbol{\gamma}$ includes $\Delta\bar{\varepsilon}_w$, $\boldsymbol{\theta}$ and $\boldsymbol{\beta}$ as

$$\boldsymbol{\Psi} = \begin{bmatrix} \psi_w \\ \boldsymbol{\psi}_\theta \\ \boldsymbol{\psi}_\beta \end{bmatrix} \quad \text{and} \quad \boldsymbol{\gamma} = \begin{bmatrix} \Delta\bar{\varepsilon}_w \\ \boldsymbol{\theta} \\ \boldsymbol{\beta} \end{bmatrix}. \tag{3.104}$$

Here, $\boldsymbol{\psi}_\theta$, $\boldsymbol{\psi}_\beta$, $\boldsymbol{\theta}$ and $\boldsymbol{\beta}$ are written in vector form for convenience in calculation. Then, the approximated function $\mathbf{R}$, proposed by Saheya et al. (2016), at $\boldsymbol{\gamma}^{(k)}$ is given as

$$\boldsymbol{\Psi}(\boldsymbol{\gamma}) \approx \mathbf{R}(\boldsymbol{\gamma}) = \boldsymbol{\Psi}(\boldsymbol{\gamma}^{(k)}) + \frac{\mathbf{J}^{(k)}(\boldsymbol{\gamma} - \boldsymbol{\gamma}^{(k)})}{1 + \mathbf{b}^{(k)} \cdot (\boldsymbol{\gamma} - \boldsymbol{\gamma}^{(k)})} = \mathbf{0}, \tag{3.105}$$

where

$$\mathbf{J}^{(k)} = \left.\frac{\partial \boldsymbol{\Psi}}{\partial \boldsymbol{\gamma}}\right|_{\boldsymbol{\gamma}=\boldsymbol{\gamma}^{(k)}} = \begin{bmatrix} \frac{\partial \psi_w}{\partial \Delta\bar{\varepsilon}_w} & \frac{\partial \psi_w}{\partial \boldsymbol{\theta}} & \frac{\partial \psi_w}{\partial \boldsymbol{\beta}} \\ \frac{\partial \boldsymbol{\psi}_\theta}{\partial \Delta\bar{\varepsilon}_w} & \frac{\partial \boldsymbol{\psi}_\theta}{\partial \boldsymbol{\theta}} & \frac{\partial \boldsymbol{\psi}_\theta}{\partial \boldsymbol{\beta}} \\ \frac{\partial \boldsymbol{\psi}_\beta}{\partial \Delta\bar{\varepsilon}_w} & \frac{\partial \boldsymbol{\psi}_\beta}{\partial \boldsymbol{\theta}} & \frac{\partial \boldsymbol{\psi}_\beta}{\partial \boldsymbol{\beta}} \end{bmatrix}_{\boldsymbol{\gamma}=\boldsymbol{\gamma}^{(k)}}, \tag{3.106}$$

and $\mathbf{b}^{(k)}$ is the unknown coefficient vector which has the same size as the vector $\boldsymbol{\gamma}$. If $\mathbf{b}^{(k)} = \mathbf{0}$, Eq.(3.105) becomes the linear equations in Eqs.(3.85)-(3.87). If $\mathbf{b}^{(k)} \neq \mathbf{0}$, the $(k+1)$th iterative correction can be obtained from Eq.(3.105) as

$$\boldsymbol{\gamma}^{(k+1)} = \boldsymbol{\gamma}^{(k)} - (\mathbf{J}^{(k)} + \boldsymbol{\Psi}^{(k)} \otimes \mathbf{b}^{(k)})^{-1}\boldsymbol{\Psi}^{(k)}, \tag{3.107}$$

where $\boldsymbol{\Psi}^{(k)} = \boldsymbol{\Psi}(\boldsymbol{\gamma}^{(k)})$. In order to determine $\mathbf{b}^{(k)}$, substituting the condition

$$\mathbf{R}(\boldsymbol{\gamma}^{(k-1)}) = \boldsymbol{\Psi}(\boldsymbol{\gamma}^{(k-1)}) \tag{3.108}$$

into Eq.(3.105) provides

$$\boldsymbol{\Psi}^{(k-1)} = \boldsymbol{\Psi}^{(k)} - \frac{\mathbf{J}^{(k)}(\boldsymbol{\gamma}^{(k)} - \boldsymbol{\gamma}^{(k-1)})}{1 - \mathbf{b}^{(k)} \cdot (\boldsymbol{\gamma}^{(k)} - \boldsymbol{\gamma}^{(k-1)})}, \tag{3.109}$$

where $\boldsymbol{\Psi}^{(k-1)} = \boldsymbol{\Psi}(\boldsymbol{\gamma}^{(k-1)})$. Rearranging of Eq.(3.109) gives

$$\begin{aligned} &\mathbf{b}^{(k)} \cdot (\boldsymbol{\gamma}^{(k)} - \boldsymbol{\gamma}^{(k-1)}) \\ &= \frac{(\boldsymbol{\Psi}^{(k)} - \boldsymbol{\Psi}^{(k-1)}) \cdot \left[(\boldsymbol{\Psi}^{(k)} - \boldsymbol{\Psi}^{(k-1)}) - \mathbf{J}^{(k)}(\boldsymbol{\gamma}^{(k)} - \boldsymbol{\gamma}^{(k-1)})\right]}{(\boldsymbol{\Psi}^{(k)} - \boldsymbol{\Psi}^{(k-1)}) \cdot (\boldsymbol{\Psi}^{(k)} - \boldsymbol{\Psi}^{(k-1)})}, \end{aligned} \tag{3.110}$$

and Saheya et al. (2016) chose $\mathbf{b}^{(k)}$ as

$$\begin{aligned} &\mathbf{b}^{(k)} = \mathbb{B}(\boldsymbol{\gamma}^{(k)} - \boldsymbol{\gamma}^{(k-1)}) \quad \text{where} \quad \mathbb{B} = \\ &\frac{(\boldsymbol{\Psi}^{(k)} - \boldsymbol{\Psi}^{(k-1)}) \cdot \left[(\boldsymbol{\Psi}^{(k)} - \boldsymbol{\Psi}^{(k-1)}) - \mathbf{J}^{(k)}(\boldsymbol{\gamma}^{(k)} - \boldsymbol{\gamma}^{(k-1)})\right]}{\|\boldsymbol{\Psi}^{(k)} - \boldsymbol{\Psi}^{(k-1)}\|^2 \|\boldsymbol{\gamma}^{(k)} - \boldsymbol{\gamma}^{(k-1)}\|^2}, \end{aligned} \tag{3.111}$$

which satisfies Eq.(3.110). The single variable case of Eq.(3.107) becomes identical with Eq.(3.76). The initial two vectors $\boldsymbol{\gamma}^{(0)}$ and $\boldsymbol{\gamma}^{(1)}$ may be selected as

$$\boldsymbol{\gamma}^{(i)} = \begin{bmatrix} \Delta\bar{\varepsilon}_w^{(i)} \\ \boldsymbol{\theta}^{(i)} \\ \boldsymbol{\beta}^{(i)} \end{bmatrix}, (i = 1, 2), \tag{3.112}$$

where

$$\boldsymbol{\beta}^{(i)} = \frac{\boldsymbol{\beta}_n + \frac{2}{3} b_1 m \Delta\bar{\varepsilon}_w^{(i)} \mathbf{n}_{wn}}{1 + m\Delta\bar{\varepsilon}_w^{(i)}} \quad \text{and} \quad \boldsymbol{\theta}^{(i)} = \frac{\boldsymbol{\theta}_n + \frac{2}{3} C a_n \Delta\bar{\varepsilon}_w^{(i)} \mathbf{n}_{wn}}{1 + C\Delta\bar{\varepsilon}_w^{(i)} \sqrt{(a_n/\bar{\theta}_n)}}, \tag{3.113}$$

with

$$\mathbf{n}_{wn} = \frac{\mathbf{s}^T - \boldsymbol{\alpha}_n}{\bar{\sigma}_w^T}, \quad a_n = B_0 + R_{bn} - Y_{wa} \quad \text{and} \quad \bar{\theta}_n = \sqrt{\frac{3}{2} \boldsymbol{\theta}_n : \boldsymbol{\theta}_n}. \tag{3.114}$$

Here, we can use

$$\Delta\bar{\varepsilon}_w^{(0)} = \mathbb{L}_w^{(0)} = 0 \quad \text{and} \quad \Delta\bar{\varepsilon}_w^{(1)} = \mathbb{U}_w^{(0)}/2 \tag{3.115}$$

after $\mathbb{U}_w^{(0)}$ is obtained by solving the following equation

$$\bar{\sigma}_w^T - 3G\Delta\bar{\varepsilon}_w - Y_w - \sigma_{prec} = 0, \tag{3.116}$$

with the one-point Newton method.

Initialization for the WH region

Although the two-point Newton method, not to mention the conventional one-point method, is adopted in the WH region, converged solutions are not easily attained when $\bar{\varepsilon}_n$ is very small and $\Delta\bar{\varepsilon}_w^{(0)} = 0$. Therefore, in the present study, we add an initialization procedure before solving Eqs.(3.79)-(3.81) to have the initial value $\Delta\bar{\varepsilon}_w^{(0)}$ closer to an actual solution. In this initialization, only Eq.(3.79) is solved using the one-point or the two-point Newton method with the initial points of Eq.(3.115) after $\bar{\sigma}_w^{\mathbb{T}}$ is replaced by $\bar{\sigma}_w^T$. If these Newton methods do not give a converged solution, the bisection method can be activated with the lower bound $\mathbb{L}_w^{(0)}$ and the upper bound $\mathbb{U}_w^{(0)}$ in Eq.(3.115). Once $\Delta\bar{\varepsilon}_w^{(0)}(\neq 0)$ is obtained, $\boldsymbol{\beta}^{(0)}$ and $\boldsymbol{\theta}^{(0)}$ for solving Eqs.(3.79)-(3.81) with the one-point Newton method are calculated from Eq.(3.113). For the two-point Newton method, $\Delta\bar{\varepsilon}_w^{(1)} = \mathbb{U}_w^{(0)}/2$ is used again to get $\boldsymbol{\beta}^{(1)}$ and $\boldsymbol{\theta}^{(1)}$ from Eq.(3.113).

Conditional isotropic hardening

The computational implementation for the evolution of non-isotropic hardening surface in Eqs.(3.22)-(3.23) is described by Ghaei and Green (2010) or Ghaei et al. (2010) as

$$r^2 = r_n^2 + 3h\boldsymbol{\xi} : \Delta\boldsymbol{\beta}, \tag{3.117}$$

$$\mathbf{q} = \mathbf{q}_n + \Delta\mu\boldsymbol{\xi}, \tag{3.118}$$

$$\boldsymbol{\xi} = \frac{\boldsymbol{\xi}_n}{1+\Delta\mu}, \tag{3.119}$$

$$\Delta\mu = \frac{-3h\boldsymbol{\xi}_n : \Delta\boldsymbol{\beta} + \sqrt{(3h\boldsymbol{\xi}_n : \Delta\boldsymbol{\beta})^2 + 4r_n^2\left(\frac{3}{2}\boldsymbol{\xi}_n : \boldsymbol{\xi}_n\right)}}{2r_n^2} - 1, \tag{3.120}$$

where

$$\Delta\boldsymbol{\beta} = \boldsymbol{\beta} - \boldsymbol{\beta}_n \quad \text{and} \quad \boldsymbol{\xi}_n = \boldsymbol{\beta} - \mathbf{q}_n, \tag{3.121}$$

and these calculations are conditionally performed when $(3/2)(\boldsymbol{\xi}_n : \boldsymbol{\xi}_n) - r_n^2 > 0$.

Update of stress and state variables

When $\Delta\bar{\varepsilon}_l$ and $\Delta\bar{\varepsilon}_w$ are simultaneously obtained, the condition Eq.(3.63) can decide the region and the effective plastic strain is accumulated as

$$\bar{\varepsilon} = \bar{\varepsilon}_n + \Delta\bar{\varepsilon}, \tag{3.122}$$

where $\Delta\bar{\varepsilon} = \Delta\bar{\varepsilon}_l$ for the LB region and $\Delta\bar{\varepsilon} = \Delta\bar{\varepsilon}_w$ for the WH region. Then, the stress is finally updated as

$$\Delta\boldsymbol{\varepsilon}^e = \Delta\boldsymbol{\varepsilon} - \Delta\bar{\varepsilon}_l\mathbf{n}_l \quad \text{or} \quad \Delta\boldsymbol{\varepsilon}^e = \Delta\boldsymbol{\varepsilon} - \Delta\bar{\varepsilon}_w\mathbf{n}_w, \tag{3.123}$$

$$\boldsymbol{\sigma} = \boldsymbol{\sigma}_n + \mathbf{D} : \Delta\boldsymbol{\varepsilon}^e, \tag{3.124}$$

where

$$\mathbf{n}_l = \frac{3}{2}\frac{\mathbf{s} - C_b\boldsymbol{\alpha}_b}{\bar{\sigma}_l} = \frac{3}{2}\frac{\mathbf{s}^T - C_b\boldsymbol{\alpha}_b}{\bar{\sigma}_l^T}, \tag{3.125}$$

and $\mathbf{n}_w$ is given by Eq.(3.83).

3.2.4 Consistent tangent stiffness

When the implicit procedure for the stress update is applied to the implementation of a material model, the consistent tangent operator needs to solve the FE equilibrium equations with the quadratic rate of convergence. The derivation of the consistent tangent operator for the LB mode be started by applying the differential operator to Eq.(3.125) as follows

$$\delta\mathbf{s} = \frac{\bar{\sigma}_l}{\bar{\sigma}_l^T}\delta\mathbf{s}^T + \left(\frac{\delta\bar{\sigma}_l}{\bar{\sigma}_l^T} - \frac{\bar{\sigma}_l}{\bar{\sigma}_l^T}\frac{\delta\bar{\sigma}_l^T}{\bar{\sigma}_l^T}\right)(\mathbf{s}^T - C_b\boldsymbol{\alpha}_b). \tag{3.126}$$

Applying the differential operator to Eq.(3.52) and Eq.(3.64) gives

$$\delta\bar{\sigma}_l^T = \frac{1}{\bar{\sigma}_l^T}\frac{3}{2}(\mathbf{s}^T - C_b\boldsymbol{\alpha}_b) : \delta\mathbf{s}^T, \tag{3.127}$$

$$\delta\bar{\sigma}_l = \delta\bar{\sigma}_l^T - 3G\delta\Delta\bar{\varepsilon}_l. \tag{3.128}$$

Substituting Eq.(3.127) and Eq.(3.128) into Eq.(3.126) with rearrangement yields

$$\delta\mathbf{s} = \frac{\bar{\sigma}_l}{\bar{\sigma}_l^T}\delta\mathbf{s}^T - 2G\delta\Delta\bar{\varepsilon}_l\mathbf{n}_l + \left(1 - \frac{\bar{\sigma}_l}{\bar{\sigma}_l^T}\right)\frac{2}{3}\mathbf{n}_l\left(\mathbf{n}_l : \delta\mathbf{s}^T\right). \tag{3.129}$$

Rewriting Eq.(3.58) as

$$\Delta\bar{\varepsilon}_l = \phi_l\left(\bar{\sigma}_l, \bar{\varepsilon}_l\right)\Delta t, \tag{3.130}$$

where

$$\phi_l\left(\bar{\sigma}_l, \bar{\varepsilon}_l\right) = \frac{bf_m\rho_t}{M}\left(\frac{\bar{\sigma}_l - Y_l - \sigma_{prec}}{D_l}\right)^{n_e}, \tag{3.131}$$

and applying the differential operator provides

$$\delta\Delta\bar{\varepsilon}_l = \left(\frac{\partial\phi_l}{\partial\bar{\varepsilon}_l}\delta\bar{\varepsilon}_l + \frac{\partial\phi_l}{\partial\bar{\sigma}_l}\delta\bar{\sigma}_l\right)\Delta t. \tag{3.132}$$

Substituting Eq.(3.128) and $\delta\bar{\varepsilon}_l = \delta\Delta\bar{\varepsilon}_l$ into Eq.(3.132) and deriving for $\delta\Delta\bar{\varepsilon}_l$ becomes

$$\delta\Delta\bar{\varepsilon}_l = U_l\delta\bar{\sigma}_l^T, \tag{3.133}$$

where

$$U_l = \frac{\dfrac{\partial\phi_l}{\partial\bar{\sigma}_l}}{\dfrac{1}{\Delta t} - \dfrac{\partial\phi_l}{\partial\bar{\varepsilon}_l} + 3G\dfrac{\partial\phi_l}{\partial\bar{\sigma}_l}}, \tag{3.134}$$

$$\frac{\partial\phi_l}{\partial\bar{\varepsilon}_l} = \frac{b}{M}\left(\frac{\partial f_m}{\partial\bar{\varepsilon}_l}\rho_t + f_m\frac{\partial\rho_t}{\partial\bar{\varepsilon}_l}\right)\left(\frac{\bar{\sigma}_l - Y_l - \sigma_{prec}}{D_l}\right)^{n_e}, \tag{3.135}$$

$$\frac{\partial\phi_l}{\partial\bar{\sigma}_l} = \frac{bf_m\rho_t}{M}\left(\frac{n_e}{D_l}\right)\left(\frac{\bar{\sigma}_l - Y_l - \sigma_{prec}}{D_l}\right)^{n_e-1}, \tag{3.136}$$

with

$$\frac{\partial f_m}{\partial\bar{\varepsilon}_l} = \lambda\left(f_{ma} - f_m\right), \tag{3.137}$$

$$\frac{\partial \rho_t}{\partial \bar{\varepsilon}_l} = \chi Z \left(\bar{\varepsilon}_l - x_b\right)^{\chi-1}. \tag{3.138}$$

Plugging Eq.(3.133) into Eq.(3.129) after replacing $\delta\bar{\sigma}_l^T$ in Eq.(3.133) with Eq.(3.127) gives

$$\delta\mathbf{s} = \left[V_l \mathbf{I}_s + \frac{2}{3} Q_l \left(\mathbf{n}_l \otimes \mathbf{n}_l\right)\right] : \delta\mathbf{s}^T. \tag{3.139}$$

where

$$V_l = \frac{\bar{\sigma}_l}{\bar{\sigma}_l^T} \quad \text{and} \quad Q_l = 1 - V_l - 3GU_l. \tag{3.140}$$

Applying the differential operator to the deviatoric stress and its deviator gives

$$\delta\mathbf{s}^T = 2G\mathbf{I}_d : \delta\boldsymbol{\varepsilon}, \tag{3.141}$$

$$\delta\mathbf{s} = \delta\boldsymbol{\sigma} - K(\boldsymbol{I} \otimes \boldsymbol{I}) : \delta\boldsymbol{\varepsilon}, \tag{3.142}$$

where $\mathbf{I}_d$, $\boldsymbol{I}$ and K denote the fourth-order deviatoric projection tensor, the second-order identity tensor, and the bulk modulus, respectively. Substituting Eq.(3.141) and Eq.(3.142) into Eq.(3.139) finally delivers the consistent tangent operator $\mathbf{D}_l^{ep}$ for the LB mode as

$$\delta\boldsymbol{\sigma} = \mathbf{D}_l^{ep} : \delta\boldsymbol{\varepsilon} = \left[2GV_l\mathbf{I}_d + \frac{4}{3} GQ_l \left(\mathbf{n}_l \otimes \mathbf{n}_l\right) + K\left(\boldsymbol{I} \otimes \boldsymbol{I}\right)\right] : \delta\boldsymbol{\varepsilon}. \tag{3.143}$$

The derivation of the consistent tangent operator for the WH mode is analogous to the LB mode. Applying similar procedures to Eq.(3.83) brings

$$\delta\boldsymbol{\eta} = \frac{\bar{\sigma}_w}{\bar{\sigma}_w^{\mathbb{T}}} \delta\boldsymbol{\eta}^{\mathbb{T}} - 2G\delta\Delta\bar{\varepsilon}_w \mathbf{n}_w + \left(1 - \frac{\bar{\sigma}_w}{\bar{\sigma}_w^{\mathbb{T}}}\right) \frac{2}{3} \mathbf{n}_w \left(\mathbf{n}_w : \delta\boldsymbol{\eta}^{\mathbb{T}}\right), \tag{3.144}$$

where

$$\delta\boldsymbol{\eta} = \delta\mathbf{s} - \delta\boldsymbol{\alpha}, \tag{3.145}$$

$$\delta\boldsymbol{\eta}^{\mathbb{T}} = \delta\mathbf{s}^T - \delta\boldsymbol{\alpha}. \tag{3.146}$$

Note that the following relations

$$\delta\bar{\sigma}_w^{\mathbb{T}} = \frac{1}{\bar{\sigma}_w^{\mathbb{T}}} \frac{3}{2} \boldsymbol{\eta}^{\mathbb{T}} : \delta\boldsymbol{\eta}^{\mathbb{T}}, \tag{3.147}$$

$$\delta\bar{\sigma}_w = \delta\bar{\sigma}_w^{\mathbb{T}} - 3G\delta\Delta\bar{\varepsilon}_w, \tag{3.148}$$

are used when Eq.(3.144) is derived. Likewise, for the following equation

$$\Delta\bar{\varepsilon}_w = \phi_w\left(\bar{\sigma}_w, \bar{\varepsilon}_w\right)\Delta t, \tag{3.149}$$

where

$$\phi_w\left(\bar{\sigma}_w, \bar{\varepsilon}_w\right) = \frac{b f_m \rho_t}{M}\left(\frac{\bar{\sigma}_w - Y_w - \sigma_{prec}}{D_w}\right)^{n_e}, \tag{3.150}$$

$\delta\Delta\bar{\varepsilon}_w$ can be expressed as

$$\delta\Delta\bar{\varepsilon}_w = U_w \delta\bar{\sigma}_w^{\mathbb{T}}, \tag{3.151}$$

where

$$U_w = \frac{\dfrac{\partial\phi_w}{\partial\bar{\sigma}_w}}{\dfrac{1}{\Delta t} - \dfrac{\partial\phi_w}{\partial\bar{\varepsilon}_w} + 3G\dfrac{\partial\phi_w}{\partial\bar{\sigma}_w}}, \tag{3.152}$$

$$\begin{aligned}\frac{\partial\phi_w}{\partial\bar{\varepsilon}_w} = {} & \frac{b}{M}\left(\frac{\partial f_m}{\partial\bar{\varepsilon}_w}\rho_t + f_m\frac{\partial\rho_t}{\partial\bar{\varepsilon}_w}\right)\left(\frac{\bar{\sigma}_w - Y_w - \sigma_{prec}}{D_w}\right)^{n_e} \\ & -\frac{b f_m \rho_t}{M}\frac{n_e}{D_w}\left(\frac{\partial Y_w}{\partial\bar{\varepsilon}_w}\right)\left(\frac{\bar{\sigma}_w - Y_w - \sigma_{prec}}{D_w}\right)^{n_e-1},\end{aligned} \tag{3.153}$$

$$\frac{\partial\phi_w}{\partial\bar{\sigma}_w} = \frac{b f_m \rho_t}{M}\left(\frac{n_e}{D_w}\right)\left(\frac{\bar{\sigma}_w - Y_w - \sigma_{prec}}{D_w}\right)^{n_e-1}, \tag{3.154}$$

with

$$\frac{\partial f_m}{\partial\bar{\varepsilon}_w} = \lambda\left(f_{ma} - f_m\right), \tag{3.155}$$

$$\frac{\partial\rho_t}{\partial\bar{\varepsilon}_w} = \chi Z\left(\bar{\varepsilon}_w - x_b\right)^{\chi-1}, \tag{3.156}$$

and

$$\frac{\partial Y_w}{\partial\bar{\varepsilon}_w} = \zeta\left(Y_{wa} - Y_w\right) \quad \text{or} \quad \frac{\partial Y_w}{\partial\bar{\varepsilon}_w} = \frac{\zeta Y_{wa}}{2\cosh^2\zeta\left(\bar{\varepsilon}_w - Y_{w0}\right)}. \tag{3.157}$$

Eliminating $\delta\mathbf{s}^T$ in Eq.(3.146) using Eq.(3.141) gives

$$\delta\boldsymbol{\eta}^{\mathbb{T}} = 2G\mathbf{I}_d : \delta\boldsymbol{\varepsilon} - \delta\boldsymbol{\alpha}. \tag{3.158}$$

Adding Eq.(3.77) and Eq.(3.78) becomes the following equation

$$\delta\boldsymbol{\alpha} = \delta\boldsymbol{\theta} + \delta\boldsymbol{\beta} = \mathbf{h}\delta\Delta\bar{\varepsilon}_w, \tag{3.159}$$

where

$$\mathbf{h} = C\left(\frac{2}{3}a\mathbf{n}_w - \sqrt{\frac{a}{\bar{\theta}}}\boldsymbol{\theta}\right) + m\left(\frac{2}{3}b_1\mathbf{n}_w - \boldsymbol{\beta}\right) \tag{3.160}$$

by Eq.(3.15). Rewriting Eq.(3.158) using Eq.(3.147), Eq.(3.151) and Eq.(3.159) for $\delta\boldsymbol{\eta}^{\mathbb{T}}$ reads

$$\delta\boldsymbol{\eta}^{\mathbb{T}} = \boldsymbol{\Xi} : \delta\boldsymbol{\varepsilon}, \tag{3.161}$$

where

$$\boldsymbol{\Xi} = 2G\left(\mathbf{I}_s + U_w\mathbf{h}\otimes\mathbf{n}_w\right)^{-1} : \mathbf{I}_d. \tag{3.162}$$

Substituting Eq.(3.158) into Eq.(3.145) to remove $\delta\boldsymbol{\alpha}$ yields

$$\delta\boldsymbol{\eta} = \delta\boldsymbol{\sigma} - K\left(\boldsymbol{I}\otimes\boldsymbol{I}\right) : \delta\boldsymbol{\varepsilon} + \delta\boldsymbol{\eta}^{\mathbb{T}} - 2G\mathbf{I}_d : \delta\boldsymbol{\varepsilon}. \tag{3.163}$$

Combining Eq.(3.161) and Eq.(3.163) with Eq.(3.144) lastly brings the consistent tangent operator $\mathbf{D}_w^{ep}$ for the WH mode as

$$\begin{aligned}\delta\boldsymbol{\sigma} &= \mathbf{D}_w^{ep} : \delta\boldsymbol{\varepsilon} \\ &= \left\{2G\mathbf{I}_d + \left[2GV_w\mathbf{I}_s - \frac{4}{3}GQ_w\left(\mathbf{n}_w\otimes\mathbf{n}_w\right)\right] : \boldsymbol{\Xi} + K\left(\boldsymbol{I}\otimes\boldsymbol{I}\right)\right\} : \delta\boldsymbol{\varepsilon},\end{aligned} \tag{3.164}$$

where

$$V_w = \frac{\bar{\sigma}_w}{\bar{\sigma}_w^{\mathbb{T}}} - 1 \quad \text{and} \quad Q_w = V_w + 3GU_w. \tag{3.165}$$

3.2.5 Summary of the overall procedure

A comprehensive flow chart representing the present subroutine and the detailed algorithm of the stress integration is drawn in Fig.3.2. The circled texts ⓐ-ⓔ in this figure indicate the aforementioned iterative methods. In the present study, four possible combinations of the one-point Newton method, the two-point Newton method, and the bisection method are adopted as organized in Table 3.2 to compare the simulation performance of each combination. Except for the part of region selection, the

[1] Although the bisection method is implemented in the subroutine, it is not called during the present simulations when the two-point Newton method is applied for ⓐ and ⓒ.

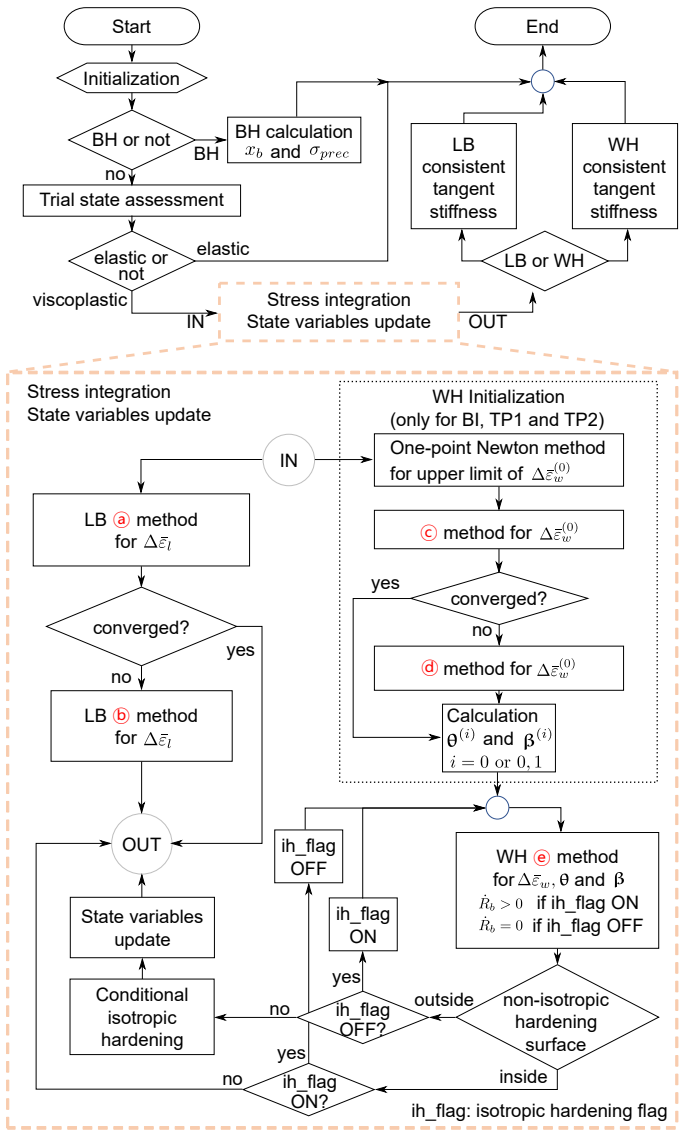

Figure 3.2. Flow chart for the present subroutine and the stress integration algorithm.

Table 3.2. Four stress integration algorithms to solve the constitutive equations.

	ⓐ	ⓑ	ⓒ	ⓓ	ⓔ
OP	One-point Newton	-	-	-	One-point Newton
BI	One-point Newton	Bisection	One-point Newton	Bisection	One-point Newton
TP1	Two-point Newton	(Bisection)[1]	Two-point Newton	(Bisection)[1]	One-point Newton
TP2	Two-point Newton	(Bisection)[1]	Two-point Newton	(Bisection)[1]	Two-point Newton

overall algorithm in Fig.3.2 is similar to typical von Mises-type viscoplastic models Souza Neto et al. (2011). However, particularly in the stress integration procedure, there should be two separate calculations for the LB and WH regions. Furthermore, the initialization and the conditional isotropic hardening algorithm are required for the WH region. Only the OP algorithm intentionally does not have the initialization step to show the non-convergent characteristics of the present model and compare it with the other algorithms. When the converged solutions are not obtained in ⓐ or ⓔ in the OP algorithm and ⓑ,ⓓ or ⓔ in the BI, TP1 and TP2 algorithms, the subroutine lets Abaqus/Standard automatically attempt the current increment again with a new time increment decreased by half unless the maximum number of increments is reached. A UMAT subroutine pseudocode of the proposed algorithm is provided in Appendix A.1.

3.3 Summary

In this chapter, the material modeling for YPP and BH was addressed with their coupling method. For the YPP model, we employed and modified the Yoshida-2008 model by using simple kinematic hardening rules and to consider the true yield-point behavior. To overcome non-convergent characteristics of YPP constitutive equations, we proposed the robust stress integration algorithms that adopt the bisection method and/or the two-point Newton method. For the BH feature of the model, a phenomenological BH model was utilized for considering the formation of the Cottrell atmosphere and the precipitation hardening. The Cottrell effect was taken into account in the way to

calculate the dislocation density ratio, and the precipitation hardening was directly associated with the viscoplastic equations of the YPP model. The YPP part of the model was formulated and implemented implicitly while the BH calculation part was codified and placed before this implicit stress integration steps. The overall procedure was prepared to selectively choose the algorithm combinations for numerical simulations.

Chapter 4

Validation of the Material Model

Numerical simulations to test the four stress integration algorithms of the YPP model in Table 3.2 are carried out using Abaqus/Standard with the corresponding four UMAT subroutines. These YPP simulations exclude BH calculations and the analysis type of the simulations is *Static, General* without the global stabilization control. The automatic time incrementation is selected in the analysis procedure. The material parameters in Table 4.1 and the common parameters in Table 3.1 are used in the YPP simulations. Problems for the YPP simulations include uniaxial tension, simple shear, uniaxial cyclic,

Table 4.1. Material parameters for the YPP simulations.

LB region		WH region								
D_l	Y_l	D_w	Y_{w0}	Y_{wa}	ζ	B_0	C	b_1	m	R_{sat}	h
185	70	120	0.013	70	150	150	1000	20	7	210	0.05

cantilever bending and v-bending.

BH simulations using a single element are also conducted for validating the YPP and BH coupled material model. These BH simulations use the BI algorithm in Table 3.2 and include the analysis type of the *Static, General* as well as that of *Coupled temp-displacement*, both without the global stabilization control. The automatic time incrementation is also selected in this BH analysis. In the UMAT for these simulations,

volumetric heat generation associated with mechanical work of the material and its variations with respect to the strain increments and the temperature as well as variation of the stress increments with respect to the temperature is ignored by assuming that there is no plastic behavior during BH operation.

4.1 Single element analysis

The uniaxial cyclic and the simple shear problems are solved using a single S4R element, 4-node shell element with reduced integration, as shown in Fig.4.1. In the 3-

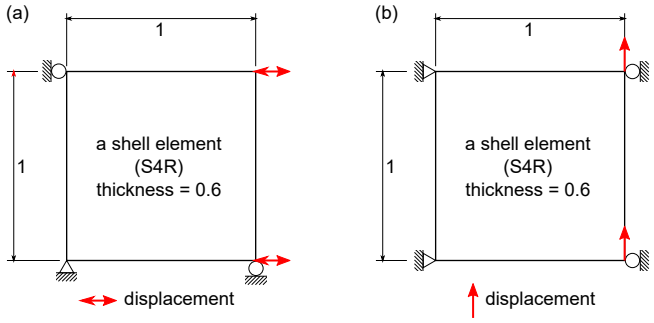

Figure 4.1. FE models for a single element simulations (dimensions in mm): (a) uniaxial cyclic and (b) simple shear.

step (tension-compression-tension) uniaxial cyclic analysis, the speed of the first tension step is 6 mm/min, and that of the compression and second tension steps is 10 mm/min. The compression starts at 2 % of the tension, and the second tension starts at 4 % of the compression. The simple shear is simulated with a speed of 6 mm/min. The stress-strain responses of the single element analysis are depicted in Fig.4.2. All responses show the key features of the YPP such as the upper yield point and the lower yield point. However, the yield-point elongation does not appear because a single element is used only. In Fig.4.2a, the Bauschinger effect is also identified in the cyclic response. Except for OP, the other algorithms provide the same responses. Only the OP algorithm predicts the higher upper yield points and the different stress levels in the strain hardening region.

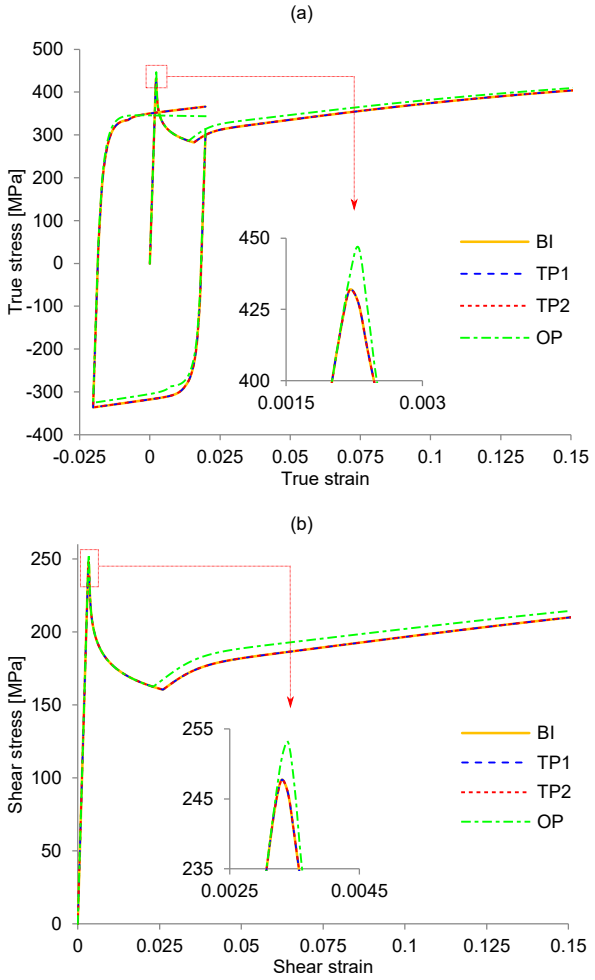

Figure 4.2. Stress-strain responses of the single element analysis: (a) uniaxial cyclic and (b) simple shear.

As plotted in Fig.4.3, the number of increments in the OP algorithm abnormally reaches about 3,000 due to numerous cutbacks of the time increment in the vicinity of the upper yield point in both problems, whereas the other algorithms do not suffer from any cutbacks. It means that the OP algorithm frequently cannot provide converged results in a given time increment near the upper yield point, and this leads to the drastic decrease of the time increment size. Subsequently, the remaining responses are influenced by these increased stresses near the upper yield point. Although the results obtained using

the OP algorithm are not significantly different from those from the other algorithms in single element analysis, a profuse number of increments due to repeated cutbacks can be a critical obstacle to obtain converged solutions in analysis with multiple elements.

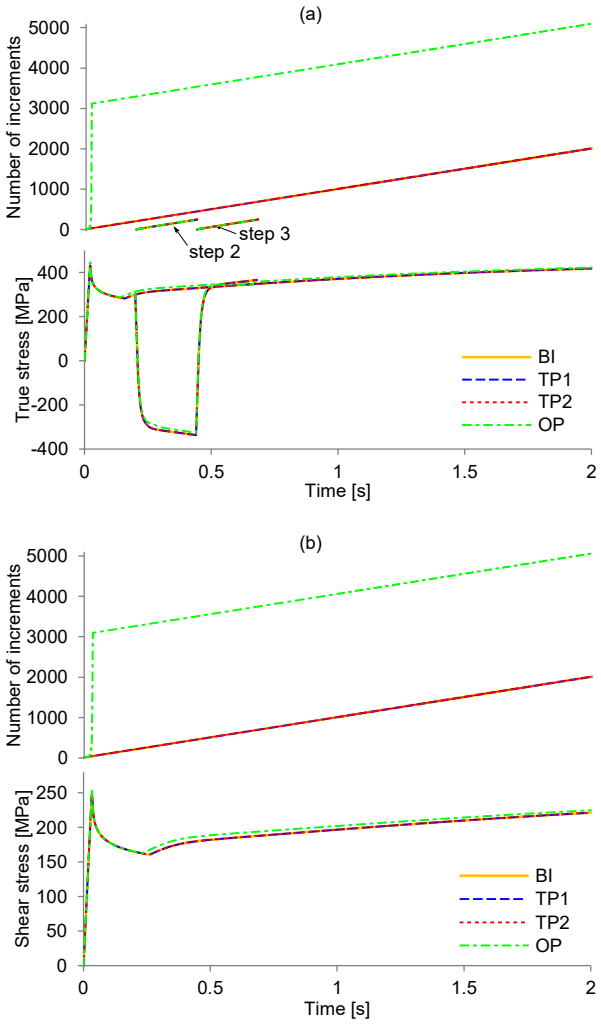

Figure 4.3. History of the number of increments and corresponding stress: (a) uniaxial cyclic and (b) simple shear.

4.2 Uniaxial tension and cyclic simulations

FE models used for the uniaxial tension and the uniaxial cyclic simulations are depicted in Fig.4.4. The dimensions of the uniaxial tension FE model are similar to the standard

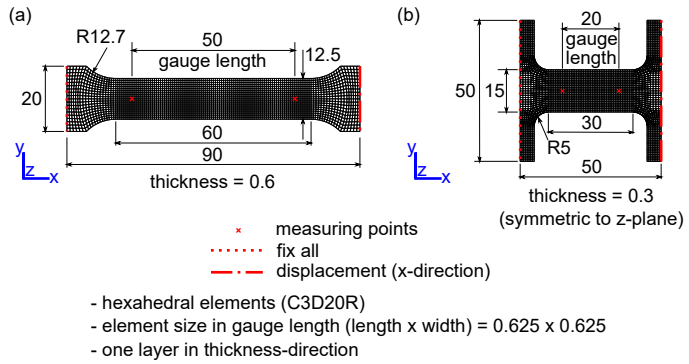

Figure 4.4. FE models for uniaxial simulations (dimensions in mm): (a) uniaxial tension and (b) uniaxial cyclic.

specimen 13B of KS B 0801 (Korean Industrial Standard) and those of the uniaxial cyclic FE model refer to Bae and Huh (2011). Both FE models use quadratic hexahedral elements of type C3D20R with reduced integration. The strains are evaluated from the displacements at the measuring points marked in Fig.4.4. The stresses are calculated from the reaction forces at the fixed nodes. The uniaxial tension simulation consists of a single step, whereas the uniaxial cyclic simulation has three steps: tension, compression, and re-tension. The crosshead speed of the uniaxial tension is 6 mm/min and that of all steps in the uniaxial cyclic is 10 mm/min. The displacement reversal condition for the uniaxial cyclic is the same as the single element simulation. The stress-strain curves obtained using the BI, TP1 and TP2 algorithms in Fig.4.5 show almost no difference. However, both uniaxial tension and cyclic simulations are stopped when the OP algorithm is used as the maximum number of increments (set to 20,000 in this study unless specified) is reached without convergence. It cannot overleap the upper yield point as inferred from the radical increase in the number of increments near the upper yield point observed in the single element analysis.

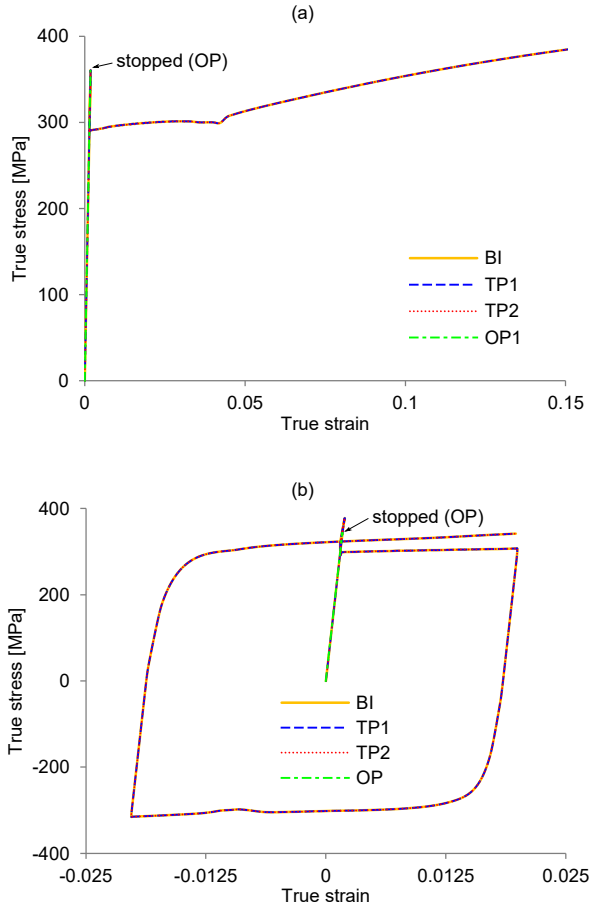

Figure 4.5. Stress-strain responses of uniaxial simulations: (a) uniaxial tension and (b) uniaxial cyclic.

4.3 V-bending simulations

FE models used in the v-bending simulations are shown in Fig.4.6. The workpiece of the 2D v-bending is made up of 8-node biquadratic plane strain elements of type CPE8R with reduced integration. For the 3D v-bending, 8-node doubly curved thick shell elements of type S8R with reduced integration are used. Five integration points are used in the shell element through the thickness. For the 2D v-bending, the punch and the die are constructed with rigid elements of type R2D2, 2-node linear link of size

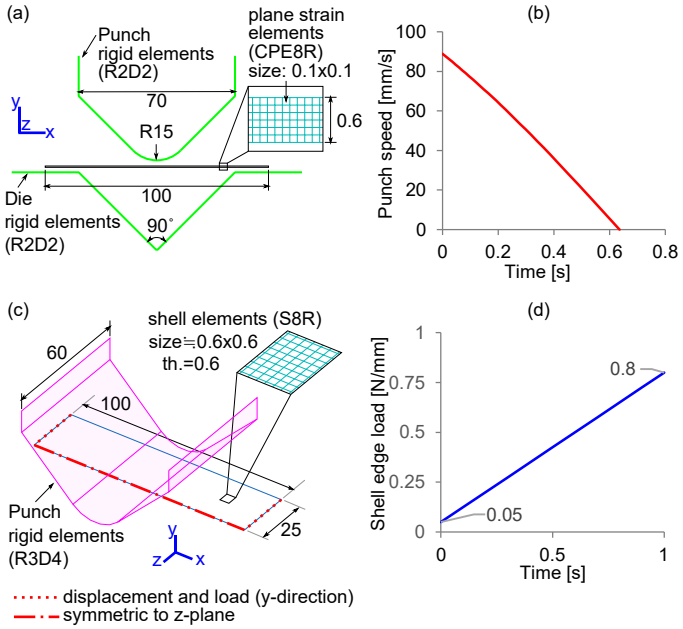

Figure 4.6. FE models with their boundary and load conditions for the v-bending simulations (dimensions in mm): (a) 2D v-bending model, (b) punch speed of the 2D v-bending, (c) 3D v-bending model and (d) load input of the 3D v-bending.

0.05 mm. The punch in the 3D v-bending which has the same dimension in xy plane as the one in 2D is meshed with rigid elements of type R3D4, 4-node bilinear quadrilateral facet. The facet length along the profile in the xy plane is 0.5 mm in the R15 corner and 1.0 mm in the flat area. The facet width in the z-direction is the same as the punch depth in the z-direction. The surface-to-surface contact method with the finite sliding tracking is selected for the interaction type between the tools and the workpiece. The penalty method with the friction coefficient of 0.15 is used for the tangential contact behavior. For the normal contact behavior, the exponential pressure-overclosure rule is applied with the contact pressure of 30 MPa at zero clearance and the clearance of 0.0001 mm at zero contact pressure.

The 2D v-bending simulation begins with moving down the punch by 1.16 mm before touching the workpiece on the die followed by a total stroke of 29.7 mm according

to the speed profile in Fig.4.6b. Then, tools are released to obtain the springback of the workpiece while the center node at its bottom surface is fixed. This simulation setup models an actual v-bending experiment using a servo-controlled mechanical press. In the 3D v-bending, on the other hand, we intentionally change the simulation setup to test the algorithms in force boundary conditions. Here, the workpiece initially positioned 0.4 mm from the punch moves vertically 4 mm upward during a displacement step of one second. Then, the vertical forces are applied at both ends of the workpiece following the linear load history plotted in Fig.4.6d. All loading conditions are released at the last step while fixing the center node of the workpiece on the line of symmetry.

Fig.4.7 shows the vertical displacements of the bottom nodes obtained from the 2D v-bending simulations. The algorithm BI, TP1, and TP2 provide almost identical

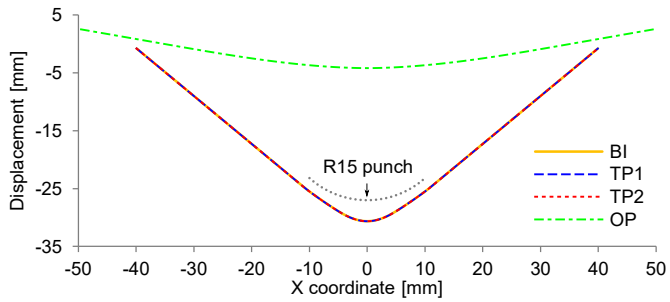

Figure 4.7. Vertical displacements of the bottom nodes in the 2D v-bending simulations.

deformations and clearly predict the fluting with a sharp bending radius. On the other hand, with the OP algorithm, the analysis stops as it reaches its maximum number of increments in the v-bending step. As illustrated in Fig.4.8, the OP algorithm suffers from difficulties in finding a solution near the upper yield point as shown in the distribution and history of the effective stress around the bending center at the last increment.

The 3D v-bending simulations provide similar results as the 2D v-bending simulations. They are successfully completed and almost the same bent shapes are obtained as plotted in Fig.4.9a except when the OP algorithm is used. The analysis with the OP algorithm is terminated in the middle of the second step since it reaches the maximum

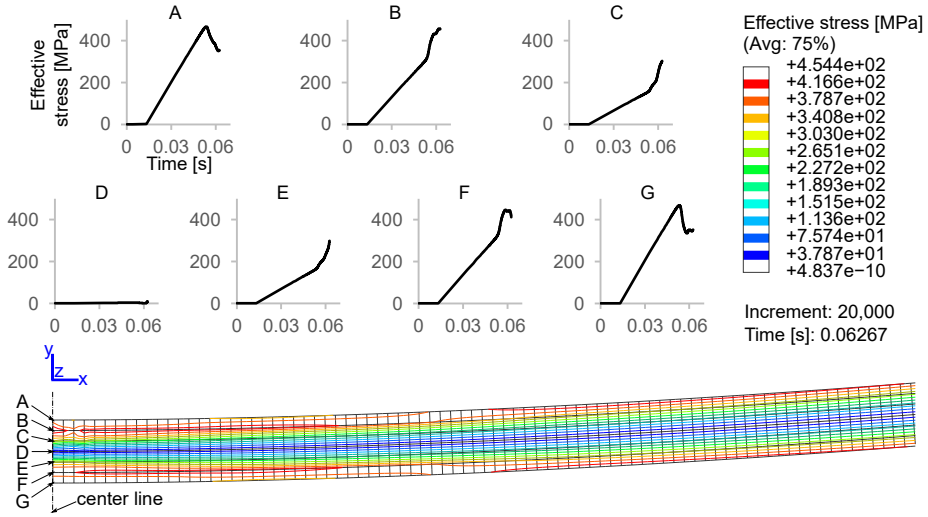

Figure 4.8. Contour plot of the effective stress around the bending center at the last increment of the OP algorithm in the 2D v-bending simulation with the stress histories of the center nodes.

number of increments (set to 10,000). Analogously to the 2D case, the OP algorithm cannot fully pass over the upper yield point (Fig.4.9b), while the other algorithms can surmount it and enter into the springback step (Fig.4.9c). As observed in the 2D v-bending, the fluting is also clearly seen in the 3D v-bending simulations.

4.4 Cantilever bending simulation

The cantilever bending simulation is performed using the FE model in Fig.4.10a where cyclic loads are applied at one end as in Fig.4.10b. The same type of shell element as in the 3D v-bending is used in this simulation. Interestingly, the analysis can be completed only when the TP2 algorithm is used (Fig.4.11). The simulations using the BI and TP1 algorithms are aborted as the minimum time increment or the maximum attempts in an increment is reached before completion of the analysis. The analysis using the OP algorithm is terminated at a very early stage. This problem with a serrated cyclic loading might be a highly non-convergent problem as high plastic strains are accumulated near

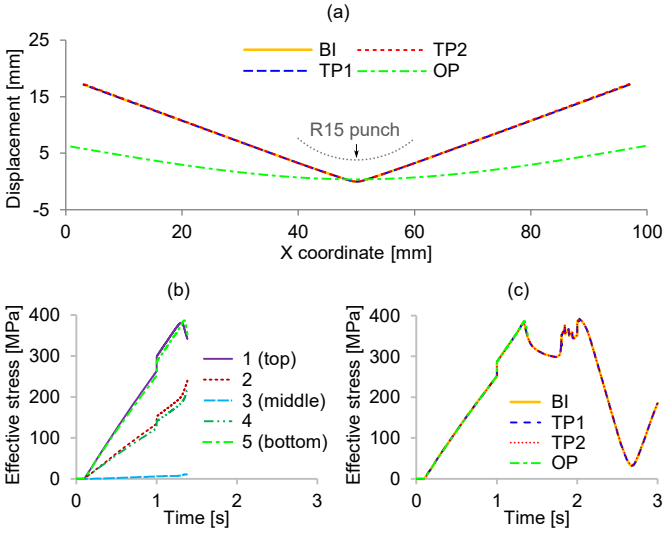

Figure 4.9. Results of the 3D v-bending simulations: (a) Vertical displacements of the nodes at the symmetry line, (b) stress histories of the center element of which edge lies on the symmetry line in the OP algorithm (element centroid value of integration points), and (c) stress histories of the same element as (b) at the bottom centroid in the four algorithms.

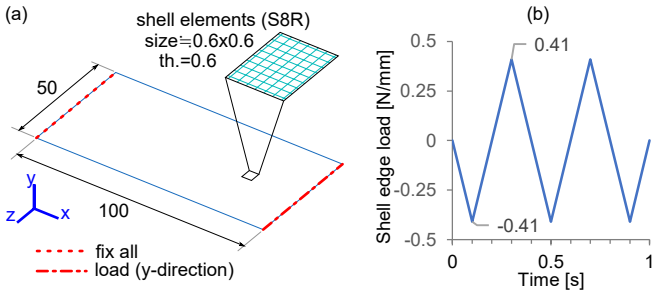

Figure 4.10. FE model with its boundary and load conditions for the cantilever bending simulation: (a) FE model and (b) corresponding load input.

the clamped end and very unstable stress states are developed (Fig.4.11b), whose solution cannot be easily obtained even with robust iterative methods.

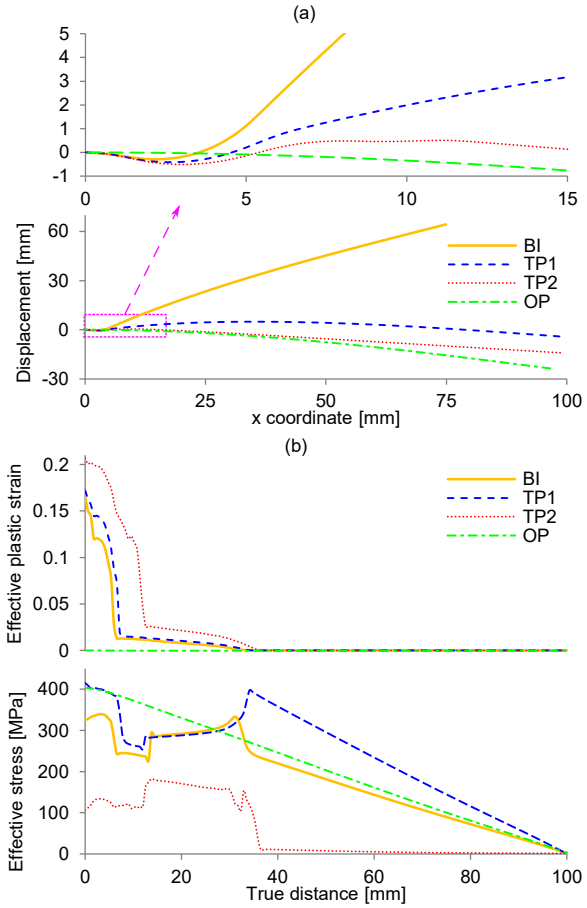

Figure 4.11. Cantilever bending results at the nodes of the width center line: (a) vertical displacements and (b) effective plastic strain and effective stress (averaged with the 75 % averaging threshold at the top integration points).

4.5 Performance comparison

All present simulations are carried out using a PC with four CPU cores (Intel Core i5-6600 3.3 GHz) and one GPU core (NVIDIA Quadro K620 2 GB) with 16 GB of system memory. Computation times and total increments including time increment cutbacks are listed in Table 4.2. In the single element (S.E.) simulations, the CPU times and the wall clocks are similar to each other as only a single CPU core is engaged in

Table 4.2. CPU times, wall clocks, total increments and cutbacks of the simulations. (Ratios in CPU time and wall clock is calculated with respect to the BI case.)

	Case	CPU time [s] (ratio)	Wall clock [s] (ratio)	Total increments	UMAT cutbacks	Total cutbacks	Completion [%]
S.E. uniaxial cyclic 3-step	OP	1,469 (1.70)	1,511 (1.45)	5,601	1,812	1,812	100.00
	BI	863 (1.00)	1039 (1.00)	2,513	0	0	100.00
	TP1	849 (0.98)	961 (0.92)	2,513	0	0	100.00
	TP2	856 (0.99)	979 (0.94)	2,513	0	0	100.00
S.E. simple shear 1-step	OP	1,299 (1.81)	1,391 (1.74)	5,062	1,790	1,790	100.00
	BI	717 (1.00)	798 (1.00)	2,011	0	0	100.00
	TP1	706 (0.98)	800 (1.00)	2,011	0	0	100.00
	TP2	727 (1.01)	826 (1.04)	2,011	0	0	100.00
Uniaxial tension 1-step	OP	80,293	24,460	20,000	11,695	11,695	1.28
	BI	2,942 (1.00)	894 (1.00)	376	11	17	100.00
	TP1	2,890 (0.98)	881 (0.99)	376	11	18	100.00
	TP2	3,436 (1.17)	1,019 (1.14)	376	11	18	100.00
Uniaxial cyclic 3-step	OP	70,416	21,608	20,000	11,549	11,549	1.60
	BI	68,687 (1.00)	20,918 (1.00)	30,077	102	102	100.00
	TP1	70,074 (1.02)	21,312 (1.02)	30,100	132	132	100.00
	TP2	81,052 (1.18)	24,092 (1.15)	30,100	132	132	100.00
2D v-bending 2-step	OP	263,780	146,731	20,000	11,702	11,702	3.83
	BI	13,041 (1.00)	7,854 (1.00)	446	102	119	100.00
	TP1	12,621 (0.97)	6,659 (0.85)	438	86	107	100.00
	TP2	14,070 (1.08)	7,104 (0.90)	450	107	125	100.00
3D v-bending 3-step	OP	211,581	66,740	10,083	5,893	5,895	46.00
	BI	8,177 (1.00)	2,576 (1.00)	282	18	20	100.00
	TP1	8,127 (0.99)	2,558 (0.99)	282	18	20	100.00
	TP2	10,033 (1.23)	3,052 (1.18)	275	25	25	100.00
Cantilever bending 1-step	OP	138,899	39,352	5,725	3,340	3,365	6.80
	BI	30,342	8,404	595	252	298	46.10
	TP1	45,228	12,457	993	495	532	49.70
	TP2	194,436	51,522	2,783	1,509	1,541	100.00

analysis. In other simulations where multiple elements are used, the CPU times are about 1.7 to 3.8 times longer than the wall clocks as multiple CPU cores are used. The simulations with the OP algorithm are all terminated around at the upper yield point except when a single element is used. Although we can obtain completed solutions for single element simulations with the OP algorithm, they are slightly different from the solutions obtained using other algorithms and it takes about 1.45 to 1.74 times longer

than when the BI algorithm is used. Therefore, it is not suitable to use the conventional one-point Newton method for the analysis of materials with the YPP. Note that 46 % of analysis is completed using the OP algorithm for the 3D v-bending simulations, but the completed solutions correspond to the displacement step which is not associated with the upper yield point.

Overall, BI, TP1 and TP2 algorithms demonstrate their robustness in most problems. The TP1 algorithm requires a slightly shorter computing time in general and the TP2 algorithm turns out to be the most robust. It seems appropriate to use the two-point Newton method for highly nonlinear problems when convergence is hardly achieved by using the conventional one-point Newton method. These test results suggest that the TP2 algorithm may be useful particularly in solving non- or hardly-convergent problems such as the YPP even though it might be slower than the one-point Newton method in solving normal, convergent problems. In practice, one can use both one-point and two-point Newton methods adaptively so that the stress integration algorithm chooses one of these methods by monitoring the convergence histories during analysis.

4.6 Single element BH simulations

Uniaxial tension and compression simulations including BH step are performed using a single element C3D8RT, 8-node trilinear displacement and temperature with reduced integration and enhanced hourglass control. The boundary conditions are shown in Fig.4.12. The simulations have 4-step analysis: a uniaxial tension, unloading, BH, and tension or compression. The initial temperature of this analysis is 20 °C and applies all nodes as the *Predefined fields*. The first and second steps are uniaxial pre-strain step with the speed of 6 mm/min (0.1 mm/sec) and unloading step, respectively. The third BH step uses the temperature history shown in Fig.2.15. This temperature boundary condition applies to all nodes. The maximum time increment size of the third step is set to 10 seconds. The last step at the same speed as the first step can be tension or

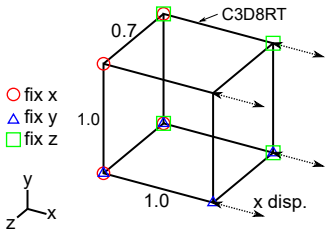

Figure 4.12. FE model for a single element BH simulations with boundary conditions (dimensions in mm).

compression according to simulation conditions.

The material parameters used in the simulations are shown in Table 4.3. The free

Table 4.3. Material parameters for the BH simulations.

Common parameters

E [GPa]	ν	b [mm]	M	f_{m0}	f_{ma}	λ	ρ_0	Z	χ	n_e
212.9	0.3	2.5e-7	2.76	1.0e-5	0.1	10	1.0e4	3.0e9	1.5	30

LB region		WH region								
D_l	Y_l	D_w	Y_{w0}	Y_{wa}	ζ	B_0	C	b_1	m	R_{sat}	h
185	160	120	190	190	20	190	150	140	18	180	0.01

BH parameters

$\mathbb{A}$ [Nmm^2]	D_0 [mm^2/s]	Q_d [J/mol]	R_{gas} [J/mol°K]	s_b	k [mJ/°K]
3.0e-23	2.0	8.4e4	8.314	9.5e11	1.38e-20

BH parameters

n_c [ppm]	n_0 [ppm]	C_b	G_{Fe} [MPa]	X_p [mm]	C_{prec}
779.21	82,245	0.7	81,600	5.0e-5	5.0e6

carbon concentration n_c is obtained from Thermo-Calc with the TCFE-9 database at the annealing temperature of 778 °C. Other mechanical and thermal constants necessary for the *Coupled temp-displacement* analysis are a material density of 7.89e-9 tonne/mm^3, the thermal conductivity of 58.8 mW/mm°K, the thermal expansion coefficient of 1.2e-5 /°K at 20 °C, and constant volume specific heat of 4.46e8 mJ/tonne°K. These constants are used throughout the present study. The simulations start with the initial

value of the effective plastic strain as $\bar{\varepsilon}_0 = 0.02$ assuming that objective material does not show YPP initially.

The simulation cases are the same as shown in Table 2.2, including the detail conditions of pre-strain, BH temperature and BH time. Stress-strain responses in these conditions are plotted in Fig.4.13-4.16. In Fig.4.13, the BH responses according to

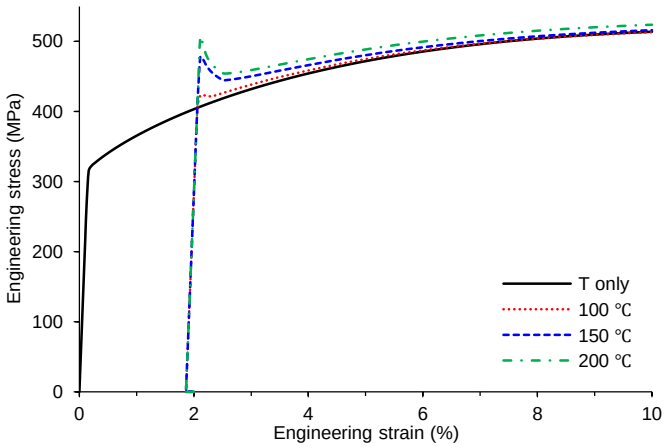

Figure 4.13. Stress-strain responses of the 'T-U-BH-T' cases according to the BH temperature in the single element BH simulations with the BH time of 20 min and the pre-strain of 2%.

the BH temperature are described. Two higher temperature cases show clear YPP as expected, and even with 100 °C, the slightly increased upper yield point is captured. The responses with respect to the BH time and the pre-strain are plotted in Fig.4.14. Similar upper yield points between 5, 20, and 35 min are recorded, and those according to the pre-strain are weakly elevated than the strain hardening slope. While, in the strain hardening region, small stress differences with respect to the BH time and the pre-strain are identified. In Fig.4.15, tension-compression responses are shown, and the kinematic hardening behaviors are exhibited in these responses. Compressive responses after the BH step in Fig.4.15 show YPP but not as strong as the YPP in tension cases.

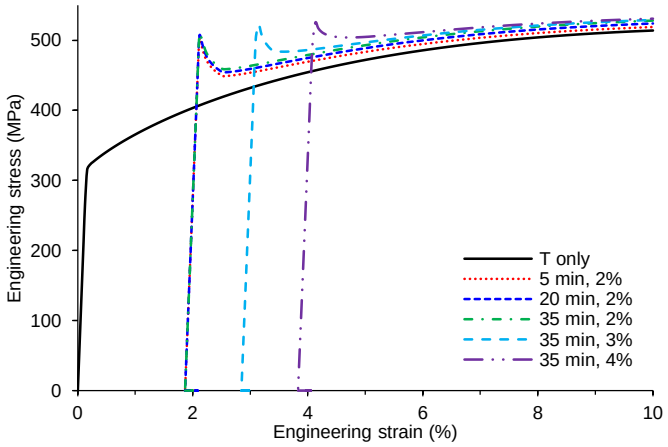

Figure 4.14. Stress-strain responses of the 'T-U-BH-T' cases according to the BH time and the pre-strain in the single element BH simulations with the BH temperature of 200 °C.

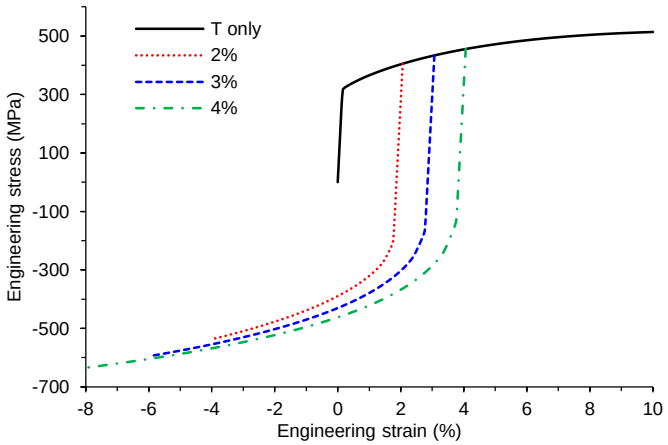

Figure 4.15. Stress-strain responses of the 'T-C' cases according to the pre-strain in the single element BH simulations with the 'T only' case.

4.7 Summary

In this chapter, the material model that adopts the bisection method and/or the two-point Newton method for stress integration was validated to check its robustness in solving

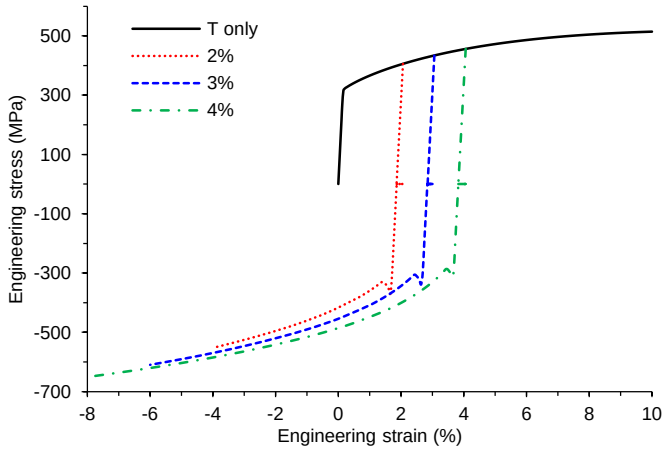

Figure 4.16. Stress-strain responses of the 'T-U-BH-C' cases according to the pre-strain in the single element BH simulations with the BH temperature of 200 °C and the BH time of 35 min.

YPP-related non-convergent problems. These methods are shown to be much more effective in performing the YPP-related simulations than the conventional one-point Newton method. While these algorithms may require longer computational times, they can be reliably used to calculate the solutions of YPP problems that cannot be obtained using conventional iterative methods. The BH feature of the material model was also verified using single element simulations with various BH conditions. As a result, a possibility that the present material model can be utilized in predicting the BH potential of bake hardenable material is identified.

Chapter 5

Numerical Analysis

In this chapter, FE simulations corresponding to the experiments are performed to study the capabilities of the present material model for describing the fluting defect of PLCS and the BH behavior of 490DP. In these simulations, the BI algorithm in Table 3.2 is used. For the simulations of the fluting defect with PLCS, the *Static, General* analysis procedure is chosen without using the global stabilization control. The material parameters are determined by comparing the simulation results with the experimental ones for uniaxial tension and cyclic cases. In contemplation of true material behaviors related to the YPP, three sets of the parameters, two for Eq.(3.13) and one for Eq.(3.14), are chosen and tested. With these parameter sets, the v-bending simulations followed by the roller-leveling simulations are performed.

The simulations for the BH behavior of 490DP include the analysis type of the *Static, General* and the *Coupled temp-displacement*. These simulations ignore volumetric heat generation and its variations with respect to both the strain increments and the temperature. The variation of the stress increments with respect to the temperature is also ignored in the UMAT subroutine. The simulations does not use the global stabilization control, whereas, in order to have better convergent characteristics in the global iterative loop, the simulation step after BH uses the *Discontinuous analysis* option, activates the *Line Search Control*, and sets the maximum number of cutbacks

allowed for an increment to 10-15 in the *General Solution Controls*. The automatic time incrementation is also selected.

5.1 Numerical simulations of fluting defect and its reduction method for PLCS

5.1.1 Uniaxial tension and cyclic simulation

FE models used for the uniaxial tension and cyclic simulations for PLCS are the same as the models in Fig.4.4. The mesh is generated so as to minimize the distortion of the elements in the transition area from the grip section to the gauge section. In the uniaxial tension simulation, a total of 2,680 quadratic hexahedral elements of type C3D20R with reduced integration are used to construct the model in Fig.4.4a. Among them, 1,600 elements of size 0.625 mm x 0.625 mm x 0.6 mm are occupied in the gauge section. In the uniaxial cyclic simulation, a total of 2,464 elements of the same type are used as depicted in Fig.4.4b where 768 elements of size 0.625 mm x 0.625 mm x 0.3 mm are in the gauge section. Symmetric boundary conditions in the thickness direction are imposed on one side of uniaxial cyclic specimens to avoid buckling. The strain is calculated with the displacements of measuring points indicated in Fig.4.4 and the stress is evaluated from the reaction force of the fixed end. In addition, the uniaxial tension simulations using a single shell element are carried out to investigate the true yield-point behavior, such as a higher upper yield point and a degraded lower yield point, evaluated by several ways in Schwab and Ruff (2013).

After comprehensive parametric studies for these simulations, three simulation sets of material parameters are established as listed in Table 5.1 and 5.2. The common parameters related to the dislocation density are gleaned from Yoshida (2000). Here, the material parameters in sim.2 and sim.3 sets are chosen to describe the true yield-point behavior better. Eq.(3.13) is used for sim.1 and sim.2 sets while Eq.(3.14) is used instead for sim.3 set. Note that, sim.1 set represents a constant yield surface of

Table 5.1. Common material parameters.

E (GPa)	ν	b (mm)	M	f_{m0}	f_{ma}	λ	ρ_0	Z	χ	n_e
199.5	0.3	2.5e-7	2.76	1.0e-5	0.1	10	1.0e4	3.0e9	1.5	20

Table 5.2. Material parameter sets.

Set	D_l	Y_l	D_w	Y_{w0}	Y_{wa}	ζ	B_0	C	b_1	m	R_{sat}	h
sim.1	130	150	120	70	70	20	150	500	20	7	210	0.1
sim.2	185	70	120	5	70	70	150	1000	20	7	210	0.05
sim.3	185	70	120	0.013	70	150	150	1000	20	7	210	0.05

Yoshida and Uemori (2003), and sim.2 set uses an exponential change of the yield surface similar to Yoshida et al. (2008). The tangent hyperbolic evolution of the yield surface in sim.3 set is the newly proposed rule for the yield surface evolution in the present material model.

The stress-strain curves obtained from the single element uniaxial tension simulations at the crosshead speed of 6 mm/min are plotted in Fig.5.1 as well as one experimental curve at the same speed. The upper yield points of sim.2 and sim.3 sets

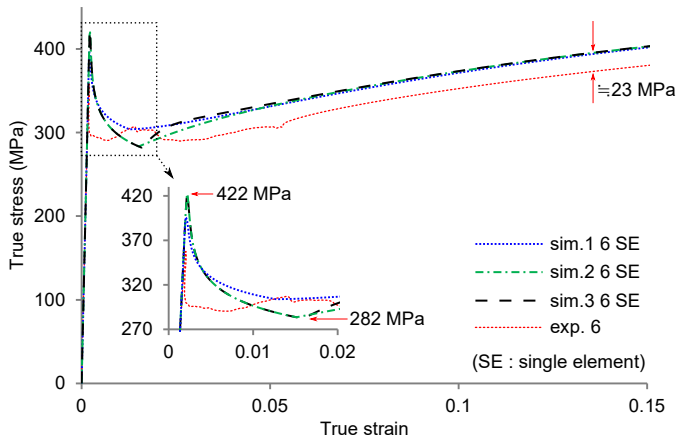

Figure 5.1. Stress-strain curves obtained from the uniaxial tension simulations using a single shell element at the crosshead speed of 6 mm/min.

are higher than that of sim.1 set as higher D_l and lower Y_l values are used in LB mode. Similarly, the lower yield points of sim.2 and sim.3 sets are smaller than that of sim.1 set as lower Y_{w0} values are used. In sim.3 set, Y_w saturates to Y_{wa} much faster than sim.2 set due to the hyperbolic tangent function in Eq.(3.14) that can describe a higher rate of strain hardening after the lower yield point as shown in Fig.5.1. Hence, it seems sim.3 set can capture the true yield-point behavior more closely than sim.2 set. Note that the experimental curve shows a smaller stress level of about 23 MPa compared to single element simulations. This difference is because the region of gauge length deforms slower than the crosshead speed due to specimen shape, unlike the single element simulations where the strain rate corresponding to the crosshead speed is applied uniformly.

The increased upper yield value of 422 MPa and the decreased lower yield value of 282 MPa in the single element simulation with the sim.3 set can be validated by the analytical expression for the observed lower yield value suggested in Schwab and Ruff (2013). The observed lower yield point can be calculated as

$$R_{\mathrm{eL(obs)}} = \frac{R_{\mathrm{eH(tr)}} + \sqrt{R_{\mathrm{eH(tr)}}^2 + 8R_{\mathrm{eL(tr)}}^2}}{4} = 331 \text{ MPa}, \tag{5.1}$$

where $R_{\mathrm{eH(tr)}}$ and $R_{\mathrm{eL(tr)}}$ denote the true upper yield point and the true lower yield point, respectively. Subtracting the stress difference of 23 MPa between the experiment and single element simulations results in $R_{\mathrm{eL(obs)}}$ of 308 MPa, which is similar to the experimentally observed lower yield point.

Stress-strain curves obtained from uniaxial tension simulations at the three different crosshead speeds using the FE model for the experimental specimen in Fig.4.4a are plotted in Fig.5.2 with the experimental ones. Experimental curves in Fig.5.2 are chosen from the data shown in Fig.2.2 for each crosshead speed. Note that the experimental curves which exhibit the increase of the yield-point elongation with respect to the crosshead speed are selected even though no clear tendency is observed in the overall data. The model can capture the effect of crosshead speed on the yield-point behavior

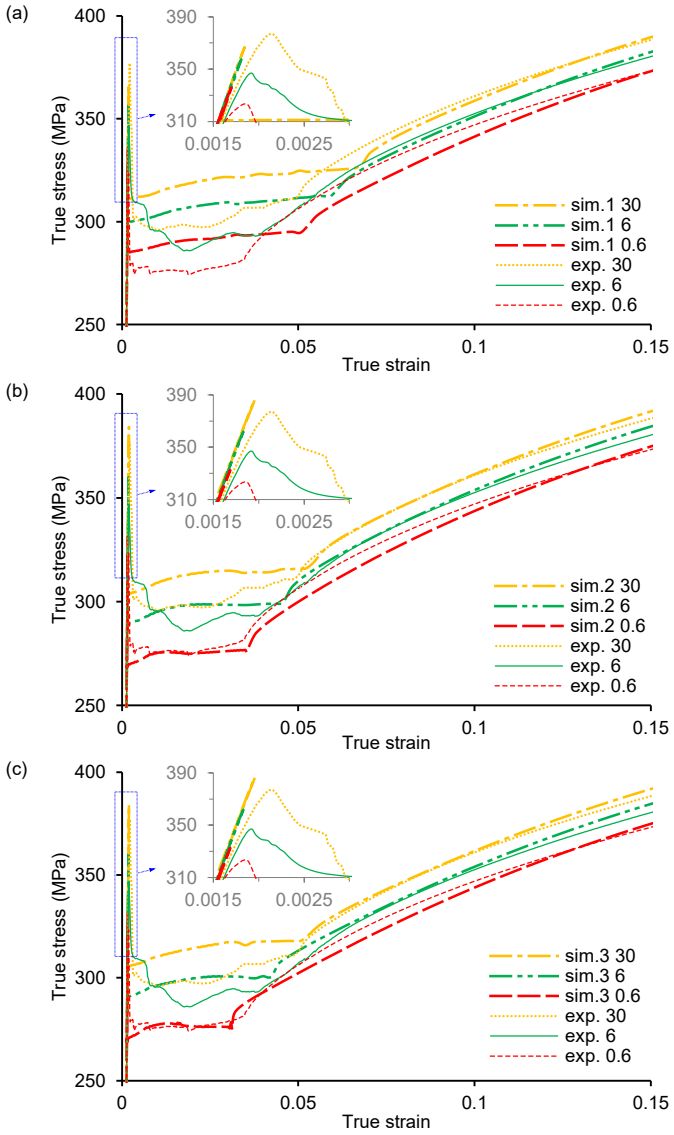

Figure 5.2. Stress-strain curves obtained from uniaxial tension simulations using the FE model for experimental specimen conducted at 0.6, 6, and 30 mm/min with the parameter sets (a) sim.1, (b) sim.2 and (c) sim.3.

observed in the selected experimental data successfully. The predicted upper yield points are quite similar to the experimental values, whereas the lower yield points and the yield-point elongations show some discrepancy between the simulated and

measured values particularly when sim.1 set is used regardless of the crosshead speed. The parameter sets of sim.2 and sim.3 are working pretty well except for the crosshead speed of 30 mm/min, and the sim.3 set reveals slightly better results at 0.6 mm/min among them. Nevertheless, the predicted stress-strain curves in Fig.5.2 agree well with the experimental ones in the strain hardening region. Overall, the parameter set sim.3 shows the best fit in all regions probably due to its consideration for the true yield-point behavior.

Fig.5.3 illustrates the stress-strain curves obtained from uniaxial cyclic simulations in the strain range of 4% at the crosshead speed of 10 mm/min using the FE model for the experimental specimen in Fig.4.4b. The predicted upper yield points are slightly

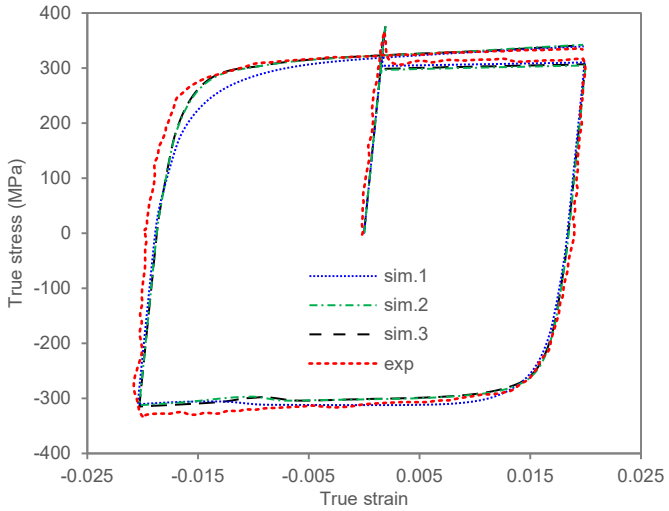

Figure 5.3. Stress-strain curves obtained from uniaxial cyclic simulations using the FE model for the experimental specimen in the strain range of 4% at the crosshead speed of 10 mm/min.

higher than the experimental value by 6 to 14 MPa while the predicted stress level in the lower yield region is slightly smaller than the experimental one by 8 to 15 MPa. All simulated curves moderately fit the experimental result in *the transient Bauschinger deformation* stated in Yoshida and Uemori (2003) during the compression. But the

curve obtained using the parameter set sim.1 shows a slow transient hardening behavior in the second tension while the results using other parameter sets look acceptable. The stress drop after the beginning of strain hardening at the latter part of the compression in simulated curves is induced by the completion of the yield-point elongation, which is not observed in the experiments.

5.1.2 Roller-leveling and v-bending simulations

The roller-leveling and the v-bending simulations for PLCS are performed using the FE model for the material illustrated in Fig.5.4. The model is 900 mm long and composed

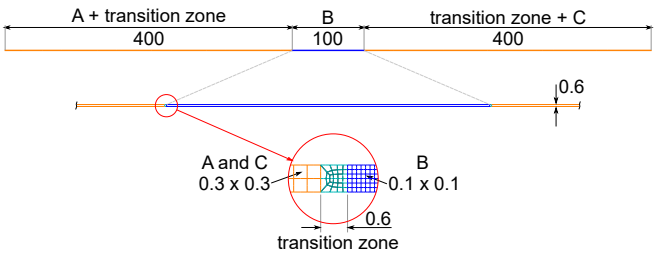

Figure 5.4. FE model for the material in the roller-leveling and v-bending simulations.

of three instances from A to C discretized using 8-node biquadratic plane strain elements of type CPE8R with reduced integration. The reason for using 2-D elements is due to computational efficiency. Nevertheless, the 2-D simulations results such as the radius of curvature and the bending angle would be almost the same as the case in which 3-D elements are adopted except for specimen edges. Because the specimen width of roller-leveling and v-bending experiments is 50-100 mm and the corresponding experimental results in the deformed shape after the v-bending test are measured by using laser scanned mid-sectional curves. This mid-sectional area can be assumed as a plane strain condition. The instances A and C are dummy instances whereas the instance B is a target instance used for the v-bending simulations. For computational efficiency, the element size of dummy instances is set to 0.3 mm x 0.3 mm while the element size of 0.1 mm x 0.1 mm is used for the target instance as depicted in Fig.5.4.

The instances are connected to each other by transition zones of 0.6 mm long.

FE models for the tools are meshed with 2-D rigid elements of type R2D2. The element sizes for the roll and v-bending tools are 0.2 mm and 0.05 mm, respectively. The tool dimensions specified in Fig.2.5a for the roller-leveling and in Fig.1.3a for the v-bending are used.

The surface-to-surface contact discretization method between the material and the tools is implemented with the finite sliding tracking approach. The penalty method is employed for tangential behaviors with a friction coefficient of 0.15. This coefficient is an averaged value from the data of friction experiments which were conducted without lubricant considering no lubricant condition in roller-leveling and v-bending experiments. Because of this condition, the friction coefficients obtained from these experiments were scattered in the range of 0.12 to 0.19. For normal behaviors, the exponential pressure-overclosure relationship is selected with the contact pressure of 30 MPa at zero clearance and the clearance of 0.0001 mm at zero contact pressure. This softened contact relationship is adopted for better convergence. The solution using this softened contact condition can be as accurate as the one provided by the hard contact condition in the Hertzian contact problem (see Appendix A.2).

The FE analysis procedure is established for the roller-leveling and the v-bending simulation as illustrated in Fig.5.5. Here, the figure for each step displays the last state within the step. Starting with the initial state where the upper and lower rolls just touch the material, the intermesh condition in Table 2.1 is applied in the first step by the downward displacement of upper rolls. In the second step, every roll rotates for 11 seconds at the same speed used in the experiment while maintaining the vertical position of the rolls. The time period of 11 seconds is sufficiently long for the target instance to pass all the rolls during the second step. At the beginning of the third step, the dummy instances are removed and the target instances are horizontally translated to the position for the v-bending simulation. Simultaneously, the tools are vertically translated to the position at which the die touches the material and the punch has the

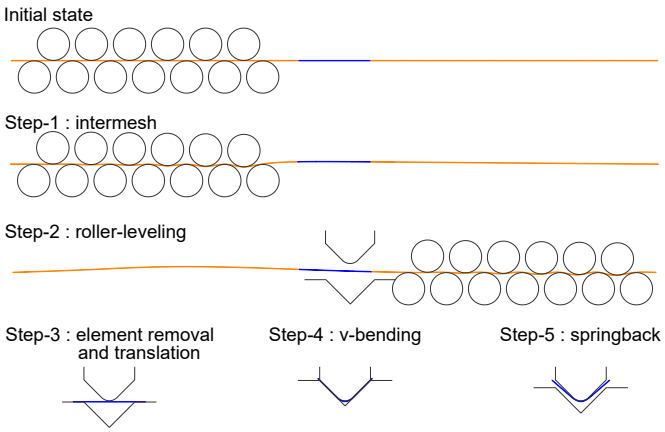

Figure 5.5. FE analysis procedure for the roller-leveling and v-bending simulations.

last stroke of 29.70 mm. The fourth step is the v-bending process which uses the punch speed shown in Fig.2.9. The springback calculation is performed in the last step. In the v-bending simulation for materials in the as-received condition, the first two steps are simply skipped. In the following simulation results, the element-based output values such as stresses and strains are averaged at the nodes with the averaging threshold of 75% in Abaqus/CAE.

The rate dependency of the fluting in the v-bending simulation

The v-bending simulations for materials in the as-received condition are carried out at four different punch speeds. Fig.5.6 shows the final deformed shapes predicted by the present procedure using the parameter set sim.3 along with the experimentally measured ones. The experimental curve corresponding to punch speed is chosen from three experimental data conducted in the same condition. The predicted curves are shifted to the experimental ones so that their bottom points coincide. The fluting clearly appears in all the predicted curves and their radii of curvature are quite similar to those of the experimental curves. However, the predicted curves are a little bit deviated from the experimental ones near the tips indicating the simulated shapes are bent a little bit more inwards.

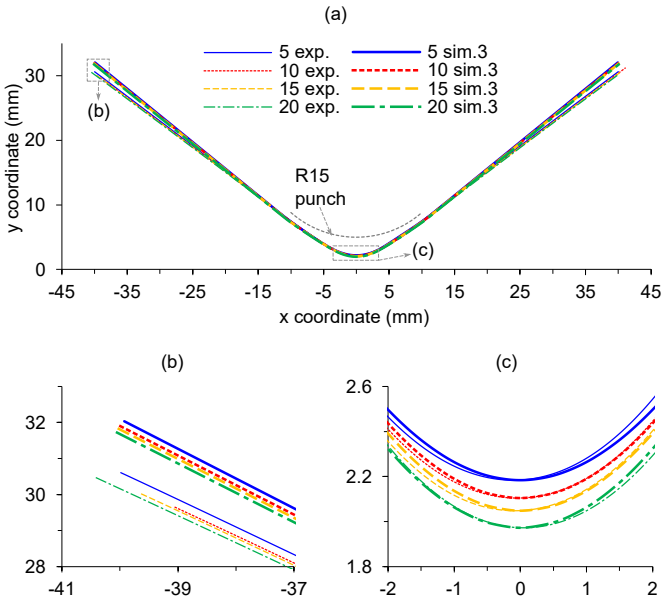

Figure 5.6. Results of the v-bending simulations for materials in the as-received condition performed using the parameter set sim.3 at four different punch speeds (5, 10, 15 and 20 SPM): (a) deformed shapes and (b)-(c) close-up views of the deformed shape.

A more quantitative comparison of the curves in terms of R and A is given in Fig.5.7. As observed in experiments, R decreases monotonically and A increases slightly with the punch speed in simulations. The calculated R values using the parameter set sim.2 are the closest to the experimental ones. As the fluting occurs in every simulation case, the predicted R values are much smaller than the punch radius of 15 mm. The calculated A values are smaller than the experimental ones by about four degrees regardless of the used parameter set. This angle difference is clearly seen in the plot of tangent slopes shown in Fig.5.8. Experimental curves exhibit a step-like, sudden slope change around the deflection point. In contrast, the simulation predicts a more gradual increase in the tangent slope of the deformed shape, resulting in a higher tangent slope near the tips. This result suggests that the plastic strain might be less localized around the deflection point in the simulations than in experiments. It is probably because the contact model used here has a limitation in modeling the real frictional contact condition accurately.

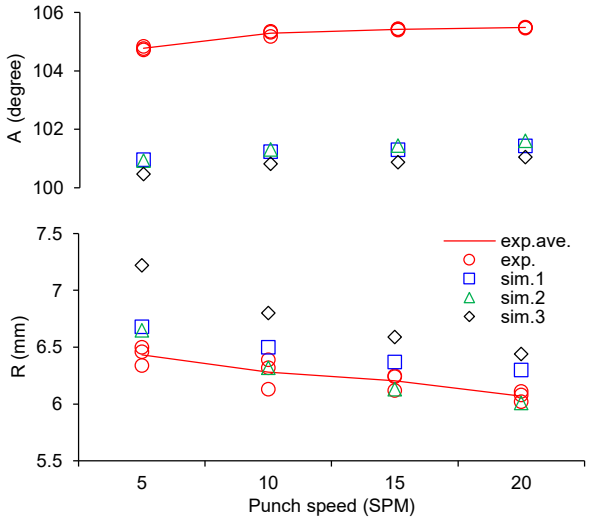

Figure 5.7. Comparison between the predicted and experimental R and A values in the as-received condition.

The time evolution of the effective stress, the effective plastic strain and the displacement profiles along the curve during the v-bending simulation reveals how the fluting affects the deformed shape of the material (Fig.5.9). These values are calculated on the bottom nodes of the material in the as-received condition simulated with the punch speed of 10 SPM. In the early stage of the v-bending process, a stress sink forms at the center of the model where the plastic deformation is localized and acts as a plastic hinge inducing the fluting in the v-bending process. It broadens up to 30 mm from the center along the curve. Because of this fluting at the center, stress and strain peaks are then generated by the contact between the punch and the material as described in Fig.2.10c, which induce the deflection points in the deformed shape. This unique stress profiles over time were not found in Trzepiecinski and Lemu (2017) because the material model without considering YPP was used.

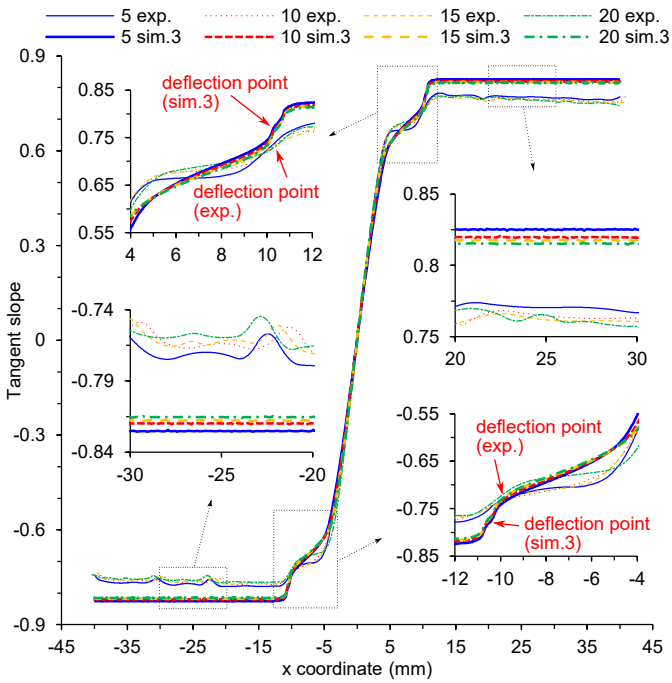

Figure 5.8. Comparison between the predicted and experimental tangent slopes in the as-received condition.

The reduction of the fluting by the roller-leveling process

In order to investigate the effect of the roller-leveling process on the fluting in the v-bending process, we performed the roller-leveling simulations with five PF conditions and the subsequent v-bending simulations at the punch speed of 10 SPM. Unless specified, the parameter set sim.3 is used by default in these simulations.

The roller-leveled specimens are looked into first. Fig.5.10a shows the effective plastic strain profiles in the target instance of FE models after the roller-leveling simulation. They are calculated on the bottom nodes of the model. The amount of induced effective plastic strain increases naturally with the PF condition. It is observed that the effective plastic strain fluctuates in the target instance and their fluctuation amount seems non-monotonically changing with respect to the PF condition. It is presumed that it might be somehow related to the surface profile measured experimentally for

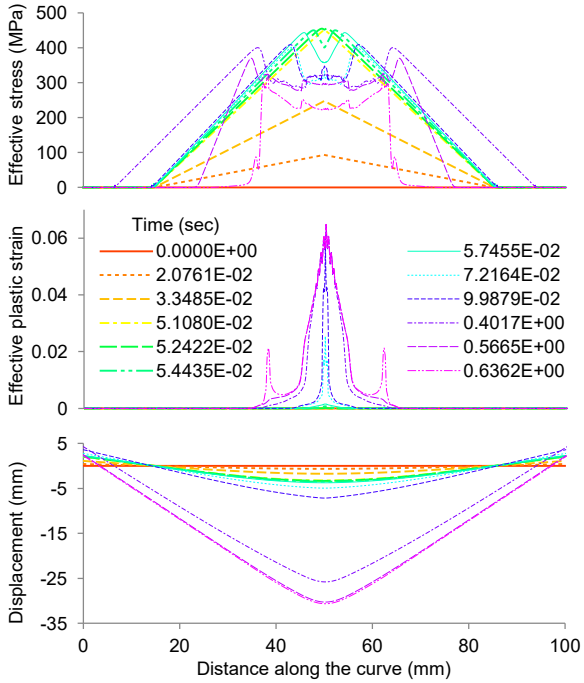

Figure 5.9. Time evolution of the effective stress, effective plastic strain and the displacement profiles along the curve during the v-bending simulation. They are calculated on the bottom nodes of the material in the as-received condition simulated with the punch speed of 10 SPM.

the roller-leveled specimens as shown in Fig.2.7. Hence, the roughness values (Ra and Rq) of effective plastic strain profiles are computed in the central 50 mm of the target instance and compared them with the surface roughness values obtained from the 3-D surface measurements as depicted in Fig.5.10. Interestingly, the plastic strain roughness shows a quite similar trend overall to the surface roughness in that it decreases initially and then increases with the PF. There exists a discrepancy in the PF values at the valley point, but it might be due to the difference between 2-D and 3-D characterizations and the coarseness of FE mesh. Also, it is possible that the induced plastic strains in experiments are smaller than the expected ones from the PF condition because of, for example, the slip between the specimen and rollers, the deformation of rollers,

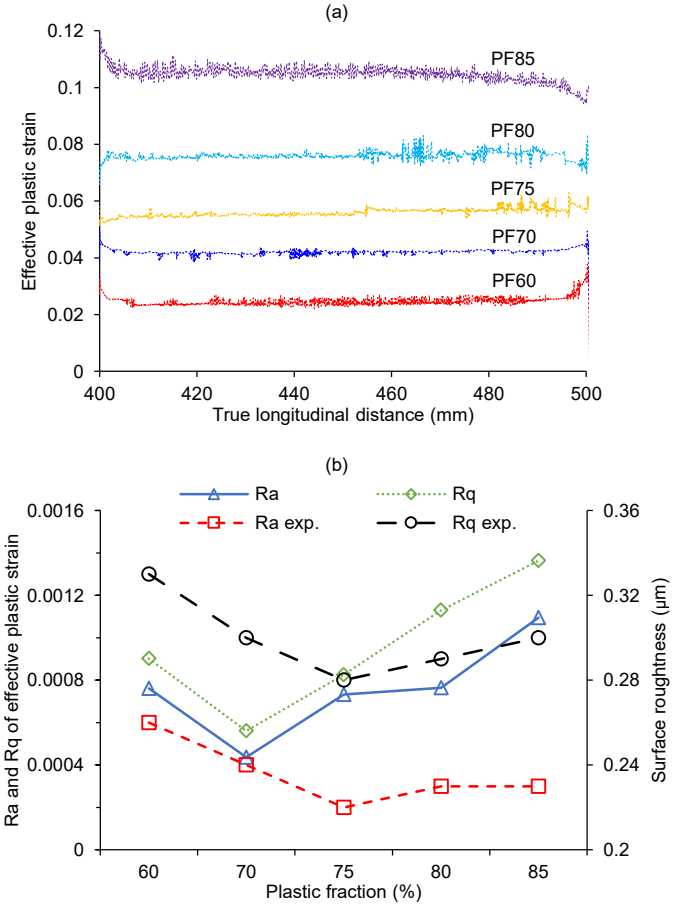

Figure 5.10. Effective plastic strains in the specimen after the roller-leveling simulation: (a) effective plastic strain profiles in the target instance and (b) their roughness values (Ra and Rq) compared to the experimental surface roughness values.

and the dynamic effects. With this in mind, the roughness of effective plastic strain profiles might be useful in estimating the surface roughness of a specimen after the roller-leveling process.

The gradient of effective plastic strains in the thickness direction increases with the PF as expected. Fig.5.11 displays the through-the-thickness profile of mean effective plastic strains that are calculated by averaging nodal strain values in the central 50 mm of the target region for each thickness layer. Slightly negative values can be treated as

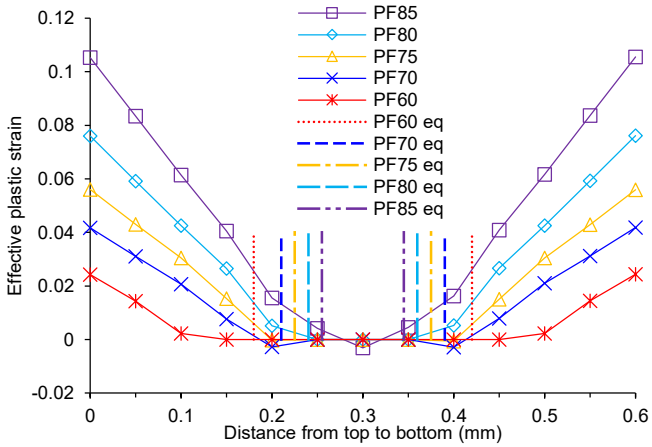

Figure 5.11. Through-the-thickness profiles of effective plastic strains. Each point represents the mean effective plastic strain computed by averaging nodal strain values in the central 50 mm of the target instance for the corresponding thickness layer.

zero because they appear when extrapolated from the values at integration points. The vertical lines represent the theoretical elastoplastic boundaries according to Eq.(2.2) so that the inside of which can be assumed as an elastic region. Overall, the elastic regions estimated from the through-the-thickness profile of mean effective plastic strains agree well with theoretical ones. Nevertheless, the predicted elastic regions for 60 to 75% PF conditions are wider while those for 80 to 85% PF conditions are narrower than the corresponding theoretical regions.

The v-bending simulations for materials roller-leveled with five PF conditions are then conducted at the punch speed of 10 SPM. Fig.5.12 shows the final deformed shapes predicted using the parameter set sim.3 along with the experimentally measured ones. The experimental curve corresponding to each PF condition is selected from three experimental data conducted in the same condition. The predicted curves are translated to the experimental ones so that their bottom points are matched. The as-received curves in this figure are the same as the curves at the punch speed of 10 SPM in Fig.5.6. The overall trend of the shape change with respect to the PF condition in simulations is similar to experiments, but the predicted deformed shape itself at each condition

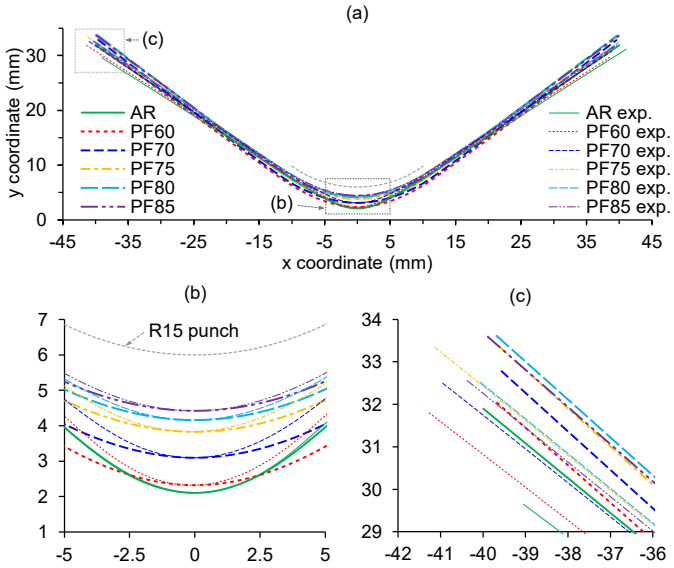

Figure 5.12. Results of the v-bending simulations for materials roller-leveled with five PF conditions: (a) deformed shapes and (b)-(c) close-up views of the deformed shape.

deviates from the experimental one. In particular, even for the material roller-leveled with the lowest PF condition, the fluting is already weakened significantly unlike experiments where strong fluting is still observed at lower PF conditions.

Variations in the bending angle and the radius of curvature quantified from the experimental and simulated curves clearly show this discrepancy as shown in Fig.5.13. The predicted bending angle decreases with the PF and becomes saturated around 75% condition similar to experiments. As in the as-received condition, there exists the angle difference of four to seven degrees between the experiment and the simulation. On the other hand, the radius of curvature in simulations increases with the PF as in experiments. However, unlike in the as-received condition, the predicted radii of curvature differ from the experimental ones by about 3.5 to 6.3 mm. Notably, the radii of curvature predicted for higher PF conditions reach almost the punch radius of 15 mm whereas the largest radius obtained experimentally with 85% PF condition was only around 11 mm. The present simulation predicts this value already at 60% PF condition.

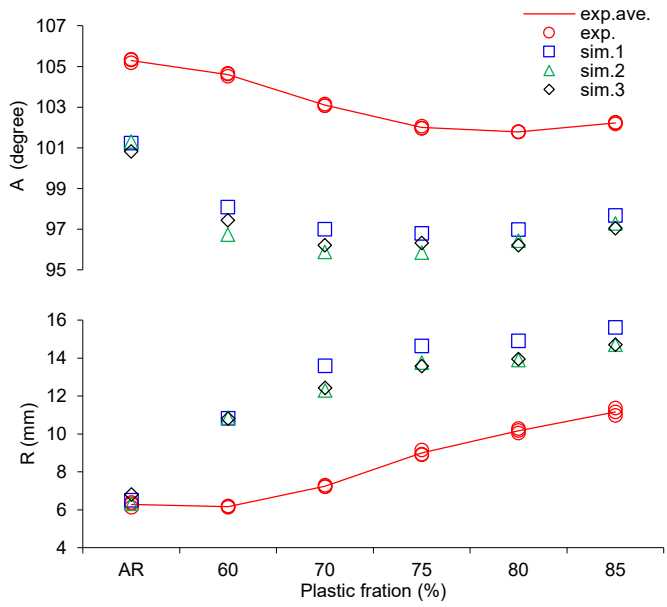

Figure 5.13. Comparison between the predicted and experimental R and A values for materials roller-leveled with five PF conditions.

As a result, the deflection points do not appear in these simulations since the fluting hardly occurs as shown in Fig.5.14, leading to a rather gradual change of tangent slopes without a flat region and sudden increase.

It can be presumed that this considerable difference in the radius of curvature for roller-leveled materials might be because the imposed plastic strains in the actual roller-leveling process are probably much smaller than the expected ones from the PF condition. And also because the predicted radii of curvature in the as-received condition agree reasonably well with the experimental ones at various punch speeds. To test this hypothesis, additional v-bending simulations are conducted with even lower PF conditions of 40% and 50%. In Fig.5.15 and 5.16, the simulation results for 40%, 50% and 60% PF conditions are compared with the experimental results for 65%, 75% and 85% PF conditions, respectively. The experimental result of 65% PF condition is estimated by averaging the results of 60% and 70% PF conditions. As shown in Fig.5.15, the predicted radii of curvature are well matched with the experimental values

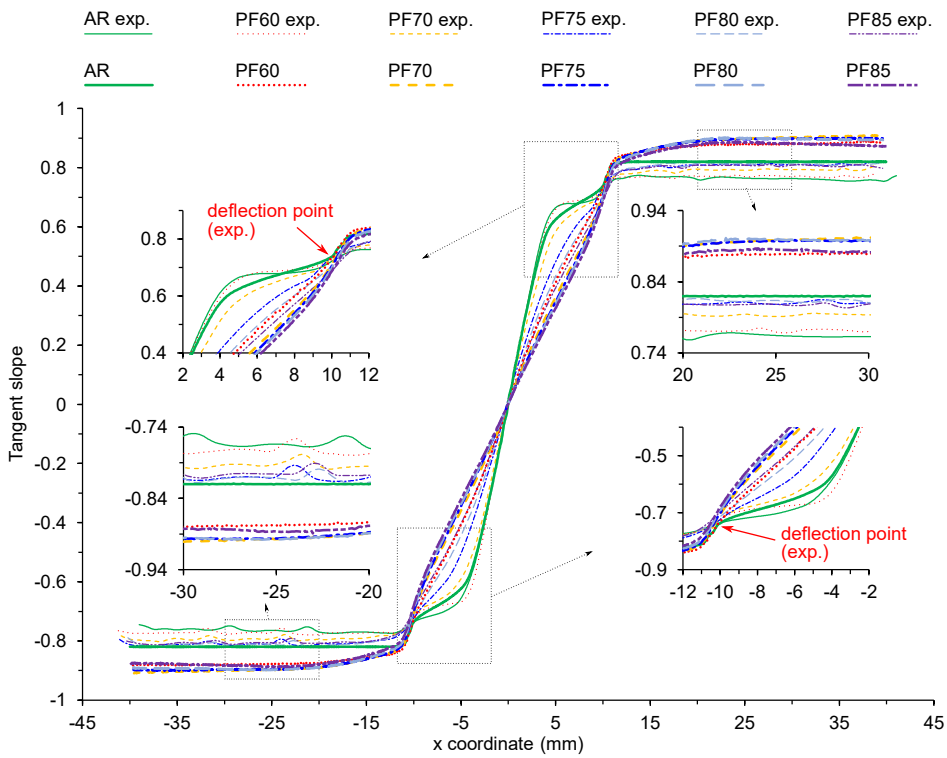

Figure 5.14. Comparison between the predicted and experimental tangent slopes for materials roller-leveled with five PF conditions.

while the bending angles show a difference of about four degrees which exists for the simulations even in the as-received condition. Tangent slope analysis in Fig.5.16, which predicts the emergence of the deflection points as in experiments, supports the present hypothesis as well. Therefore, it is reasonable to think that plastic strains smaller than the ones predicted theoretically or computationally are likely to be induced in the actual roller-leveling process. Because there could be unconsidered physical reasons in the model including the slip between the material and the rollers, the dynamic effects, and the side slipping of the material.

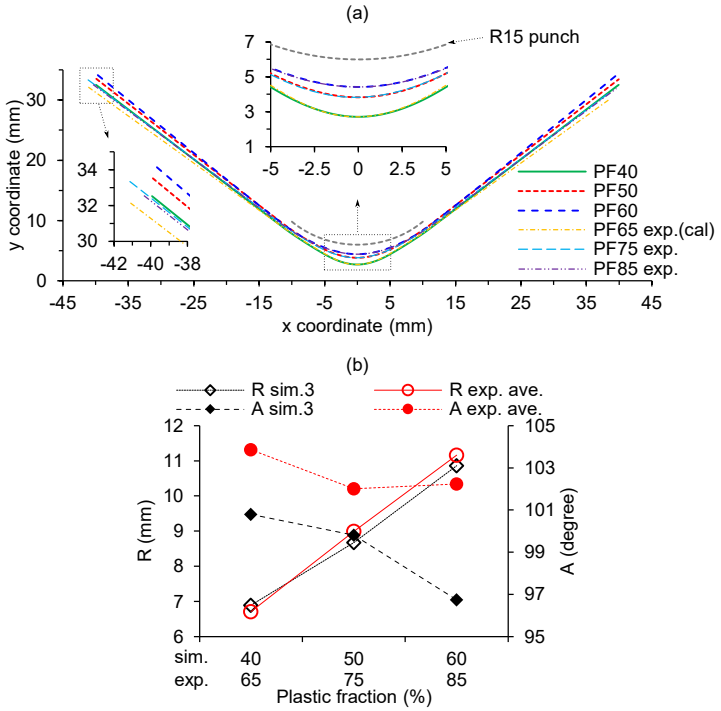

Figure 5.15. Comparison between the predicted (40-60% PF conditions) and experimental (65-85% PF conditions) results in the v-bending process: (a) deformed shapes, (b) R and A. The experimental result for 65% PF condition is obtained by averaging the result for 60% and 70% PF conditions.

5.2 Numerical simulations of static dent resistance considering BH behavior for 490DP

5.2.1 Uniaxial tension and tension-compression simulations

Uniaxial tension and tension-compression simulations for 490DP including BH step use FE models shown in Fig.5.17. These models have a few different dimensions from Fig.4.4, those are the radius of specimen shoulder in uniaxial tension, the gauge length in uniaxial tension-compression, and the thickness of both models. The hexahedral elements construct the FE models are C3D20RT (20-node triquadratic displacement,

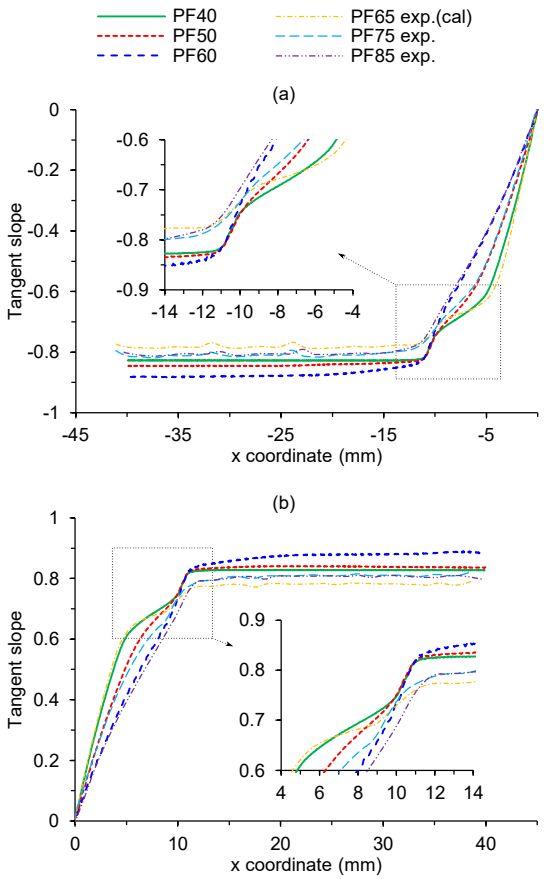

Figure 5.16. Tangent slopes of deformed shapes in Fig.5.15 when x coordinate is (a) negative and (b) positive.

trilinear temperature, and reduced integration) for the *Coupled temp-displacement* analysis. Among the total of 3,040 elements of the uniaxial tension FE model, 1,600 elements of size 0.625 mm x 0.625 mm x 0.7 mm are located in the gauge section. In the uniaxial tension-compression model of the total of 768 elements, 768 elements of size 0.625 mm x 0.625 mm x 0.35 mm occupy the gauge section. The FE models have a single layer of elements in the thickness direction. To avoid the buckling instability, the FE model of the uniaxial tension-compression has symmetric boundary conditions in the thickness direction. The stress-strain responses are obtained by the strain evaluated from the relative displacements between measuring points and the stress calculated

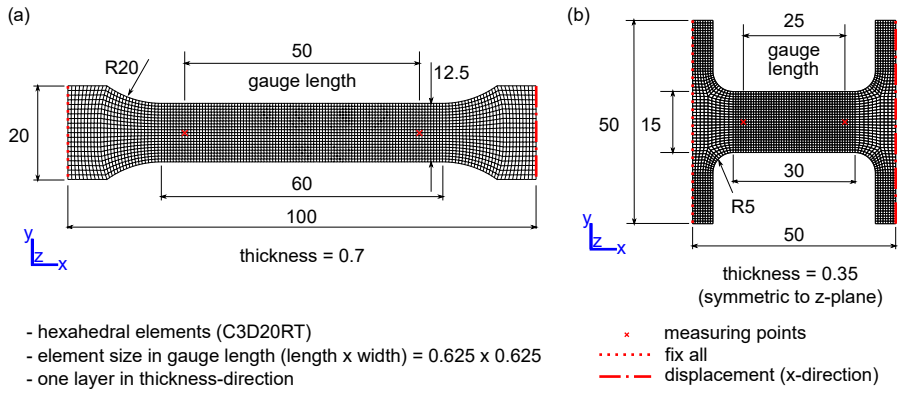

Figure 5.17. FE models for uniaxial simulations with BH operation (dimensions in mm): (a) uniaxial tension and (b) uniaxial tension-compression.

from the reaction force of the fixed end.

The other simulation conditions, steps, cases are also analogous to the single element BH simulation in Chapter 4. The simulations consist of 4 steps as follows:

- Step-1: Uniaxial tension (t_{Step-1} sec).
- Step-2: Unloading (1 sec).
- Step-3: Bake hardening (BH time + 1,200 sec).
- Step-4: Uniaxial tension or compression (t_{Step-4} sec).

In the Step-1, the displacement boundary condition is 5 mm and 2.5 mm for the uniaxial tension and the uniaxial tension-compression, respectively. Then, t_{Step-1} can be set so as to meet the crosshead speed of 6 mm/min. The *Predefined fields* with an initial temperature of 20 °C is used in this step. The Step-2 can be started from a certain time increment of the Step-1 in order to meet the pre-strain condition. For this, the *Restart* feature is used in the Step-1 and the *Predefined fields* with the initial state, the certain increment of the Step-1, is defined in the Step-2. This analysis continuation technique is necessary because, not like the single element simulations, these multiple elements of an experimental specimen shape are unable to directly acquire strain information by the

displacement boundary condition before executing the simulations. In the Step-2, only the fixed boundary condition remains for unloading. The boundary conditions for the Step-3 take the temperature history shows in Fig.2.15. These temperature conditions are applied to all nodes of the FE models. The last step can be uniaxial tension or uniaxial compression with t_{Step-4} calculated from the remaining displacement and the crosshead speed.

The simulations use the same cases of Table 2.2. The material constants are chosen to well reflect the experimental results of uniaxial tension and tension-compression. Those are listed in Table 4.3. Note that Eq.(3.13) and the condition of $Y_{w0} = Y_{wa}$ (similar to the sim.1 set of Table 5.2) are used for the material parameter Y_w. The mechanical and thermal constants for *Coupled temp-displacement* analysis are the same as those of the single element BH simulations. The simulations also start with $\bar{\varepsilon}_0 = 0.02$ considering no initial YPP of the material.

Firstly, Fig.5.18 shows stress-strain responses extracted from the unaxial tension simulation cases 'T only' at the crosshead speed of 0.6, 6, and 30 mm/min with the corresponding experimental responses. The yield points and the strain hardening regions

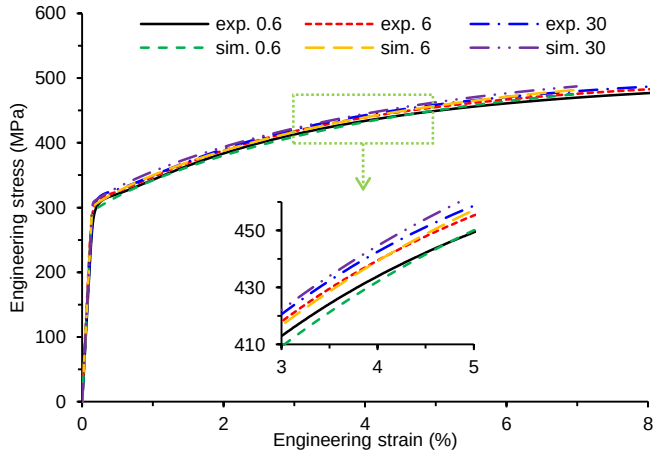

Figure 5.18. Stress-strain responses of the simulation cases 'T only' at the crosshead speed of 0.6, 6 and 30 mm/min with the corresponding experimental responses.

of the experimental curves are fittingly described by the simulation results. The rate dependency of the material is also properly mimicked by using the rate exponent n_e set to 30 in the simulations.

The stress-strain curves of 'T-U-BH-T' cases according to BH temperature are plotted in Fig.5.19. In this figure, it is identified that the experimental BH behaviors

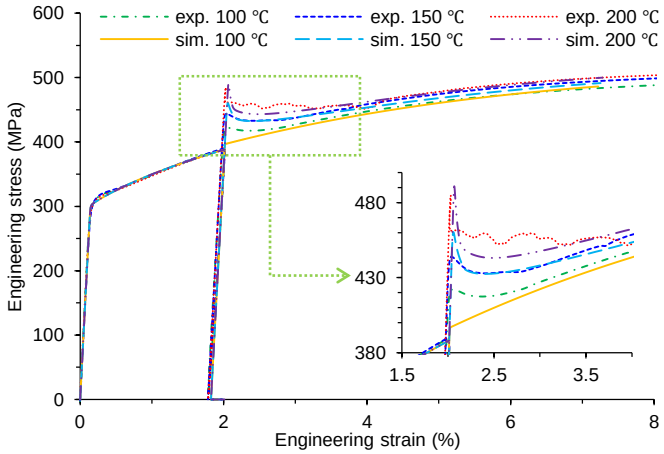

Figure 5.19. Stress-strain responses of the simulation cases 'T-U-BH-T' with BH temperature of 100, 150, and 200 °C for BH time of 20 min and pre-strain of 2%.

are overall illustrated by the simulations. In detail, however, the simulation curve of 200 °C BH temperature does not exhibit the experimental instability of the yield-point elongation. The reason for no instability in the yield-point elongation region of this simulation curve might be due to a relatively small difference (about 50 MPa) between the upper yield point and the lower yield point in the single element simulation of the same BH condition as depicted in Fig.4.13. In the previous simulations, as shown in Fig.5.2a, the yield-point elongation instability is realized in simulations, and the difference between the upper yield point and the lower yield point in the sim.1 case of Fig.5.1 is over 85 MPa. The next unsatisfied aspect is that the simulation curve of 100 °C BH temperature does not have the upper yield point. This could be originated from that the present material model and its BH parameters have some limitations to

describe BH effects in this temperature of 100 °C.

Next graphs are the stress-strain responses of 'T-U-BH-T' cases according to BH time as drawn in Fig.5.20-5.21. With the BH temperature of 100 °C, the simulation

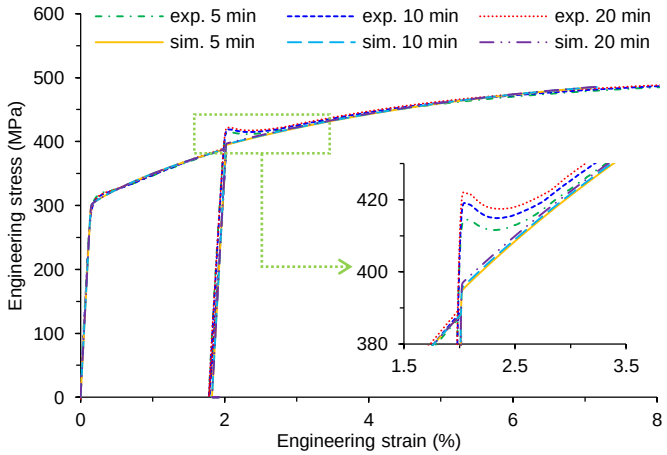

Figure 5.20. Stress-strain responses of the simulation cases 'T-U-BH-T' for BH time of 5, 10, and 20 min at BH temperature of 100 °C and pre-strain of 2%.

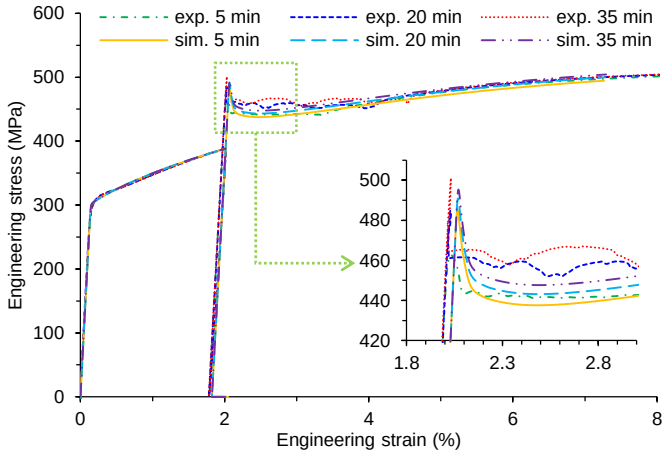

Figure 5.21. Stress-strain responses of the simulation cases 'T-U-BH-T' for BH time of 5, 20, and 35 min at BH temperature of 200 °C and pre-strain of 2%.

responses do not reveal the YPP that is weakly shown in the experimental curves as

plotted in Fig.5.20. The stress level in the simulation responses is slightly different according to the BH time, and the magnitude of the difference is smaller than the experimental result. In Fig.5.21 with the BH temperature of 200 °C, all experimental curves clearly show the yield-point elongation instability whereas simulations curves do not display it presumably due to the similar reason explained in Fig.5.19. The experimental variation of the upper and lower yield point according to BH time is roughly described by the simulations. The experimental stress level in the strain hardening region is relatively narrower than the simulated one. This might be because the present material model considers the precipitation hardening effects, and the term σ_{prec} in Eq.(3.26) associated with these effects makes the difference according to BH time in these simulation cases.

The last stress-strain responses of 'T-U-BH-T' simulation cases are with respect to the pre-strain of 2, 3, and 4% as plotted in Fig.5.22. In these simulations cases, the

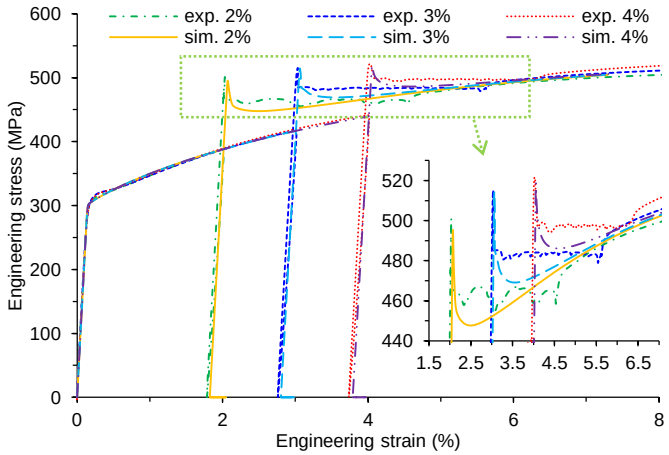

Figure 5.22. Stress-strain responses of the simulation cases 'T-U-BH-T' with pre-strain of 2, 3, and 4%. The BH temperature and time are 200 °C and 20 min, respectively.

experimental instabilities in the yield-point elongation are not captured, and the lower yield stresses are lower than the experiments. However, the upper yield stress levels are similarly depicted. The simulation curves in the strain hardening region are very close

to each other while the experimental ones show some difference.

For the uniaxial tension-compression simulations, the stress-strain responses of 'T-C' and 'T-U-BH-C' are plotted with the experimental curves in Fig.5.23-5.24. In

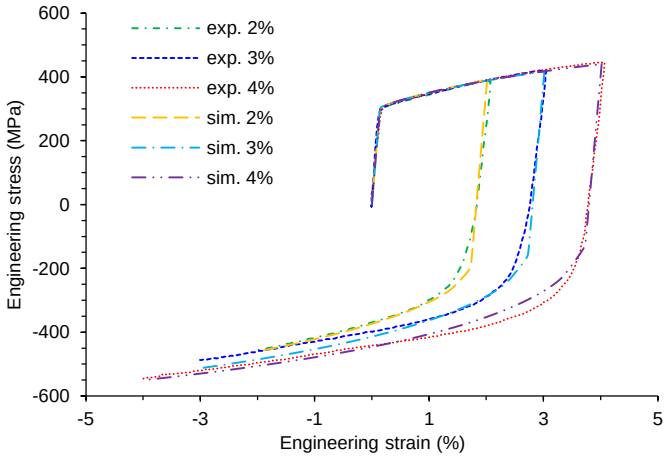

Figure 5.23. Stress-strain responses of the simulation cases 'T-C' with pre-strain of 2, 3, and 4%.

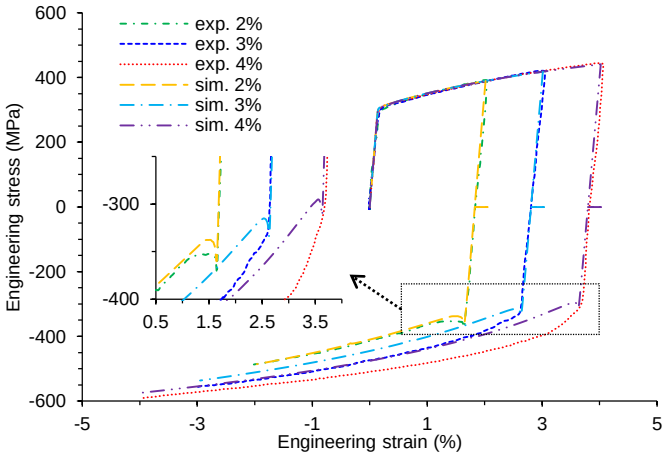

Figure 5.24. Stress-strain responses of the simulation cases 'T-U-BH-C' with pre-strain of 2, 3, and 4%. The BH temperature and BH time are 200 °C and 35 min, respectively.

the simulation cases 'T-C', the Bauschinger effects observed in the experiments are

partially well described. Only the compressive yield stress with the pre-strain of 4% is comparable, and its gap between the experiments and the simulations increases as the pre-strain reduces. The stress levels in the compression region show in the other way; the stress difference in the strain hardening region increases as the pre-strain increases. This seems to be caused by a limitation of the kinematic hardening rule the present material model takes. The simulation cases 'T-U-BH-C' also show similar results. The simulation case with the pre-strain of 2% quite well fits the experimental curve however the other cases cannot describe the disappearance of YPP in the experiments. If Y_w varies as the effective plastic strain increases ($Y_{w0} \neq Y_{wa}$), the experimental compressive responses after BH might be described. If then, however, the compressive yield stress can be increased so that its current difference between the experiments and simulations can be also increased.

5.2.2 Static dent simulations

Static dent simulations for 490DP corresponding to the static dent experiments are carried out using the axisymmetric FE models displayed in Fig.5.25. The element type and size for the blank of these models are thermally coupled CAX8RT (8-node axisymmetric, quadrilateral displacement, bilinear temperature, and reduced integration) and 0.175 mm x 0.175 mm, respectively. The blank FE model has total a 3,272 of elements composing four layers in the thickness direction. Axisymmetric discrete rigid elements RAX2 of 0.1 mm are used for all tools including the indenter. The holder shown in Fig.5.25a is the same as the one in Fig.5.25b, and its positions in the x-direction are also identical in both models. Therefore, the blank is fixed at the same position in the x-direction which is the stinger bead position (=the holder lock position).

The contact conditions of these simulations are determined analogously to the roller-leveling and v-bending simulations. The contact discretization method between the blank and the tools is surface-to-surface with the finite sliding tracking approach. For tangential behavior, the penalty method is chosen with a friction coefficient of 0.15.

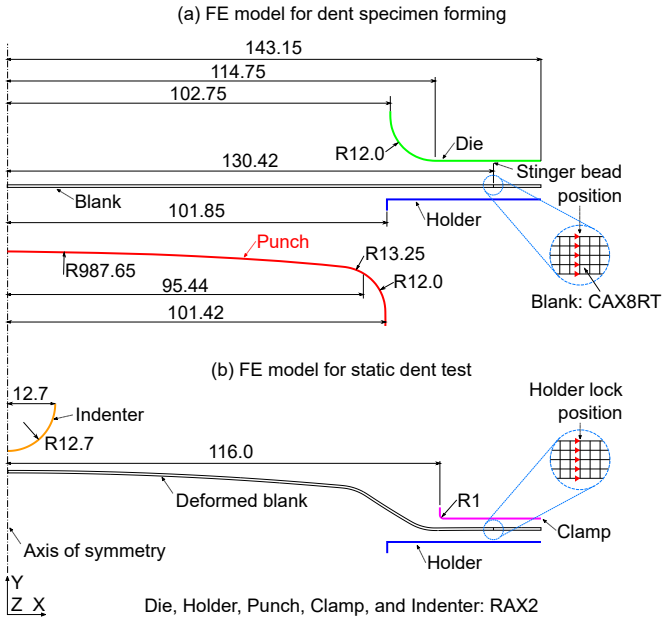

Figure 5.25. FE models for (a) dent specimen forming and (b) dent test.

In order to avoid contact instability, the exponential pressure-overclosure relationship, so called 'softened contact', in normal behaviors is employed with the contact pressure of 30 MPa at zero clearance and the clearance of 0.0001 mm at zero contact pressure. The accuracy of this softened contact condition may be referred to Appendix A.2.

The simulation steps are composed as follows:

- Step-1: Dent specimen forming (5.333 sec).
- Step-2: Springback (1 sec).
- Step-3: BH (BH time + 1,200 sec).
- Step-4: Holder clamping for dent test (1 sec).
- Step-5: Dent - indenter 6 mm forward (180 sec).
- Step-6: Dent - indenter 6 mm backward (180 sec).

These steps are also shown in Fig.5.26. The first and second steps are simulating dent

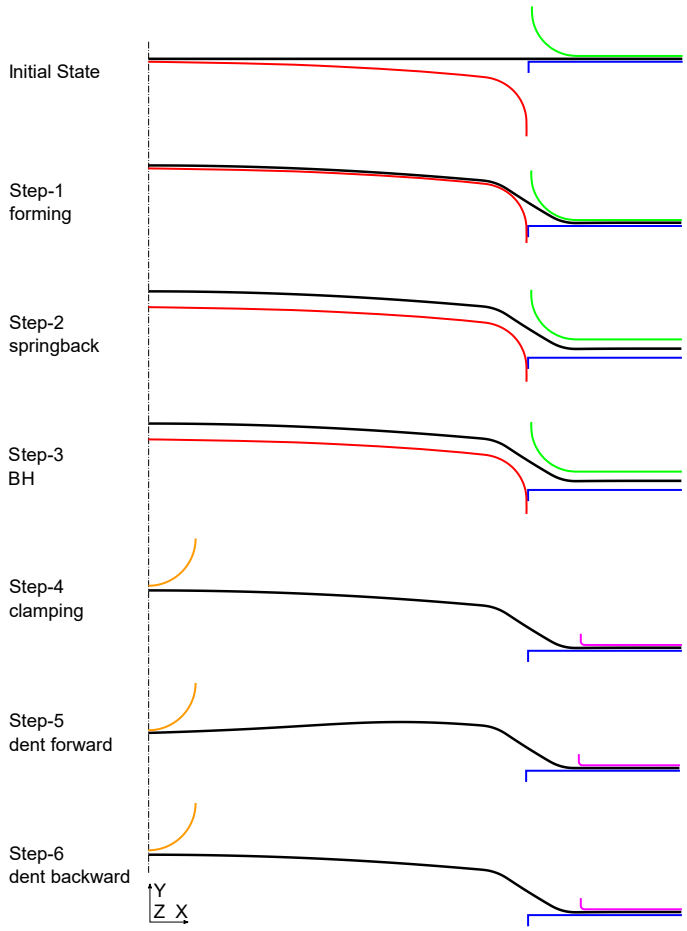

Figure 5.26. Simulation steps for dent specimen forming, BH, and dent. The figure for each step shows the last state within the step.

specimen forming and its springback. The Step-1 time (5.333 sec) is calculated from dividing the die stroke by the forming speed. The initial temperature for this step is 20 °C. The BH operation in the Step-3 takes the temperature history drawn in Fig.2.15. The BH conditions are the same as the experiments. For no BH condition, the Step-3 can be skipped. In the Step-4, the deformed specimen is clamped by the holder, and initial indenter position for the Step-5 is obtained. During the dent steps, the indenter moves forward by 6 mm and backward by 6 mm with a speed of 2 mm/min. The indenter force

can be obtained from the reaction force of the rigid elements composing the indenter.

In order to examine the influence of the elastic modulus degradation on the dent simulations, the sets of simulation parameters associated with the degradation are chosen as listed in Table 5.3. The sim.a set uses a constant elastic modulus, and the

Table 5.3. Simulation sets for the elastic modulus degradation.

	E_0 [GPa]	E_{sat} [GPa]	ξ_E	Remark
sim.a	212.9			constant
sim.b	212.9	161.5	51	degra. (uniaxial)
sim.c	212.9	183.5	119	degra. (biaxial)

other sets use the degradation rule of Eq.(2.4). The parameters of the sim.b set are the same as the present one in Table 2.3, and those of the sim.c set are assumed values by referring the biaxial modulus of 490DP in Lee et al. (2016).

The deformed shape (top layer) of the blank after simulating the Step-1 and 2 is drawn in Fig.5.27 with the averaged experimental data of Fig.2.29. The experimental

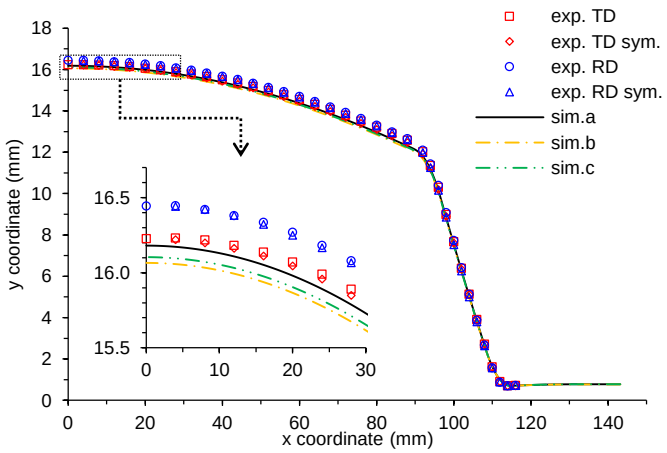

Figure 5.27. Deformed shape (top layer) obtained from the simulation Step-2 with the averaged experimental data symmetrized to the y axis.

data in the negative x coordinate in Fig.2.29 is symmetrized to the y axis. The simulation curves are shifted to the position in which their bottom points were matched

to the experimental data. The overall shapes of the simulations are fairly fitted to the experimental data whereas the top point springbacks of the simulations are bigger than those of the experiments. As expected from the general knowledge that springback increases as elastic modulus decreases, the order of the springback magnitude in the simulation sets is the sim.b set, the sim.c set, and the sim.a set.

The strain of the deformed top layer in the x-direction is extracted from the Step-2 result and plotted as in Fig.5.28. The experimental data in this figure is distributed

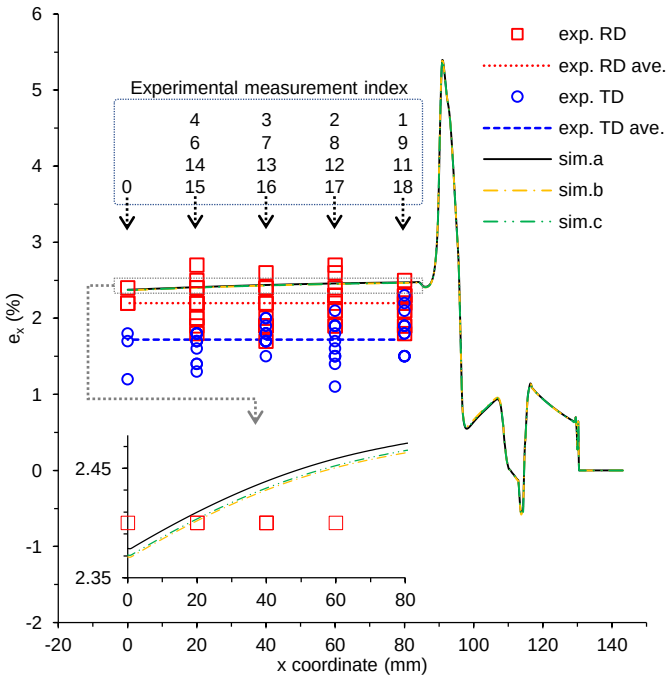

Figure 5.28. Top layer strain profiles obtained from the simulation Step-2 results in the x-direction along to x coordinate with the experimental strain measurement.

considering the measurement locations as shown in Fig.2.27b. The calculated strain results are not significantly different from the experimental data. However, they are not located inside the RD and TD average values. As expected, the maximum calculated strain of about 5.4% is observed around the end of the convex shape. The highest strain in the convex shape among the simulation sets is the sim.a set while the lowest

strain is the sim.b set despite that their difference is very small. The thicknesses of the deformed blank obtained from the Step-2 results in the x-direction are shown in Fig.5.29. The experimental data of this figure is the same as those of Fig.2.28. The

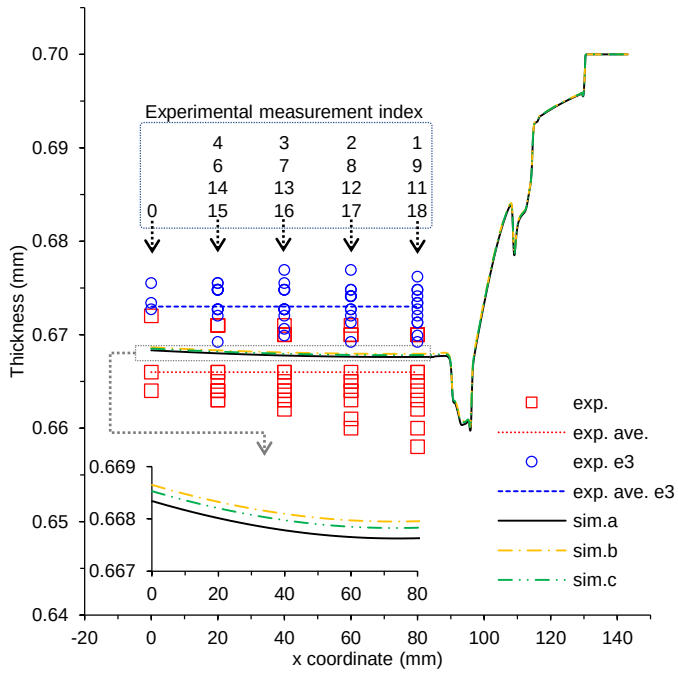

Figure 5.29. Thickness profiles obtained from the simulation Step-2 results in the x-direction along to x coordinate with the experimental thickness measurement.

simulation thicknesses are closer to the ultrasonic gauge measurement result than the calculated values from e_3. The order of the thickness profiles in the simulations is the opposite to the strain profiles as anticipated. The minimum thickness is about 0.660 mm, and its location is the same as the maximum strain point in Fig.5.28.

The force-displacement simulation responses without BH operation are drawn with the corresponding averaged experimental result. The experimental response is from Fig.2.32. Since the initial slope of the sim.a set curve is the highest among the simulation sets, the highest force is maintained during the forward movement of the indenter, and its maximum force is also the highest. The shape of its unloading curve

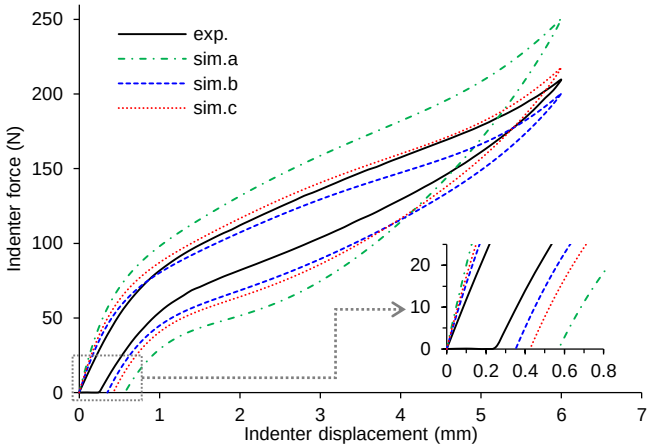

Figure 5.30. Force-displacement simulation and averaged experimental responses without BH operation.

is quite different from the experimental one, and its dent depth is recorded more than twice as high as the experiment. The possible reason for this might be that the sim.a set uses a constant and highest elastic modulus. The other sets that use the degradation rule get closer to the experimental data. These results show that the degradation of elastic modulus can be a important factor for this kind of dent simulations as explained in Lee et al. (2016). However, these degradation sets are not able to fully meet both the dent depth and the maximum force of the experiments.

The simulation results with the experimental curves according to the BH temperature are plotted in Fig.5.31. The experimental curves are the same as Fig.2.32. Analogously to Fig.5.30, the initial slopes of the sim.a set curves in Fig.5.31a are the steepest among the simulation sets. This set also leads to the highest maximum forces and the biggest dent depths among the simulation sets being the farthest away from the experimental curves. In Fig.5.31b-c, the simulation sets which use the elastic degradation rule have closer slopes to those of the experiments. Nonetheless, the sim.b set starts with a similar slope to the experiments, this set records the lowest maximum force showing some difference from the experiments. However, the dent depths of the sim.b

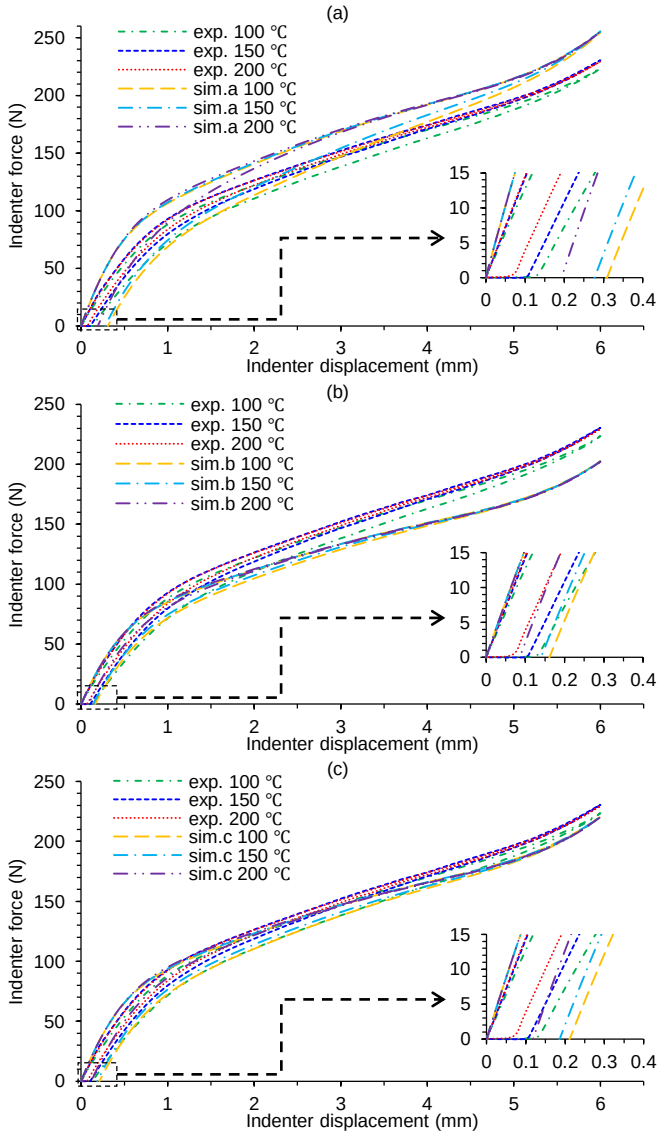

Figure 5.31. Force-displacement simulation responses according to the BH temperature with the experimental responses: (a) sim.a, (b) sim.b, and (c) sim.c. The BH time is 20 min.

set are the closest to the experiments among the simulation sets. Fig.5.31c illustrates the medium level results between the Fig.5.31a and b. Despite these inaccuracies, the simulations are able to describe the behavior that the depths are reduced as the BH

temperature increases.

The next two sets of results, Fig.5.32 and Fig.5.33, are the simulation results according to the BH time for the BH temperature of 100 and 200 °C, respectively. The experimental curves for these graphs are from Fig.2.33-2.34. In Fig.5.32, although the force-displacement responses of the experiments are different from each other according to the BH time, those of the simulations are almost identical to each other due to the insensitivity of the present material model and its parameter set around the BH temperature of 100 °C. The experimental dent depth level is fairly predicted in the sim.b set whereas the experimental maximum force level is well estimated by the sim.c set. In Fig.5.33, not like Fig.5.32, the simulation curves on the backward movement vary with respect to the BH time while those on the forward movement are hardly distinguishable. These simulation responses do not seem to fully describe the experimental responses according to the BH time. However, the experimental dent depths and the maximum forces are roughly forecast by the sim.b set and the sim.c set, respectively. All results from Fig.5.30-5.33 are plotted in Fig.5.34-5.35 in terms of the maximum force and the dent depth. In Fig.5.34, the maximum force level in the experiments is approximately predicted by the sim.c set notwithstanding the scattered experimental data. In Fig.5.35, the experimental dent depth with respect to the BH conditions is adequately predicted by the sim.b set.

5.3 Summary

In this chapter, comprehensive and in-depth numerical investigations for the fluting defect of PLCS in the v-bending and its reduction by the roller-leveling were conducted, and extensive simulation works for the BH behavior of 490DP were synthetically handled with uniaxial loads and static dent cases. The material model developed in the present study could effectively reproduce the uniaxial tension and cyclic behaviors of PLCS after determining the material parameters to fit the uniaxial experiments.

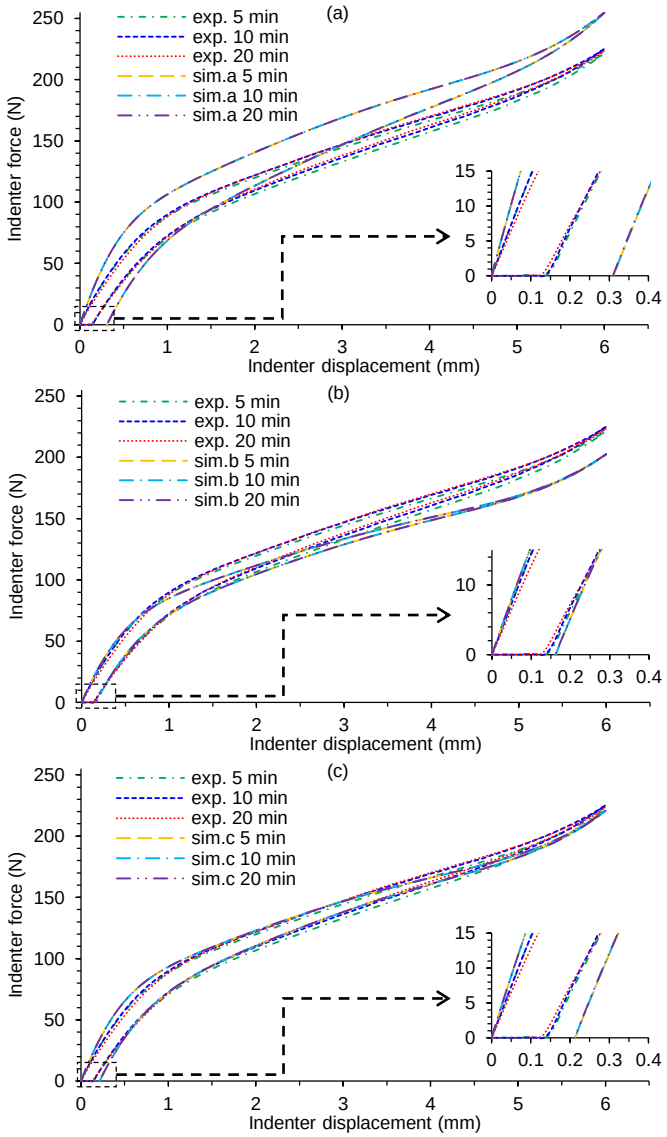

Figure 5.32. Force-displacement simulation responses according to the BH time with the experimental responses: (a) sim.a, (b) sim.b, and (c) sim.c. The BH temperature is 100 °C.

V-bending simulations of PLCS in the as-received condition with this model could predict the fluting-related features fairly well including the radii of curvature and the deflection points. They clearly showed how the fluting defect affected the deformed

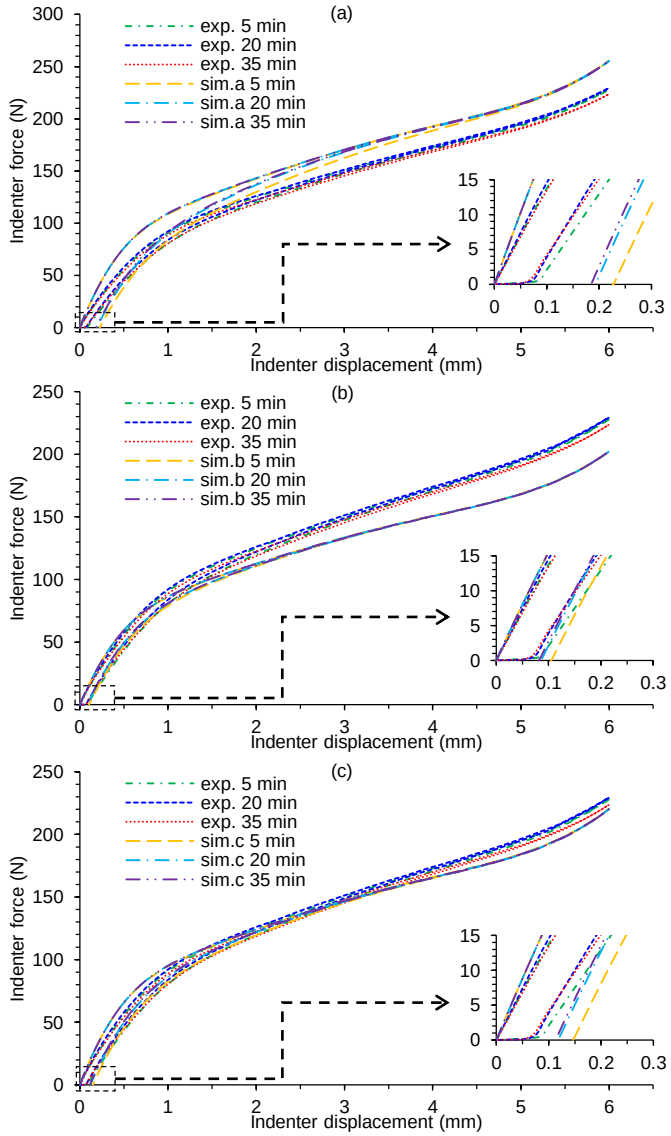

Figure 5.33. Force-displacement simulation responses according to the BH time with the experimental responses: (a) sim.a, (b) sim.b, and (c) sim.c. The BH temperature is 200 °C.

shape of specimens with the YPP. In the simulations, the stress sink first developed from the YPP at the center which operated as a plastic hinge and then the plastic deformation was localized near the contact point between the punch and the specimen

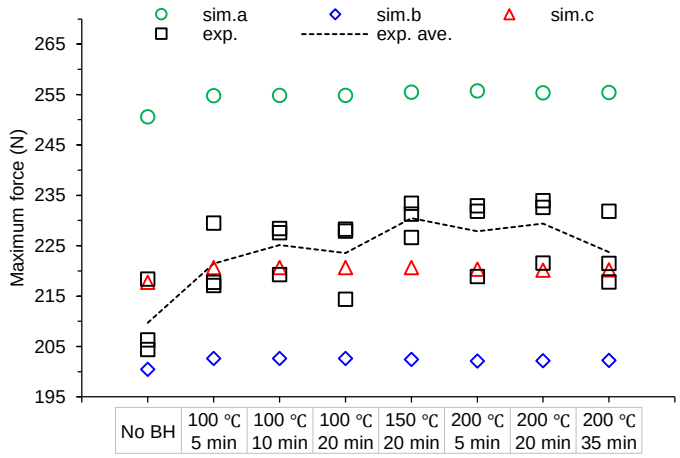

Figure 5.34. Maximum forces in the simulations according to BH condition.

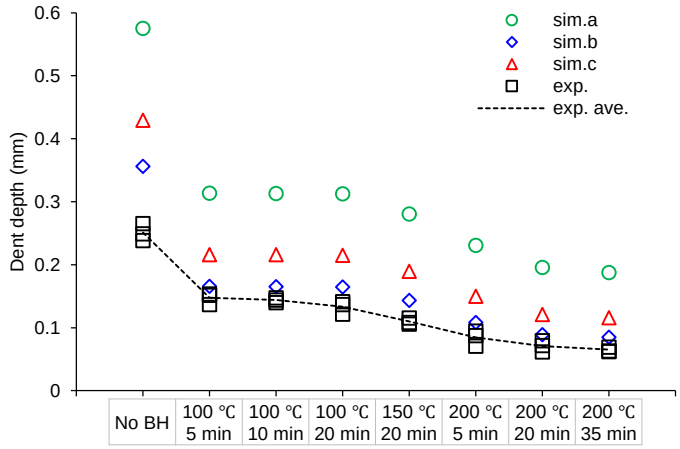

Figure 5.35. Dent depths in the simulations according to BH condition.

forming the deflection points. Roller-leveling simulations could also capture the overall trend of experimental results well. However, the predicted values at various roller-leveling conditions showed some deviations from the experimentally measured ones. We found that simulated results became well matched with experimental ones if we used a lower leveling condition in simulation than the one estimated from the analytical expression for the experimental roller-leveling condition. This suggests that the actual roller-leveling condition might be lighter than expected due to some losses during the

process. Or, the present FE analysis might impose a higher leveling condition since the simulations worked well in other cases.

The FE simulations including BH steps for the corresponding experiments of 490DP brought some insights for predicting the BH behavior in the experiments with the present material model which combines the YPP model and the BH model. The material parameters for 490DP were determined to fit the uniaxial load cases with BH. In the uniaxial tension cases, the simulation responses according to various BH conditions overall described the experiments except for the yield-point elongations. The compressive responses before and after BH operation in the uniaxial tension-compression cases were partially illustrated presumably owing to the limitation of the present kinematic hardening rule. Static dent simulations including forming simulations were able to roughly depict the experiments. Plastic strains and thickness obtained in the simulations were comparable to the test values. Static dent resistance calculated in the simulations was also commensurate with the experimental results more obviously when the degradation of the elastic modulus was taken into consideration.

Chapter 6

Conclusion

In this thesis, we firstly investigated the YPP of PLCS and the BH behavior of 490DP in the comprehensive experiments. Specifically, the fluting defect of PLCS in the v-bending, the defect reduction by roller-leveling, and the dent resistance of bake hardened 490DP were investigated after examining the YPP of PLCS and the BH behavior of 490DP in the uniaxial loads. Secondly, the material modeling was carried out to reflect all experimental observations. In the material modeling, the robust stress integration algorithms were newly proposed for conducting implicit elastoviscoplastic FE analysis for YPP materials. These robust algorithms were applied to the present material modeling based on the Yoshida-2008 model. The BH model was also combined with the YPP model in order to encompass the ambilaterality of the YPP, avoiding or utilizing it. Lastly, numerical analysis was performed to illustrate the fluting defect of PLCS with its reduction and the dent resistance of 490DP using the YPP and BH integrated model. While these objectives were being achieved, the following key outcomes were drawn:

1. The fluting defect of PLCS in the v-bending and its reduction by the roller-leveling process were embracively and intensively studied in the experiments. After observing the rate dependency of the YPP and its cyclic behaviors for PLCS in the uniaxial experiments, the roller-leveling tests were performed with

five PF conditions. It would be beneficial to assess the surface roughness of the material processed with the PF conditions to determine the proper PF condition without leading to surficial defects. Although the YPP values of roller-leveled specimens decreased in general as induced plastic strains increased, they were slightly more strengthened in the 60% PF condition than the as-received condition presumably due to the dominant effect of residual stress reduction over the plastic strain addition in a low PF condition. The v-bending tests for the as-received and the roller-leveled materials demonstrated that the fluting, much smaller radii of curvature compared with the punch radius, occurred, this fluting additionally generated the deflection point, and as the YPP properties were reduced by the roller-leveling, these fluting-related features disappeared. The BH behavior of DP steel was synthetically studied in the experiments of uniaxial loads and static dent cases. In the uniaxial tension tests, the responses with respect to the BH temperature exhibited a more obvious difference than those with respect to the BH time. The degradation of the elastic modulus according to the pre-strain identified in the uniaxial tension tests was similar to the previous literature regardless of BH conditions. With the fixed BH condition in the uniaxial tension-compression tests, only the pre-strain of a 2% case gave clear YPP in the compression after BH. In the static dent experiments, as the BH conditions got stronger, there was no clear tendency in the maximum dent force while there was an apparent reduction in the dent depth. The BH effect on the dent resistance was more explicitly observed in the BH temperature variations than the BH time.

2. The material modeling for describing the YPP with the BH behavior was newly presented with their coupling scheme. Based on the Yoshida-2008 model, simple kinematic hardening rules and the true yield-point behavior were adopted and considered, respectively. Non-convergent characteristics of YPP constitutive equations were conquered by proposing the robust stress integration algorithms that adopt the bisection method and/or the two-point Newton method. A phe-

nomenological BH model was taken into account for the material model to mimic the formation of the Cottrell atmosphere and the precipitation hardening. The YPP material model in combination with the BH calculation portion was implemented with the proposed robust algorithms. This model was validated to check its robustness in solving YPP-related non-convergent problems showing its effectiveness in performing the YPP-related simulations than the conventional approach. Whereas these algorithms may require longer computational times. The BH part of the material model was also verified using the single element simulations delivering a possibility that the present material model can be utilized in predicting the BH potential of bake hardenable material.

3. The extensive experimental results were able to be effectively reproduced by the numerical simulations using the material model developed in the present study and the material parameter sets determined to fit the uniaxial load experiments. The material parameter set for the true yield-point behavior was suitable to describe the YPP in the uniaxial simulations of PLCS, while the other simulations showed different results. In the roller-leveling simulations for PLCS, it might be worth to utilize the effective plastic strain fluctuation to assess the experimental surface roughness with respect to the PF conditions. The v-bending simulations for the as-received PLCS could describe the fluting-related features fairly well providing the insights of the fluting mechanism which the stress sink acts as the plastic hinge. The roller-leveling simulations could also depict the overall trend of experimental results well despite that the predicted values at various roller-leveling conditions showed some deviations from the experimental measurements presumably due to a higher leveling condition in the simulations. The FE simulations for 490DP corresponding experimental conditions delivered key insights for predicting the BH behavior with the present material model which combines the YPP model and the BH model. The uniaxial tension simulations according to various BH conditions overall demonstrated the experimental BH

behaviors except for the yield-point elongations. The compressive responses before and after BH operation in the uniaxial tension-compression simulations were partially described presumably due to the limitation of the present kinematic hardening rule. The static dent simulations including forming simulations were able to roughly depict the experiments. The static dent resistance acquired in the simulations was also commensurate with the experimental results more obviously when the degradation of the elastic modulus was taken into consideration.

To conclude, from these experimental and numerical investigations, we obtained important mechanical insights into both the fluting defect in the v-bending process with its reduction by the roller-leveling process and the BH effects in the static dent case. The capabilities and usefulness of the present FE analysis procedure with the YPP constitutive model and the BH model were demonstrated through various numerical tests. Nevertheless, more refined experimental and computational setup and studies for the roller-leveling process and the static dent case would be beneficial. To take material anisotropy into account for the material model could provide more sophisticated outcomes. Also, on top of this, the extension to fully 3-D simulations with efficiency would be valuable to explore the effect of YPP and BH in actual 3-D parts of a product.

Chapter A

Appendix

A.1 Pseudocodes of UMAT subroutine for numerical simulations

```
      SUBROUTINE UMAT(STRESS,STATEV,DDSDDE,...
     + ...
     + ...,DSTRAN,...,TEMP,DTEMP,...
     + ...,NTENS,NSTATV,...,PNEWDT,
     + ...)
c
      DIMENSION STRESS(NTENS),STATEV(NSTATV),
     + DDSDDE(NTENS,NTENS),...
     + ...,DSTRAN(NTENS),...
     + ...
c
c0. Inputs passed in
c     STRESS: σ_n
c     STATEV: α_n, β_n, θ_n, q_n, and other state variables of the previous
     increment n
c     DDSDDE: D_l^ep or D_w^ep
c     DSTRAN: Δε
c     TEMP, DTEMP: used for BH temperature T_b
c     NTENS: Number of stress or strain components
c     NSTATV: Number of state variables
c     PNEWDT: Ratio of new time increment to the current one
```

c STRESS, STATEV, and DDSDDE should be updated

c

c1. BH calculation

IF(BH temperature) THEN

Calculation of x_b and σ_{prec}

$\boldsymbol{\alpha}_b = \boldsymbol{\alpha}$

ELSE

c

c2. Calculation of $\bar{\sigma}_l^T$ and $\bar{\sigma}_w^T$ assuming $\Delta\boldsymbol{\varepsilon} = \Delta\boldsymbol{\varepsilon}^e$

$\boldsymbol{\sigma}^T = \boldsymbol{\sigma}_n + \mathbf{D} : \Delta\boldsymbol{\varepsilon}^e$

$\bar{\sigma}_l^T = \sqrt{\frac{3}{2}(\mathbf{s}^T - C_b\boldsymbol{\alpha}_b) : (\mathbf{s}^T - C_b\boldsymbol{\alpha}_b)}$ and $\bar{\sigma}_w^T = \sqrt{\frac{3}{2}(\mathbf{s}^T - \boldsymbol{\alpha}_n) : (\mathbf{s}^T - \boldsymbol{\alpha}_n)}$

c

c3. State evaluation whether elastic or not

IF(viscoplastic) THEN

c (i) Stress integration: LB mode

c (a) Upper and lower bound for bisection method

$\mathbb{L}_l^{(0)} = 0$ and $\mathbb{U}_l^{(0)} = \frac{\bar{\sigma}_l^T - Y_l - \sigma_{prec}}{3G}$

c (b) Calculation of $\Delta\bar{\varepsilon}_l$

c One-point Newton method for OP and BI,

$$\Delta\bar{\varepsilon}_l^{(k)} = \Delta\bar{\varepsilon}_l^{(k-1)} - \frac{\psi_l\left(\Delta\bar{\varepsilon}_l^{(k-1)}\right)}{\left.\dfrac{\partial\psi_l}{\partial\Delta\bar{\varepsilon}_l}\right|_{\Delta\bar{\varepsilon}_l = \Delta\bar{\varepsilon}_l^{(k-1)}}} \quad \text{with} \quad \Delta\bar{\varepsilon}_l^{(0)} = \mathbb{L}^{(0)}$$

c Two-point Newton method for TP1 and TP2,

$$\Delta\bar{\varepsilon}_l^{(k+1)} = \Delta\bar{\varepsilon}_l^{(k-1)} + \frac{\Delta\bar{\varepsilon}_l^{(k)} - \Delta\bar{\varepsilon}_l^{(k-1)}}{1 - \dfrac{\psi_l^{(k)}}{\psi_l^{(k-1)}}\dfrac{\psi_l^{(k)} - \psi_l^{(k-1)}}{\Delta\bar{\varepsilon}_l^{(k)} - \Delta\bar{\varepsilon}_l^{(k-1)}}\dfrac{1}{\left.\dfrac{d\psi_l}{d\Delta\bar{\varepsilon}_l}\right|_{\Delta\bar{\varepsilon}_l = \Delta\bar{\varepsilon}_l^{(k)}}}}$$

with $\Delta\bar{\varepsilon}_l^{(0)} = \mathbb{L}^{(0)}$ and $\Delta\bar{\varepsilon}_l^{(1)} = \mathbb{U}^{(0)}/2$

IF(converged) THEN

CONTINUE

ELSE

c Bisection method for BI, TP1 and TP2

$\mathbb{L}_l^{(k)} = \frac{\mathbb{L}_l^{(k-1)} + \mathbb{U}_l^{(k-1)}}{2}$ if $\psi_l(\mathbb{L}_l^{(k)}) \cdot \psi_l(\mathbb{L}_l^{(k-1)}) > 0$

$\mathbb{U}_l^{(k)} = \frac{\mathbb{L}_l^{(k-1)} + \mathbb{U}_l^{(k-1)}}{2}$ otherwise

IF(converged) THEN

CONTINUE

ELSE

```
c          New increment attempt with a decreased time increment
           PNEWDT=0.5
           RETURN
          END IF
         END IF
c      (ii) Stress integration: WH mode
c       (a) WH initialization (only for BI, TP1 and TP2)
c        Calculation of 𝕌_w^(0) by solving
         σ̄_w^T − 3GΔε̄_w − Y_w − σ_prec = 0 with the one-point Newton method
c        (initial value: (σ̄_w^T − Y_wn − σ_prec)/3G)
c        Calculation of Δε̄_w^(0) by solving
         (Δε̄_w/Δt) − (b f_m ρ_t/M) ((σ̄_w^𝕋 − 3GΔε̄_w − Y_w − σ_prec)/D_w)^n_e = 0
c         for BI
          with one-point Newton method (initial value: 0)
c         for TP1 and TP2
          with two-point Newton method (initial values: 0 and 𝕌_w^(0)/2)
          IF(converged) THEN
           CONTINUE
          ELSE
           Bisection method with 𝕃_w^(0) = 0 and 𝕌_w^(0)
           IF(converged) THEN
            CONTINUE
           ELSE
            PNEWDT=0.5
            RETURN
           END IF
          END IF
          Δε̄_w^(1) = 𝕌_w^(0)/2
          β^(i) = (β_n + (2/3) b_1 m Δε̄_w^(i) n_wn)/(1 + m Δε̄_w^(i)) and ϑ^(i) = (ϑ_n + (2/3) C a_n Δε̄_w^(i) n_wn)/(1 + C Δε̄_w^(i) √(a_n/θ̄_n))
c       (b) Calculation of Δε̄_w, ϑ and β
c        Check isotropic hardening flag (ih_flag)
         IF(ih_flag) THEN
          R_b update
         ELSE
          R_b no update
         END IF
c        One-point Newton method for OP, BI and TP1
         (∂ψ_w/∂Δε̄_w) dΔε̄_w + (∂ψ_w/∂ϑ) : dϑ + (∂ψ_w/∂β) : dβ = −ψ_w
         (∂Ψ_θ/∂Δε̄_w) dΔε̄_w + (∂Ψ_θ/∂ϑ) : dϑ + (∂Ψ_θ/∂β) : dβ = −Ψ_θ
```

$\frac{\partial \boldsymbol{\Psi}_\beta}{\partial \Delta \bar{\boldsymbol{\varepsilon}}_w} \mathrm{d}\Delta \bar{\boldsymbol{\varepsilon}}_w + \frac{\partial \boldsymbol{\Psi}_\beta}{\partial \boldsymbol{\theta}} : \mathrm{d}\boldsymbol{\theta} + \frac{\partial \boldsymbol{\Psi}_\beta}{\partial \boldsymbol{\beta}} : \mathrm{d}\boldsymbol{\beta} = -\boldsymbol{\Psi}_\beta$

$\Delta \bar{\boldsymbol{\varepsilon}}_w^{(k)} := \Delta \bar{\boldsymbol{\varepsilon}}_w^{(k-1)} + \mathrm{d}\Delta \bar{\boldsymbol{\varepsilon}}_w$

$\boldsymbol{\theta}^{(k)} := \boldsymbol{\theta}^{(k-1)} + \mathrm{d}\boldsymbol{\theta}$

$\boldsymbol{\beta}^{(k)} := \boldsymbol{\beta}^{(k-1)} + \mathrm{d}\boldsymbol{\beta}$

```
c       Two-point Newton method for TP2
```

$\boldsymbol{\gamma}^{(k+1)} = \boldsymbol{\gamma}^{(k)} - (\mathbf{J}^{(k)} + \boldsymbol{\Psi}^{(k)} \otimes \mathbf{b}^{(k)})^{-1} \boldsymbol{\Psi}^{(k)}$

$$\mathbf{J}^{(k)} = \begin{bmatrix} \frac{\partial \psi_w}{\partial \Delta \bar{\boldsymbol{\varepsilon}}_w} & \frac{\partial \psi_w}{\partial \boldsymbol{\theta}} & \frac{\partial \psi_w}{\partial \boldsymbol{\beta}} \\ \frac{\partial \boldsymbol{\Psi}_\theta}{\partial \Delta \bar{\boldsymbol{\varepsilon}}_w} & \frac{\partial \boldsymbol{\Psi}_\theta}{\partial \boldsymbol{\theta}} & \frac{\partial \boldsymbol{\Psi}_\theta}{\partial \boldsymbol{\beta}} \\ \frac{\partial \boldsymbol{\Psi}_\beta}{\partial \Delta \bar{\boldsymbol{\varepsilon}}_w} & \frac{\partial \boldsymbol{\Psi}_\beta}{\partial \boldsymbol{\theta}} & \frac{\partial \boldsymbol{\Psi}_\beta}{\partial \boldsymbol{\beta}} \end{bmatrix}_{\boldsymbol{\gamma}=\boldsymbol{\gamma}^{(k)}}$$

$$\mathbf{b}^{(k)} = \frac{(\boldsymbol{\Psi}^{(k)} - \boldsymbol{\Psi}^{(k-1)}) \cdot \left[(\boldsymbol{\Psi}^{(k)} - \boldsymbol{\Psi}^{(k-1)}) - \mathbf{J}^{(k)} (\boldsymbol{\gamma}^{(k)} - \boldsymbol{\gamma}^{(k-1)}) \right]}{\| \boldsymbol{\Psi}^{(k)} - \boldsymbol{\Psi}^{(k-1)} \|^2 \| \boldsymbol{\gamma}^{(k)} - \boldsymbol{\gamma}^{(k-1)} \|^2} (\boldsymbol{\gamma}^{(k)} - \boldsymbol{\gamma}^{(k-1)})$$

```
      IF(converged) THEN
       CONTINUE
      ELSE
       PNEWDT=0.5
       RETURN
      END IF
c     Workhardening stagnation
```

$\Delta \boldsymbol{\beta} = \boldsymbol{\beta} - \boldsymbol{\beta}_n \quad \text{and} \quad \boldsymbol{\xi}_n = \boldsymbol{\beta} - \mathbf{q}_n$

```
      IF((3/2)(ξ_n : ξ_n) − r_n^2 > 0) THEN
       IF(ih_flag) THEN
```

$r^2 = r_n^2 + 3h\boldsymbol{\xi} : \Delta\boldsymbol{\beta}$

$\mathbf{q} = \mathbf{q}_n + \Delta\mu\boldsymbol{\xi}$

$\boldsymbol{\xi} = \frac{\boldsymbol{\xi}_n}{1+\Delta\mu}$

$\Delta\mu = \frac{-3h\boldsymbol{\xi}_n : \Delta\boldsymbol{\beta} + \sqrt{(3h\boldsymbol{\xi}_n : \Delta\boldsymbol{\beta})^2 + 4r_n^2 \left(\frac{3}{2}\boldsymbol{\xi}_n : \boldsymbol{\xi}_n\right)}}{2r_n^2} - 1$

```
       ELSE
        ih_flag=TRUE
        GOTO (b)
       END IF
      ELSE
       IF(ih_flag) THEN
        ih_flag=FALSE
        GOTO (b)
       ELSE
        CONTINUE
       END IF
      END IF
c     (c) State variables update
      STATEV=new values
c    (iii) Mode selection
```

```
          IF (Δε̄_l < Δε̄_w) THEN
c          LB mode
           Δε^e = Δε − Δε̄_l n_l
           DDSDDE = D_l^ep = 2GV_l I_d + (4/3)GQ_l (n_l ⊗ n_l) + K (I ⊗ I)
          ELSE
c          WH mode
           Δε^e = Δε − Δε̄_w n_w
           DDSDDE = D_w^ep = 2GI_d + [2GV_w I_s − (4/3)GQ_w (n_w ⊗ n_w)] : Ξ + K (I ⊗ I)
          END IF
c         Stress update
          STRESS (σ) = σ_n + D : Δε^e
        ELSE
c    Current state is elastic
          STRESS (σ) = σ^T
          DDSDDE = D
c        State evaluation whether elastic or not 'END IF'
        END IF
c      BH calculation 'END IF'
       END IF
       RETURN
       END
```

A.2 Hertz contact problem for validating the parameters of the exponential pressure-overclosure relationship

The exponential pressure-overclosure relationship between the contact pressure p_{ex} and the contact clearance c in Abaqus/Standard is defined as

$$p_{ex}(c) = \begin{cases} 0, & c \geq c_0 \\ p_0 \left(1 - \frac{c}{c_0}\right) \frac{\exp\left(1-\frac{c}{c_0}\right)-1}{\exp(1)-1}, & c < c_0 \end{cases}, \tag{A.2.1}$$

where p_0 and c_0 are the contact pressure at zero clearance and the clearance at zero contact pressure, respectively. In order to verify the validity of the parameters of the exponential pressure-overclosure relationship used in the simulations of the roller-leveling and the v-bending, simple simulations for the 2-D Hertzian contact problem as shown in Fig.A.2.1a are performed using the benchmark analysis model of Abaqus/Standard

as depicted in Fig.A.2.1b. The simulations use the three contact conditions for normal

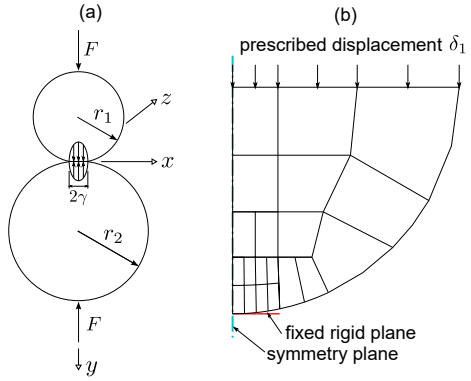

Figure A.2.1. Hertzian contact problem: (a) 2-D contact model for two infinitely long cylinders Franke (2011), (b) 2-D quarter-cylinder model meshed with 8-node plane strain elements and a rigid plane in the benchmark problem in Abaqus/Standard.

behavior: (a) hard contact, (b) softened contact with $p_0 = 30$ MPa and $c_0 = 0.0001$ mm, and (c) softened contact with $p_0 = 3$ MPa and $c_0 = 0.01$ mm.

For the analytic contact solution between a cylinder and a rigid plane, assuming r_2 and the Young's modulus E_2 of the lower cylinder are infinite, Franke (2011) derived the distribution of the pressure in the contact interface as follows

$$p(x) = \frac{E_1}{2r_1(1-\nu_1^2)}\sqrt{\gamma^2 - x^2}, \tag{A.2.2}$$

and the half width γ of the contact interface can be given as

$$\gamma = \sqrt{\frac{4Fr_1}{\pi l}\frac{(1-\nu_1^2)r_1}{E_1}}, \tag{A.2.3}$$

where E_1 and ν_1 denote the Young's modulus and the Poisson's ratio of the lower cylinder, respectively. The length of the cylinders is l. Referring to Johnson (1987), the prescribed displacement δ_1 indicated in Fig.A.2.1 can be calculated as

$$\delta_1 = \frac{F}{\pi l}\frac{(1-\nu_1^2)}{E_1}\left(2\ln\frac{4r_1}{\gamma} - 1\right) = 0.4 \tag{A.2.4}$$

with $E_1 = 199514$ GPa, $\nu_1 = 0.3$, $l = 1$ mm, $r_1 = 10$ mm, and $F = 52,314$ N.

The contact pressures obtained from the simulations and the analytic solution calculated with Eq.(A.2.2) are plotted in Fig.A.2.2. The softened contact condition

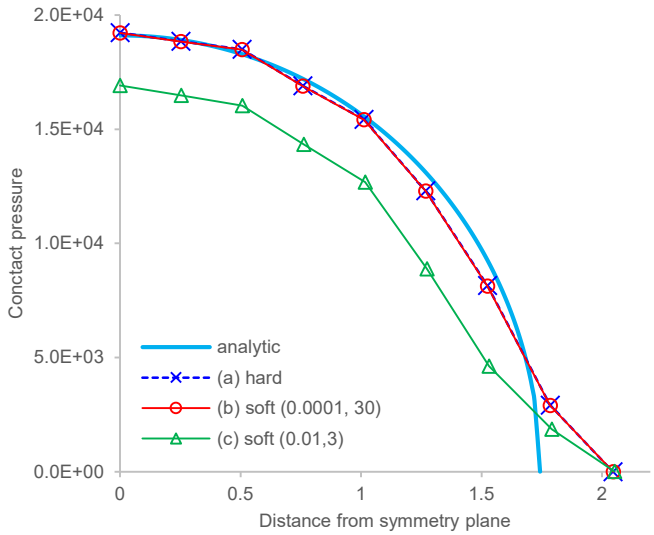

Figure A.2.2. Contact pressure calculated from the simulations and the analytic solution.

(b) is as accurate as the hard contact condition while the condition (c) shows weaker contact pressure. The reaction forces measured from the rigid plane and the maximum penetration at the bottom nodes are entered in Table A.2.1. Even though the forces

Table A.2.1. Reaction force of the rigid plane and maximum penetrations at the bottom nodes.

	analytic	(a) hard	(b) soft (30, 0.0001)	(c) soft (3, 0.01)
reaction force (N)	52,314	52,214	52,152	43,364
maximum penetration (mm)	0.0e0	0.0e0	4.3392e-4	6.2047e-2

of the simulations are smaller than the analytic value, the force of the condition (b) is acceptable as that of the condition (a). No penetration occurs in the condition (a), whereas the maximum penetrations in the condition (b) and (c) are about 4.34e-4 mm and 6.20e-2 mm, respectively, at the bottom node. Depending on the dimensional scale of FE models, this penetration amount of the condition (b) can be negligible.

References

Abspoel, M., Scholting, M. E., Lansbergen, M., An, Y., and Vegter, H. (2017). "A new method for predicting advanced yield criteria input parameters from mechanical properties". In: *Journal of Materials Processing Technology* 248, pp. 161–177. ISSN: 0924-0136. DOI: 10.1016/J.JMATPROTEC.2017.05.006.

Aratani, M., Tosaka, A., Furukimi, O., Obara, T., and Kuguminato, H. (1997). "The effect of deformation conditions on the occurrence of fluting at 3-pieces can body making". In: *Tetsu-to-Hagane* 83.4, pp. 251–256. ISSN: 0021-1575. DOI: 10.2355/tetsutohagane1955.83.4_251.

Asnafi, N. (1995). "On strength, stiffness and dent resistance of car body panels". In: *Journal of Materials Processing Technology* 49.1-2, pp. 13–31. ISSN: 0924-0136. DOI: 10.1016/0924-0136(94)01333-V.

Bae, G. H. and Huh, H. (2011). "Tension/compression test of auto-body steel sheets with the variation of the pre-strain and the strain rate". In: *WIT Transactions on Engineering Sciences* 72, pp. 213–225. DOI: 10.2495/MC110191.

Baker, L. J., Daniel, S. R., and Parker, J. D. (2002). "Metallurgy and processing of ultralow carbon bake hardening steels". In: *Materials Science and Technology* 18.4, pp. 355–368. ISSN: 0267-0836. DOI: 10.1179/026708302225002452.

Ballarin, V., Perlade, A., Lemoine, X., Bouaziz, O., and Forest, S. (2009a). "Mechanisms and Modelling of Bake-Hardening Steels: Part II. Complex Loading Paths". In: *Metallurgical and Materials Transactions A: Physical Metallurgy and Materials Science* 40.6, pp. 1375–1382. ISSN: 1073-5623. DOI: 10.1007/s11661-009-9812-6.

Ballarin, V., Soler, M., Perlade, A., Lemoine, X., and Forest, S. (2009b). “Mechanisms and modeling of bake-hardening steels: Part I. Uniaxial tension”. In: *Metallurgical and Materials Transactions A: Physical Metallurgy and Materials Science* 40.6, pp. 1367–1374. ISSN: 1073-5623. DOI: 10.1007/s11661-009-9813-5.

Boger, R. K., Wagoner, R. H., Barlat, F., Lee, M. G., and Chung, K. (2005). “Continuous, large strain, tension/compression testing of sheet material”. In: *International Journal of Plasticity* 21.12, pp. 2319–2343. ISSN: 0749-6419. DOI: 10.1016/j.ijplas.2004.12.002.

Cao, J. and Wang, X. (2000). “An analytical model for plate wrinkling under tri-axial loading and its application”. In: *International Journal of Mechanical Sciences* 42.3, pp. 617–633. ISSN: 0020-7403. DOI: 10.1016/S0020-7403(98)00138-6.

Chipman, J. (1972). “Thermodynamics and phase diagram of the Fe-C system”. In: *Metallurgical and Materials Transactions B* 3.1, pp. 55–64. ISSN: 1543-1916. DOI: 10.1007/BF02680585.

Chung, K. and Richmond, O. (1993). “A deformation theory of plasticity based on minimum work paths”. In: *International Journal of Plasticity* 9.8, pp. 907–920. ISSN: 0749-6419. DOI: 10.1016/0749-6419(93)90057-W.

Cochardt, A. W., Schoek, G., and Wiedersich, H. (1955). “Interaction between dislocations and interstitial atoms in body-centered cubic metals”. In: *Acta Metallurgica* 3.6, pp. 533–537. ISSN: 0001-6160. DOI: https://doi.org/10.1016/0001-6160(55)90111-5.

Conrad, H. (1964). “Thermally activated deformation of metals”. In: *Journal of Metals* 16.7, pp. 582–588. ISSN: 1543-1851. DOI: 10.1007/BF03378292.

Cottrell, A. H. and Bilby, B. A. (1949). “Dislocation Theory of Yielding and Strain Ageing of Iron”. In: *Proceedings of the Physical Society. Section A* 62.1, pp. 49–62. ISSN: 0370-1298. DOI: 10.1088/0370-1298/62/1/308.

Das, S., Mohanty, O. N., and Singh, S. B. (2014). “A phenomenological model for bake hardening in minimal carbon steels”. In: *Philosophical Magazine* 94.18, pp. 2046–2061. ISSN: 1478-6435. DOI: 10.1080/14786435.2014.906754.

De, A. K., De Cooman, B. C., and Vandeputte, S. (2001). “Kinetics of strain aging in bake hardening ultra low carbon steel—a comparison with low carbon steel”. In: *Journal of Materials Engineering and Performance* 10.5, pp. 567–575. ISSN: 1544-1024. DOI: 10.1361/105994901770344719.

Ding, S. C. and Duncan, J. L. (2004). “Instability in bending-under-tension of aged steel sheet”. In: *International Journal of Mechanical Sciences* 46.10, pp. 1471–1480. ISSN: 0020-7403. DOI: 10.1016/j.ijmecsci.2004.09.008.

Duncan, J. L., Ding, S. C., and Jiang, W. L. (1999). “Moment-curvature measurement in thin sheet–part II: yielding and kinking in aged steel sheet”. In: *International Journal of Mechanical Sciences* 41.3, pp. 261–267. ISSN: 0020-7403. DOI: 10.1016/S0020-7403(98)00032-0.

Elsen, P. and Hougardy, H. P. (1993). “On the mechanism of bake-hardening”. In: *Steel Research* 64.8-9, pp. 431–436. ISSN: 0177-4832. DOI: 10.1002/srin.199301049.

Franke, D. (2011). “Investigation of mechanical contact problems with high-order finite element methods”. Thesis. Technical University of Munich.

Ghaei, A. and Green, D. E. (2010). “Numerical implementation of Yoshida-Uemori two-surface plasticity model using a fully implicit integration scheme”. In: *Computational Materials Science* 48.1, pp. 195–205. ISSN: 0927-0256. DOI: 10.1016/j.commatsci.2009.12.028.

Ghaei, A., Green, D. E., and Taherizadeh, A. (2010). “Semi-implicit numerical integration of Yoshida-Uemori two-surface plasticity model”. In: *International Journal of Mechanical Sciences* 52.4, pp. 531–540. ISSN: 0020-7403. DOI: 10.1016/j.ijmecsci.2009.11.018.

Giarola, A. M., Pereira, P. H. R., Stemler, P. A., Pertence, A. E. M., Campos, H. B., Aguilar, M. T. P., and Cetlin, P. R. (2015). “Strain heterogeneities in the rolling

direction of steel sheets submitted to the skin pass: A finite element analysis". In: *Journal of Materials Processing Technology* 216, pp. 234–247. ISSN: 0924-0136. DOI: 10.1016/j.jmatprotec.2014.09.015.

Gladman, T. (1999). "Precipitation hardening in metals". In: *Materials Science and Technology* 15.1, pp. 30–36. ISSN: 0267-0836. DOI: 10.1179/026708399773002782.

Hahn, G. T. (1962). "A model for yielding with special reference to the yield-point phenomena of iron and related bcc metals". In: *Acta Metallurgica* 10.8, pp. 727–738. ISSN: 0001-6160. DOI: 10.1016/0001-6160(62)90041-x.

Hall, E. O. (1970). *Yield phenomena in metals and alloys*. New York: Plenum Press. DOI: 10.1007/978-1-4684-1860-6.

Harper, S. (1951). "Precipitation of Carbon and Nitrogen in Cold-Worked Alpha-Iron". In: *Physical Review* 83.4, pp. 709–712. DOI: 10.1103/PhysRev.83.709.

Hartley, S. (1966). "Strain-ageing in tantalum". In: *Acta Metallurgica* 14.10, pp. 1237–1246. ISSN: 0001-6160. DOI: 10.1016/0001-6160(66)90241-0.

Hasegawa, T., Yakou, T., and Karashima, S. (1975). "Deformation behaviour and dislocation structures upon stress reversal in polycrystalline aluminium". In: *Materials Science and Engineering* 20, pp. 267–276. ISSN: 0025-5416. DOI: 10.1016/0025-5416(75)90159-7.

Holmberg, S. and Nejabat, B. (2004). "Numerical assessment of stiffness and dent properties of automotive exterior panels". In: *Materials & Design* 25.5, pp. 361–368. ISSN: 0261-3069. DOI: 10.1016/J.MATDES.2003.12.005.

Holmberg, S. and Thilderkvist, P. (2002). "Influence of material properties and stamping conditions on the stiffness and static dent resistance of automotive panels". In: *Materials & Design* 23.8, pp. 681–691. ISSN: 0261-3069. DOI: 10.1016/S0261-3069(02)00079-1.

Hosford, W. F. and Caddell, R. M. (2011). *Metal Forming: Mechanics and Metallurgy*. New York: Cambridge University Press. DOI: 10.1017/CBO9780511976940.

Hu, Z., Rauch, E. F., and Teodosiu, C. (1992). “Work-hardening behavior of mild steel under stress reversal at large strains”. In: *International Journal of Plasticity* 8.7, pp. 839–856. ISSN: 0749-6419. DOI: 10.1016/0749-6419(92)90006-X.

Hutchison, M. (1957). “High upper yield points in mild steel”. In: *The Journal of the Iron and Steel Institute* 186, pp. 431–432.

Johnson, K. L. (1987). *Contact mechanics*. Cambridge: Cambridge university press. DOI: 10.1017/CBO9781139171731.

Johnston, W. G. and Gilman, J. J. (1959). “Dislocation velocities, dislocation densities, and plastic flow in lithium fluoride crystals”. In: *Journal of Applied Physics* 30.2, pp. 129–144. ISSN: 0021-8979. DOI: 10.1063/1.1735121.

Jung, D.-W. (2002). “A parametric study of sheet metal denting using a simplified design approach”. In: *KSME International Journal* 16.12, pp. 1673–1686. ISSN: 1738-494X. DOI: 10.1007/BF03021669.

Kantereit, H. (2011). *Bake Hardening Behavior of Advanced High Strength Steels under Manufacturing Conditions*. Tech. rep. SAE Technical Paper. DOI: 10.4271/2011-01-1053.

Kim, J. and Kim, D. N. (2019). “Robust stress integration algorithms for implicit elasto-viscoplastic finite element analysis of materials with yield-point phenomenon”. In: *International Journal of Mechanical Sciences* 150, pp. 277–289. ISSN: 0020-7403. DOI: 10.1016/j.ijmecsci.2018.10.018.

Kim, J., Park, K.-C., and Kim, D.-N. (2019). “Investigating the fluting defect in v-bending due to the yield-point phenomenon and its reduction via roller-leveling process”. In: *Journal of Materials Processing Technology* 270, pp. 59–81. ISSN: 0924-0136. DOI: 10.1016/J.JMATPROTEC.2019.02.016.

Krieg, R. D. and Krieg, D. B. (1977). “Accuracies of Numerical Solution Methods for the Elastic-Perfectly Plastic Model”. In: *Journal of Pressure Vessel Technology* 99.4, pp. 510–515. ISSN: 0094-9930. DOI: 10.1115/1.3454568.

Krieg, R. D. (1975). “A practical two surface plasticity theory”. In: *Journal of applied mechanics* 42.3, pp. 641–646. ISSN: 0021-8936. DOI: 10.1115/1.3423656.

Lee, J.-Y., Lee, M.-G., Barlat, F., Chung, K.-H., and Kim, D.-J. (2016). “Effect of non-linear multi-axial elasticity and anisotropic plasticity on quasi-static dent properties of automotive steel sheets”. In: *International Journal of Solids and Structures* 87, pp. 254–266. ISSN: 0020-7683. DOI: 10.1016/J.IJSOLSTR.2016.01.020.

Leslie, W. C. (1991). *The physical metallurgy of steels*. Herndon, VA: TechBooks. ISBN: 0070377804.

Lüders, W. (1860). “Über die Äußerung der Elasticität an stahlartigen Eisenstäben und Stahlstäben, und über eine beim Biegen solcher Stäbe beobachtete Molecularbewegung”. In: *Polytechnisches Journal* 155, pp. 18–22.

Mao, B. and Liao, Y. (2019). “Modeling of lüders elongation and work hardening behaviors of ferrite-pearlite dual phase steels under tension”. In: *Mechanics of Materials* 129, pp. 222–229. ISSN: 0167-6636. DOI: 10.1016/J.MECHMAT.2018.11.015.

Markiewicz, É., Langrand, B., Leconte, N., Fabis, J., and Dupuy, T. (2016). “A methodology for the viscoplastic behaviour characterisation of spot-weld heat affected materials”. In: *Journal of Materials Processing Technology* 238, pp. 169–180. ISSN: 0924-0136. DOI: 10.1016/J.JMATPROTEC.2016.07.022.

Mazière, M. and Forest, S. (2015). “Strain gradient plasticity modeling and finite element simulation of Lüders band formation and propagation”. In: *Continuum Mechanics and Thermodynamics* 27.1-2, pp. 83–104. ISSN: 0935-1175. DOI: 10.1007/s00161-013-0331-8.

Ortiz, M. and Popov, E. P. (1985). “Accuracy and stability of integration algorithms for elastoplastic constitutive relations”. In: *International journal for numerical methods in engineering* 21.9, pp. 1561–1576. ISSN: 0029-5981. DOI: 10.1002/nme.1620210902.

Park, K.-C. (2015). “Leveling of Aged Low Carbon Steel Sheets in order to Prevent Shape Defects after Stamping”. In: *Transactions of Materials Processing* 24.4, pp. 241–247. ISSN: 1225-696X. DOI: 10.5228/KSTP.24.4.241.

Park, K.-C. and Hwang, S. M. (2002). “Development of a Finite Element Analysis Program for Roller Leveling and Application for Removing Blanking Bow Defects of Thin Steel Sheet”. In: *ISIJ International* 42.9, pp. 990–999. DOI: 10.2355/isijinternational.42.990.

Park, K.-C., Kim, H. J., and Kim, G. S. (2006). “Leveling Condition in Cut-To-Length Lines to Produce Low Residual Stress Flat Plate from Hot Rolled Coils”. In: *Transactions of Materials Processing* 15.4, pp. 311–318. ISSN: 1225-696X. DOI: 10.5228/KSPP.2006.15.4.311.

Park, K.-C. and Yoon, J. B. (2007). “Analysis on the Mechanism of Fluting in the Bending of Low Carbon Steels”. In: *Transactions of Materials Processing* 16.4, pp. 317–322. ISSN: 1225-696X. DOI: 10.5228/KSPP.2007.16.4.317.

Pearce, R. (1991). *Sheet Metal Forming*. New York: Adam Hilger.

Pepelnjak, T. and Barisic, B. (2007). “Analysis and elimination of the stretcher strains on TH415 tinplate rings in the stamping process”. In: *Journal of Materials Processing Technology* 186.1, pp. 111–119. ISSN: 0924-0136. DOI: 10.1016/j.jmatprotec.2006.12.025.

Piobert, G., Didion, I., and Morin, A. (1842). “Expérience sur la pénétration des projectiles dans le fer forgé”. In: *Mémorial de l’artillerie* 5, pp. 501–552.

Prior, A. M. (1994). “Applications of implicit and explicit finite element techniques to metal forming”. In: *Journal of Materials Processing Tech.* 45.1-4, pp. 649–656. ISSN: 0924-0136. DOI: 10.1016/0924-0136(94)90413-8.

Ramazani, A., Bruehl, S., Gerber, T., Bleck, W., and Prahl, U. (2014). “Quantification of bake hardening effect in DP600 and TRIP700 steels”. In: *Materials and Design* 57, pp. 479–486. ISSN: 1873-4197. DOI: 10.1016/j.matdes.2014.01.001.

Rana, R. and Singh, S. B. (2017). *Automotive Steels: Design, Metallurgy, Processing and Applications*. Woodhead Publishing, p. 478. ISBN: 9780081006535. DOI: 10.1016/S0140-6736(12)60861-7.

Rezaiee-Pajand, M., Auricchio, F., Sharifian, M., and Sharifian, M. (2014). "Computational plasticity of mixed hardening pressure-dependency constitutive equations". In: *Acta Mechanica* 225.6, pp. 1699–1733. ISSN: 1619-6937. DOI: 10.1007/s00707-013-0998-8.

Rezaiee-Pajand, M., Nasirai, C., and Sharifian, M. (2010). "Application of exponential-based methods in integrating the constitutive equations with multicomponent nonlinear kinematic hardening". In: *Journal of Engineering Mechanics* 136.12, pp. 1502–1518. ISSN: 0733-9399. DOI: 10.1061/(ASCE)EM.1943-7889.0000192.

Rezaiee-Pajand, M., Nasirai, C., and Sharifian, M. (2011a). "Integration of nonlinear mixed hardening models". In: *Multidiscipline Modeling in Materials and Structures* 7.3, pp. 266–305. ISSN: 1573-6105. DOI: 10.1108/1536-540911178252.

Rezaiee-Pajand, M., Sharifian, M., and Sharifian, M. (2011b). "Accurate and approximate integrations of Drucker-Prager plasticity with linear isotropic and kinematic hardening". In: *European Journal of Mechanics, A/Solids* 30.3, pp. 345–361. ISSN: 0997-7538. DOI: 10.1016/j.euromechsol.2010.12.001.

Saheya, B., Chen, G. Q., Sui, Y. K., and Wu, C. Y. (2016). "A new Newton-like method for solving nonlinear equations". In: *SpringerPlus* 5.1, p. 1269. ISSN: 2193-1801. DOI: 10.1186/s40064-016-2909-7.

Schwab, R. and Ruff, V. (2013). "On the nature of the yield point phenomenon". In: *Acta Materialia* 61.5, pp. 1798–1808. ISSN: 1359-6454. DOI: 10.1016/j.actamat.2012.12.003.

Shen, H., Li, S., and Chen, G. (2010). "Numerical analysis of panels' dent resistance considering the Bauschinger effect". In: *Materials & Design* 31.2, pp. 870–876. ISSN: 0261-3069. DOI: 10.1016/J.MATDES.2009.07.043.

Simo, J. C. and Taylor, R. L. (1985). "Consistent tangent operators for rate-independent elastoplasticity". In: *Computer methods in applied mechanics and engineering* 48.1, pp. 101–118. ISSN: 0045-7825. DOI: 10.1016/0045-7825(85)90070-2.

Souza Neto, E. A. de, Perić, D., and Owen, D. R. (2011). *Computational methods for plasticity: theory and applications*. Chichester: John Wiley & Sons. ISBN: 1119964547. DOI: 10.1002/9780470694626.

Sun, H. B., Yoshida, F., Ohmori, M., and Ma, X. (2003). "Effect of strain rate on Lüders band propagating velocity and Lüders strain for annealed mild steel under uniaxial tension". In: *Materials Letters* 57.29, pp. 4535–4539. ISSN: 0167-577X. DOI: 10.1016/S0167-577X(03)00358-6.

Theis, H. E. (1999). *Handbook of Metalforming processes*. New York: CRC Press.

Timokhina, I. B., Hodgson, P. D., and Pereloma, E. V. (2007). "Transmission Electron Microscopy Characterization of the Bake-Hardening Behavior of Transformation-Induced Plasticity and Dual-Phase Steels". In: *Metallurgical and Materials Transactions A* 38.10, pp. 2442–2454. ISSN: 1543-1940. DOI: 10.1007/s11661-007-9258-7.

Tiruneh, A. T., Ndlela, W. N., and Nkambule, S. J. (2013). "A Two-Point Newton Method Suitable for Nonconvergent Cases and with Super-Quadratic Convergence". In: *Advances in Numerical Analysis* 2013. ISSN: 1687-9562. DOI: 10.1155/2013/687382.

Trzepiecinski, T. and Lemu, H. G. (2017). "Effect of Computational Parameters on Springback Prediction by Numerical Simulation". In: *Metals* 7.9, p. 380. DOI: 10.3390/met7090380.

Tsukahara, H. and Iung, T. (1998). "Finite element simulation of the Piobert–Lüders behavior in an uniaxial tensile test". In: *Materials Science and Engineering: A* 248.1, pp. 304–308. ISSN: 0921-5093. DOI: https://doi.org/10.1016/S0921-5093(97)00857-5.

Turner, T. J. and Miller, M. P. (2006). "Modeling the Influence of Material Structure on Deformation Induced Surface Roughening in AA7050 Thick Plate". In: *Journal of*

Engineering Materials and Technology 129.3, pp. 367–379. ISSN: 0094-4289. DOI: 10.1115/1.2744395.

Van Rooyen, G. (1971). "Basic factors which influence the Lüders strain during discontinuous yielding". In: *Materials Science and Engineering* 7.1, pp. 37–48. ISSN: 0025-5416. DOI: 10.1016/0025-5416(71)90059-0.

Watanabe, T. (1982). "Effect of Strain Rate on Yield Behavior of Cold-rolled Sheet Steel". In: *Transactions of the Iron and Steel Institute of Japan* 22.5, pp. 385–390. DOI: 10.2355/isijinternational1966.22.385.

Waterschoot, T., De Cooman, B. C., De, A. K., and Vandeputte, S. (2003). "Static strain aging phenomena in cold-rolled dual-phase steels". In: *Metallurgical and Materials Transactions A* 34.3, pp. 781–791. ISSN: 1543-1940. DOI: 10.1007/s11661-003-0113-1.

Wenman, M. R. and Chard-Tuckey, P. R. (2010). "Modelling and experimental characterisation of the Lüders strain in complex loaded ferritic steel compact tension specimens". In: *International Journal of Plasticity* 26.7, pp. 1013–1028. ISSN: 0749-6419. DOI: 10.1016/j.ijplas.2009.12.005.

Wilkins, M. L. (1964). "Computation of elastic–plastic flow". In: *Methods in Computational Physics* 3. Ed. by B. Alders.

Wilson, D. and Russell, B. (1960). "The contribution of atmosphere locking to the strain-ageing of low carbon steels". In: *Acta Metallurgica* 8.1, pp. 36–45. ISSN: 0001-6160. DOI: 10.1016/0001-6160(60)90138-3.

Yoshida, F. (2000). "A constitutive model of cyclic plasticity". In: *International Journal of Plasticity* 16.3, pp. 359–380. ISSN: 0749-6419. DOI: 10.1016/S0749-6419(99)00058-3.

Yoshida, F., Kaneda, Y., and Yamamoto, S. (2008). "A plasticity model describing yield-point phenomena of steels and its application to FE simulation of temper rolling". In: *International Journal of Plasticity* 24.10, pp. 1792–1818. ISSN: 0749-6419. DOI: 10.1016/j.ijplas.2008.05.004.

Yoshida, F. and Uemori, T. (2003). “A model of large-strain cyclic plasticity and its application to springback simulation”. In: *International Journal of Mechanical Sciences* 45.10, pp. 1687–1702. ISSN: 0020-7403. DOI: 10.1016/j.ijmecsci.2003.10.013.

Yoshida, F., Uemori, T., and Fujiwara, K. (2002). “Elastic-plastic behavior of steel sheets under in-plane cyclic tension-compression at large strain”. In: *International Journal of Plasticity* 18.5, pp. 633–659. ISSN: 0749-6419. DOI: 10.1016/S0749-6419(01)00049-3.

Zener, C. (1949). “Theory of Growth of Spherical Precipitates from Solid Solution”. In: *Journal of Applied Physics* 20.10, pp. 950–953. ISSN: 0021-8979. DOI: 10.1063/1.1698258.

Žerovnik, A., Kunc, R., and Prebil, I. (2010). “Yield-point phenomenon in constitutive models of cyclic plasticity”. In: *Computational Materials Science* 49.3, pp. 473–482. ISSN: 0927-0256. DOI: 10.1016/j.commatsci.2010.05.038.

Žerovnik, A., Pepel, V., Prebil, I., and Kunc, R. (2016). “The yield-point phenomenon and cyclic plasticity of the uniaxially loaded specimens”. In: *Materials and Design* 92, pp. 971–977. ISSN: 1873-4197. DOI: 10.1016/j.matdes.2015.12.111.

Zhang, C., Gong, B., Deng, C., and Wang, D. (2017). “Orientation dependence of deformation and failure in a C-Mn weld metal”. In: *Journal of Materials Processing Technology* 250, pp. 363–371. ISSN: 0924-0136. DOI: 10.1016/J.JMATPROTEC.2017.08.003.

Zhang, J., Fu, R., Zhang, M., Liu, R., Wei, X., and Li, L. (2008). “Bake hardening behavior of TRIP and DP steels”. In: *Journal of University of Science and Technology Beijing: Mineral Metallurgy Materials (Eng Ed)* 15.2, pp. 132–137. ISSN: 1005-8850. DOI: 10.1016/S1005-8850(08)60026-2.

Zhang, S., McCormick, P. G., and Estrin, Y. (2001). “The morphology of Portevin-Le Chatelier bands: finite element simulation for Al-Mg-Si”. In: *Acta Materialia* 49.6, pp. 1087–1094. ISSN: 1359-6454. DOI: 10.1016/S1359-6454(00)00380-3.

Zhao, J. Z., De, A. K., and De Cooman, B. C. (2001). “Formation of the cottrell atmosphere during strain aging of bake-hardenable steels”. In: *Metallurgical and Materials Transactions A* 32.2, pp. 417–423. ISSN: 1543-1940. DOI: 10.1007/s11661-001-0273-9.

초 록

소둔이 되었거나 시효가 발생한 금속의 항복점 현상은 이 현상을 회피하거나 활용하는 관점에서 양면성을 가지고 있다. 이 현상으로 발생하는 V굽힘 공정에서의 꺾임 결함은 소재에 상하방향 굽힘을 부과하는 롤러 레벨링 공정의 적용으로 감소될 수 있다. 롤러 레벨링 조건이 과할 경우 표면 결함이 발생할 수 있고, 적절한 공정 조건을 찾는 것이 여전히 어려운 실정이다. 예변형된 저탄소강을 구웠을 때 항복점이 현저하게 높이지는 특징을 보이는 소부 경화 거동은 이 현상을 활용하는 경우이며, 자동차 박판 금속 성형 응용 분야에서 덴트 저항성을 향상시키기 위해 사용된다. 그러나 소부 경화능에 대한 많은 연구는 일축 인장에서의 소부 경화 응답 및 그 영향인자에만 집중하고 있고, 자동차 강판의 덴트 저항성을 위한 수치적 연구는 소부 경화 효과를 거의 고려하지 않고 있다. 항복점 현상을 보이는 소재의 거동을 정확하게 예측하기 위해서는 점탄소성 수치해석을 위한 구성 모델이 항복점 현상, 바우싱거 효과, 그리고 소부 경화능을 묘사할 수 있어야 하지만, 이러한 예측과정에서 전통적인 1점 뉴턴법을 사용할 경우 내연적 수치해석에서 수렴된 해를 획득하기 어렵다. 본 연구에서는 먼저 V굽힘 공정에서의 꺾임, 롤러 레벨링 공정을 통한 꺾임 감소, 그리고 자동차 소부 경화 강판의 덴트 저항성에 대한 포괄적인 실험적 연구를 수행하였다. 일축 하중 하에서 저탄소 도장 강판의 속도 의존성과 주기 거동 특성을 조사한 뒤 V굽힘에서의 꺾임에 대한 롤러 레벨링 조건의 효과를 체계적으로 평가하였다. 2상 강판의 소부 경화 거동은 예변형과 소부 경화 조건의 일축 하중 및 정적 덴트 실험에서 관찰되었다. 이러한 실험적 관찰 결과를 수치해석으로 묘사하기 위해, 항복점 현상과 바우싱거 효과를 동시에 묘사할 수 있는 재료 구성 모델에 대해

내연적 응력 적분 과정을 수식화하고 이를 유한 요소 해석 코드로 구현하였다. 그리고 양분법과 2점 뉴턴법을 채택하여 내연적 유한 요소 해석에서 효율적으로 사용될 수 있는 강건한 응력 적분 알고리즘을 제안하였다. 또한 소부 경화능을 묘사하기 위해 소부 경화 모델과 본 재료모델을 통합하였다. 단순한 문제에 본 모델을 적용하여 수행한 검증 해석 결과는 고전적인 반복법으로는 해를 얻을 수 없는 항복점 현상 문제에 본 모델이 신뢰할 수준으로 사용될 수 있지만 계산 시간은 증가할 수도 있다는 것을 보여주었다. 일축 실험을 재현할 수 있도록 결정된 재료 변수들을 이용하여 실험에 대응되는 수치해석이 수행되었다. 다양한 롤러 레벨링 조건에서의 V굽힘 해석은 실험적으로 관찰된 꺾임 결함과 그 감소 현상을 잘 보여주었다. 실험에서 확인된 소부 경화 거동은 소부 경화 단계를 포함하는 정적 덴트 해석에서 분석되었고, 소부 경화 효과가 수치 해석에서 전반적으로 묘사되었다. 결론적으로 본 연구에서 제안된 해석 방법은 다양한 금속 성형 공정에서 항복점 현상의 효과를 연구하는 것 뿐만 아니라 꺾임 결함을 방지하기 위한 롤러 레벨링 조건을 추정하고 자동차 소부 경화 강판의 덴트 저항성을 예측하는데 유용하게 사용될 것으로 기대된다.

주요어: 항복점 현상, 점탄소성, 응력 적분 알고리즘, 꺾임, 소부 경화, 덴트
학번: 2016-36339